Integrated, adaptive and machine learning approaches to estimate the ghost wavefield of seismic data

Vrolijk, J.

Important note
To cite this publication, please use the final published version (if applicable).
Please check the document version above.

INTEGRATED, ADAPTIVE AND MACHINE LEARNING APPROACHES TO ESTIMATE THE GHOST WAVEFIELD OF SEISMIC DATA

Integrated, Adaptive and Machine Learning Approaches to Estimate the Ghost Wavefield of Seismic Data

Proefschrift

ter verkrijging van de graad van doctor
aan de Technische Universiteit Delft,
op gezag van de Rector Magnificus prof. dr. ir. T.H.J.J. van der Hagen,
voorzitter van het College voor Promoties,
in het openbaar te verdedigen op
vrijdag 27 november 2020 om 10:00 uur

door

Jan-Willem VROLIJK

Master of Science in Applied Physics,
Technische Universiteit Delft, Nederland,
geboren te Rijnsburg, Nederland.

Dit proefschrift is goedgekeurd door de promotoren

Samenstelling promotiecommissie:

Rector Magnificus	voorzitter
Prof. dr. ir. C.P.A. Wapenaar	Technische Universiteit Delft, promotor
Dr. ir. G. Blacquière	Technische Universiteit Delft, promotor

Onafhankelijke leden:

Prof. dr. ir. G.J.T. Leus	Technische Universiteit Delft
Prof. dr. ir. E.C. Slob	Technische Universiteit Delft
Prof. dr. J.O.A. Robertsson	ETH Zürich
Dr. L. Pahlavan	Technische Universiteit Delft
Dr. ir. R.F. Hegge	Aramco Overseas Company B.V.

Printed by: Gildeprint

An electronic version of this dissertation is available at
http://repository.tudelft.nl/.

CONTENTS

SUMMARY

In exploration geophysics, seismic measurements are used to obtain information about the subsurface. A large proportion of these measurements take place in oceans, seas and lakes, where the sources and the receivers are generally located somewhere between the water bottom and the water surface during data acquisition. The sources emit an acoustic signal into the subsurface and the receivers measure, amongst other things, the reflections of this signal. Some of these signals only reflect within the subsurface, but others may reflect at the water surface one or more times. The signals that reflect at the water surface disturb the reflections from the subsurface and have a destructive effect on the bandwidth. In this thesis the focus is on the removal of signals with the first reflection and/or the last reflection at the water surface. Correctly removing these so-called ghost reflections will improve the bandwidth.

In this thesis, three methods are covered, that aim to integrate the removal of ghost reflections into another process, or to improve the removal of ghost reflections under specific conditions. The first method integrates the removal of the receiver ghost into closed-loop surface-related multiple estimation. The results on modeled data and field data show that this is an efficient approach and provides a significant improvement over a sequential workflow. This first method, like many other methods that remove ghost reflections, requires accurate information about the depth of the receivers relative to the surface of the water. Due to a dynamic sea surface or movement of the cables this information about the depth of receivers is often not accurate, limiting the removal of the receiver ghost. The second method optimizes the removal of the ghost reflections by estimating and incorporating the depth of receivers relative to the dynamic water surface in this ghost removal process. On modeled data and field data, we show good results for cases where accurate information about the depth of the receivers relative to a dynamic water surface is not available. The first two methods address the removal of the receiver ghost, and it is well known that the receiver ghost should be removed in the shot domain. This is different when removing the source ghost, which has to be done in the receiver domain. However, in practice, the receiver domain is often coarsely sampled, complicating the removal of the source ghost in this domain. The third method handles the removal of the source ghost in the coarsely sampled receiver domain by training a convolutional neural network. The training data consist of coarsely sampled shot records with and without the receiver ghost that can be obtained relatively easy because the corresponding densely sampled shot records are available as well. Using reciprocity, these training data are a representative data set for removing the source ghost in the coarsely sampled receiver domain. The modeled data and field data results show that this machine learning approach is able to accurately remove the source ghost in the receiver domain. The modeled data results also show that this approach significantly improves the removal of the source ghost compared to its removal in the densely sampled shot domain.

SAMENVATTING

In exploratie-geofysica worden seismische metingen gebruikt om informatie over de ondergrond te verkrijgen. Een groot gedeelte van deze metingen vindt plaats in oceanen, zeeën en meren. Hierbij bevinden de bronnen en de ontvangers zich over het algemeen tussen de waterbodem en het wateroppervlak gedurende de data-acquisitie. De bronnen versturen een akoestisch signaal en de ontvangers meten onder andere de reflecties van dit signaal. Sommige van deze signalen reflecteren alleen in de ondergrond, maar anderen kunnen één of meerdere keren reflecteren aan het wateroppervlak. De signalen die reflecteren aan het wateroppervlak verstoren de reflecties afkomstig uit de ondergrond en hebben een destructieve uitwerking op de bandbreedte. In dit proefschrift ligt de focus op het verwijderen van signalen met als eerste en/of als laatste reflectie het wateroppervlak. Het correct verwijderen van deze zogenaamde spookreflecties (Eng.: 'ghost reflections') zal de bandbreedte verbeteren.

In dit proefschrift worden drie methodes behandeld die tot doel hebben om de verwijdering van spookreflecties met een ander proces te integreren, of om de verwijdering van de spookreflecties onder specifieke omstandigheden te verbeteren. De eerste methode integreert de verwijdering van spookreflecties aan de ontvangerkant in een gesloten-lus proces, welk de meervoudige oppervlaktereflecties schat. De resultaten op gemodelleerde data en velddata tonen aan dat dit een efficiënte manier is en een significante verbetering geeft ten opzichte van een sequentiële werkstroom. Deze eerste methode vereist, net als vele andere methodes die de spookreflecties verwijderen, nauwkeurige informatie over de diepte van de ontvangers ten opzichte van het wateroppervlak. Door een dynamisch zeeoppervlak of beweging van de kabels is deze informatie over de diepte van de ontvangers vaak niet nauwkeurig, wat de verwijdering van spookreflecties aan de ontvangerkant beperkt. De tweede methode optimaliseert de verwijdering van de spookreflecties door de schatting met betrekking tot de diepte van de ontvangers ten opzichte van het dynamische wateroppervlak in het proces te integreren. Op gemodelleerde data en velddata laten we zien dat dit de goede resultaten geeft voor het geval dat nauwkeurige informatie over de diepte van de ontvangers ten opzichte van het dynamische wateroppervlak niet beschikbaar is. De eerste twee methoden hebben betrekking op de verwijdering van spookreflecties aan de ontvangerkant, en het is algemeen bekend dat deze spookreflecties verwijderd moeten worden in het brondomein. In tegenstelling tot het verwijderen van spookreflecties aan de zenderkant, wat in het ontvangerdomein moet worden gedaan. In de praktijk is het ontvangerdomein echter vaak grof bemonsterd, wat de verwijdering van spookreflecties aan de zenderkant in dit domein bemoeilijkt. De derde methode behandelt de verwijdering van spookreflecties aan de zenderkant in het grof bemonsterde ontvangerdomein door een convolutioneel neuraal netwerk te trainen. De trainingsgegevens bestaan uit grof bemonsterde schot-data met en zonder spookreflecties aan de ontvangerkant, die relatief eenvoudig verkregen kunnen worden omdat de bijbehorende dicht bemonsterde schot-data ook beschikbaar

zijn. Door gebruik te maken van reciprociteit zijn deze trainingsgegevens een represen-
tatieve gegevensset voor het verwijderen van spookreflecties aan de zenderkant in het
grof bemonsterde ontvangerdomein. De resultaten verkregen met gemodelleerde data
en velddata tonen aan dat deze aanpak met machinaal leren in staat is om spookreflec-
ties aan de zenderkant nauwkeurig te verwijderen in het ontvangerdomein. De resulta-
ten verkregen met gemodelleerde data laten ook zien dat deze aanpak de verwijdering
van spookreflecties aan de zenderkant aanzienlijk verbetert in vergelijking met de ver-
wijdering in het dicht bemonsterde schotdomein.

1

INTRODUCTION

1

1.1. MARINE SEISMIC

Reflection seismology is used to obtain a structural image of the subsurface and retrieve geological information without drilling. This geophysical technique is of interest, e.g., for exploration, near-surface studies and archeology. In Figure 1.1 we show a near-surface profile of the Samyish river bottom in Russia and in Chapter 2 we show a structural image of the subsurface off the coast of Australia used for hydrocarbon exploration (Figure 2.9c). Seismic acquisition surveys must be carried out to obtain data leading to these structural images. These acquisition surveys can be performed on land and in water. The latter surveys are part of this thesis. In these acquisition surveys several seismic sources, e.g., an airgun, a vibrator, or an electric spark source could be chosen from to generate an acoustic wavefield. Depending on the type of source, the frequency range and the corresponding penetration depth of the acoustic wavefield may differ. To obtain the data in Figure 1.1 an electric spark source is used with a frequency range of 0.1-2 kHz, while in hydrocarbon exploration airguns with a frequency range of about 2-200 Hz are widely used. An example of a marine seismic acquisition survey is shown in Figure 1.2. When the source fires, part of the wavefield propagates in an upward direction, indicated by the red and green arrows, and part of the wavefield propagates in a downward direction, indicated by the blue and grey arrows. The downgoing wavefield in Figure 1.2 reflects from the water bottom and reflects in the subsurface due to differences in acoustic impedance in the medium. In practice, part of the upgoing wavefield will also reflect in the subsurface (see Figure 1.5). The receivers, indicated by the black triangles, are often hydrophones and record the reflected pressure wavefield. Not only the part of the wavefield that has one reflection in the subsurface (grey) is recorded, the receivers also record the so-called ghost wavefield, which first reflects from the water surface on the source side (green) and/or reflects last from the water surface on the receiver side
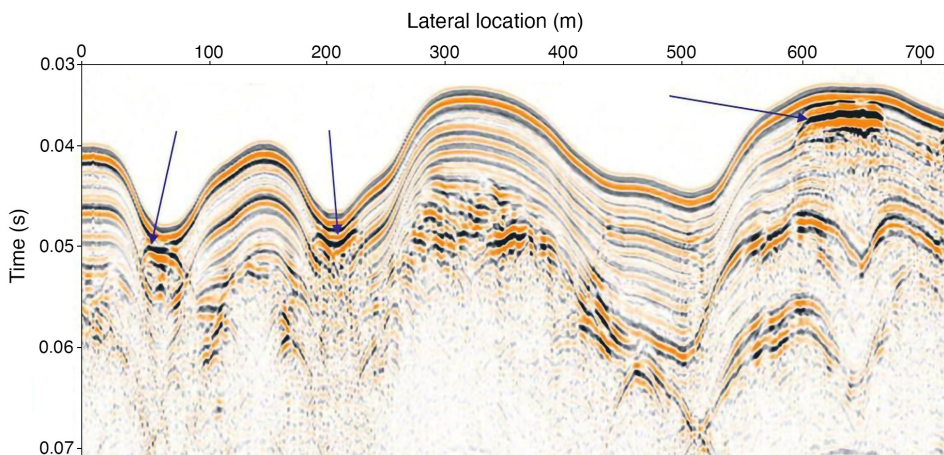

Figure 1.1: The near-surface profile of the Samyish river bottom, where the arrows indicate gas saturated sediments (Data recorded during NSU SEG Field Camp 2017).
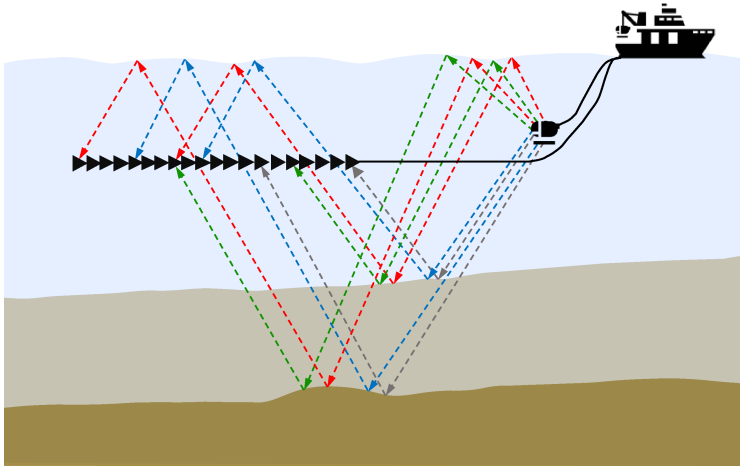
Figure 1.2: A schematic representation of a marine seismic acquisition survey with primary reflections (grey), source ghost reflections (green), receiver ghost reflections (blue) and source-receiver ghost reflections (red).

(red and blue). Due to the difference in acoustic impedance between water and air, the water surface acts as a strong reflector with a reflection coefficient of almost -1. A ghost wavefield can also occur on land, in case sources and/or receivers are buried. The ghost wavefield is a type of multiple reflection and in section 1.4 we will also discuss the two other types of multiples: surface related multiples and internal multiples. In the next section, we will discuss the effect of the ghost wavefield on the bandwidth of marine seismic data.

1.2. GHOST NOTCHES

We will introduce the notch effect by modeling a single reflection using a broadband source and broadband receiver (Figure 1.3a). In Figures 1.3b-1.3d we show the same reflection with, respectively, the source ghost, the receiver ghost and the source-receiver ghost. The ghost wavefields are modeled for sources at 12.5 m and receivers at 18.75 m below the water surface. The ghost wavefield causes interference in the wavenumber-frequency domain. Constructive interference amplifies areas in the amplitude spectra by 6 dB, causing peaks in those areas. While destructive interference causes notches in the amplitude spectra that do not contain any signal (Figures 1.3e-1.3g). The angle-dependent notch frequencies f_{notch} are given by:

$$f_{notch}(k_x) = \sqrt{\left(\frac{n \cdot c_w}{2\Delta z}\right)^2 + \left(\frac{k_x c_w}{2\pi}\right)^2}, \quad \text{for } n \in \mathbb{N}, \tag{1.1}$$

with n being the order of the notch, c_w being the wave propagation velocity in water, Δz being the depth of the source or receiver, k_x being the horizontal wavenumber and $\mathbb{N}$ being the set of natural numbers. In this thesis, several examples will show the full range of angle-dependent notch frequencies in the space-frequency domain as well as in the

1
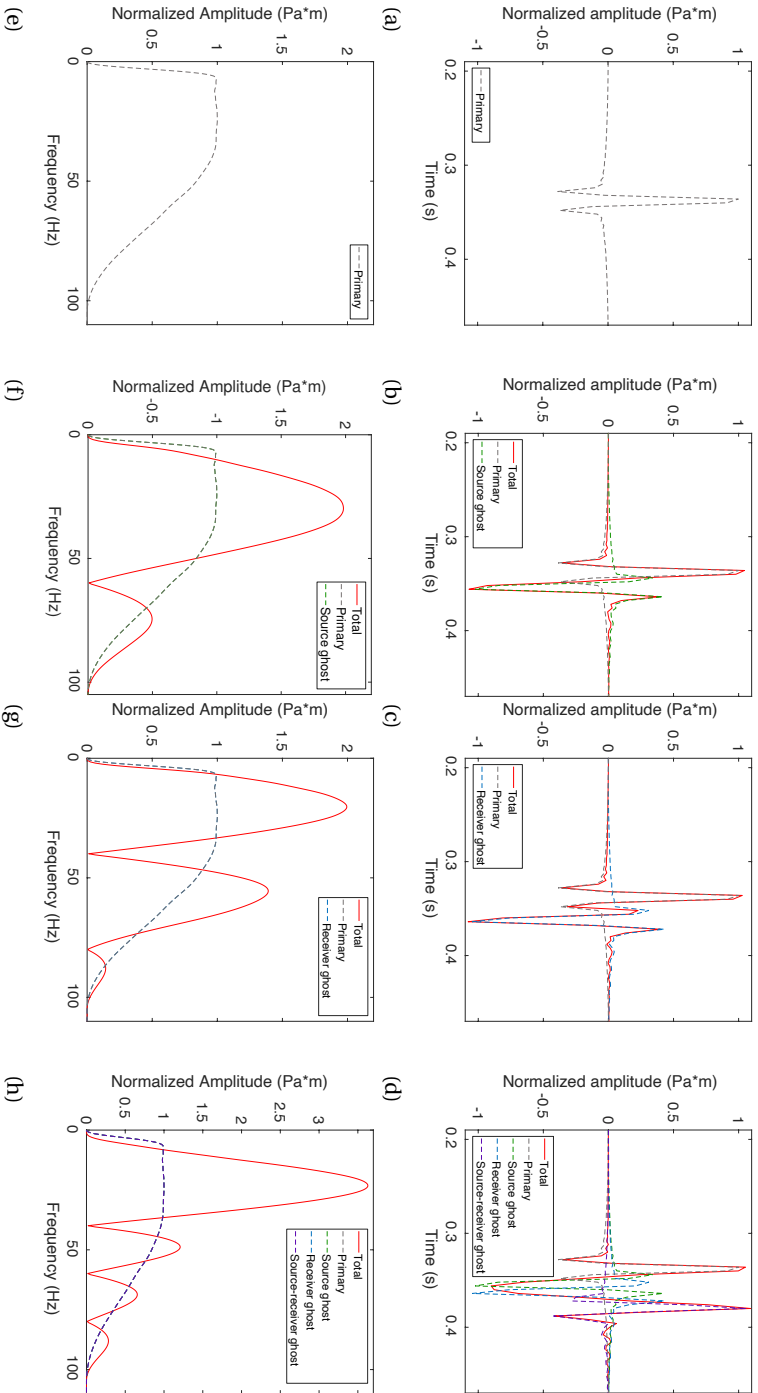

Figure 1.3: Modeled zero-offset traces with sources and receivers located at a depth of, respectively, 12.5 m and 18.75 m. a) Primary reflection. b) Primary reflection with source ghost. c) Primary reflection with receiver ghost. d) Primary reflection with source ghost as well as receiver ghost. e),f),g) and h) The amplitude frequency spectra for $k_x = 0$ corresponding to Figures 1.3a-1.3d.

wavenumber-frequency domain (sections 2.4, 3.5 and 4.3). In Figures 1.3f and 1.3h the first-order notch at 60 Hz that corresponds to $k_x = 0$ m^{-1}, $c_w = 1500$ m/s and $\Delta z = 12.5$ m is clearly visible. The first-order notch at 40 Hz and the second-order notch at 80 Hz that correspond to $k_x = 0$ m^{-1}, $c_w = 1500$ m/s, and $\Delta z = 18.75$ m are clearly visible in Figures 1.3g and 1.3h. There is always a notch at 0 Hz ($n = 0$ and $k_x = 0$ m^{-1}) regardless the depth Δz. The effect of this zero-order notch gradually increases as the source or receiver comes closer to the water surface, see Figures 1.3f and 1.3g. It is essential to correctly remove the ghost wavefield to increase the usable bandwidth and improve the resolution of the final image. In the next section we will look into the process of removing the ghost wavefield, which is referred to as deghosting.

1.3. DEGHOSTING AND THE EFFECT OF NOISE

Wavenumber-frequency domain deconvolution (which will be used as a bench-mark in Chapter 2) is one of the most common methods for deghosting seismic data (Amundsen et al., 2013). The deconvolution process must be stabilized in order to handle the deep notches in the spectrum. The stabilization also ensures that the generally poor signal-to-noise ratio in the notch areas does not dominate the deghosting result. Using a tuning parameter the algorithm compromises between noise suppression and signal recovery. Alternatively, a sparse inversion (which will be discussed in more detail in Chapter 3) can handle the deep notches as well. This method also uses a tuning parameter and is known to have a slightly better performance with respect to noise suppression in the notch areas (Vrolijk and Blacquière, 2017). In Figures 1.4a-1.4c we show respectively, source deghosting results, receiver deghosting results and the results for a combination of source and receiver deghosting. We added some Gaussian noise to the data from Figure 1.3b-1.3d to obtain the input data that has a signal-to-noise ratio of 30 dB, indicated by the dotted grey signals in Figures 1.4a-1.4c. These figures illustrate that indeed the performance of the sparse inversion algorithm, indicated by the red signals in Figure 1.4, is superior with respect to signal reconstruction and noise suppression. Especially, in the notch areas around 40, 60 and 80 Hz this is clearly visible (Figures 1.4d-1.4f). Note that the stabilized deconvolution results, indicated by the green signals in Figure 1.4, already gives a significant uplift compared to the almost non-stabilized deconvolution results, indicated by the blue signals in Figure 1.4. Note that there are many alternative source as well as receiver deghosting methods described in literature (Beasley et al., 2013; Berkhout and Blacquière, 2016; Ferber and Beasley, 2014; Robertsson et al., 2014; Soubaras, 2010). Most deghosting methods require the exact depth of the sources/receivers with respect to the water surface. However, the exact depth of the sources/receivers with respect to the water surface is not always known. In such a case the deghosting algorithm has to adapt to the exact depth of the sources and receivers with respect to possibly even a dynamic sea surface.
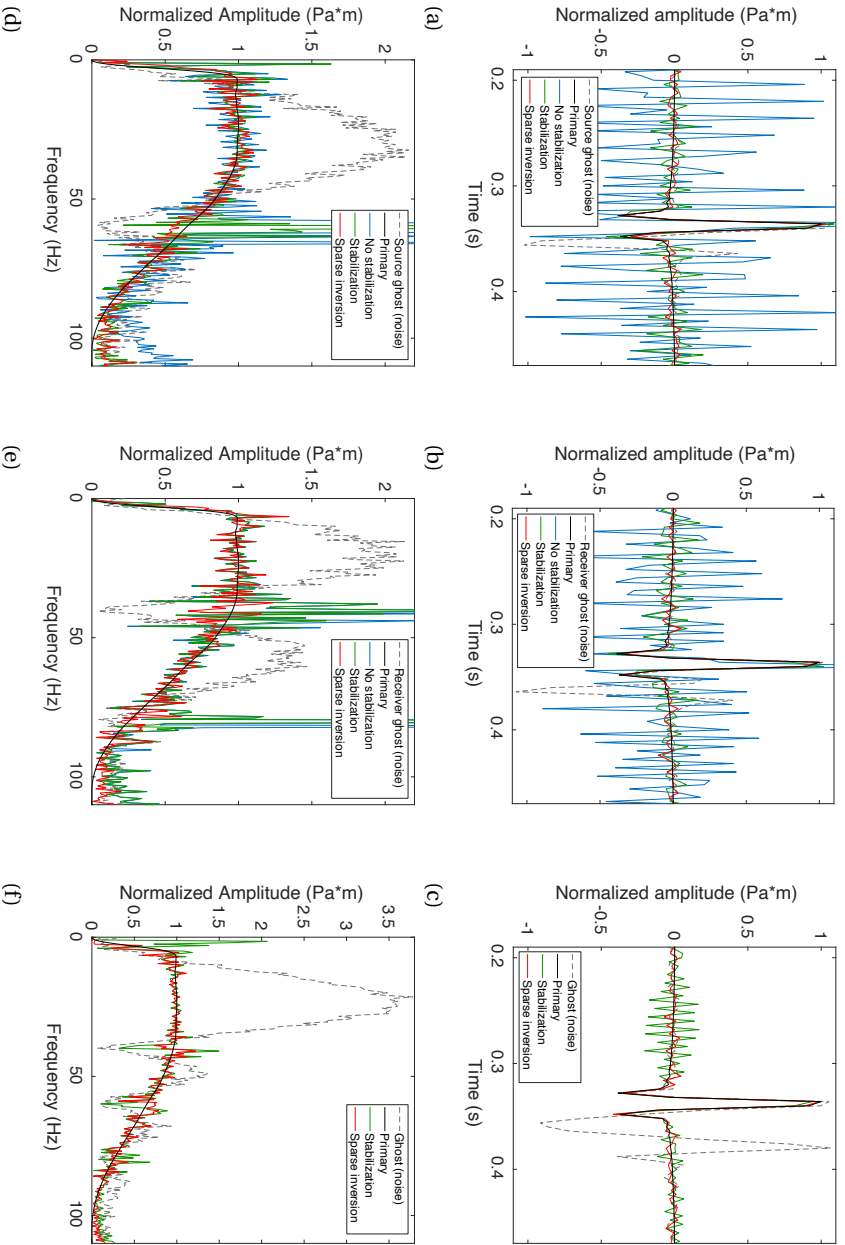
1

Figure 1.4: a),b) and c) The primary reflection without noise and the deghosting results for different methods applied to the traces from Figure 1.3b-1.3d after adding Gaussian noise. d),e) and f) The frequency spectra for $k_x = 0$ corresponding to Figures 1.4a-1.4c.
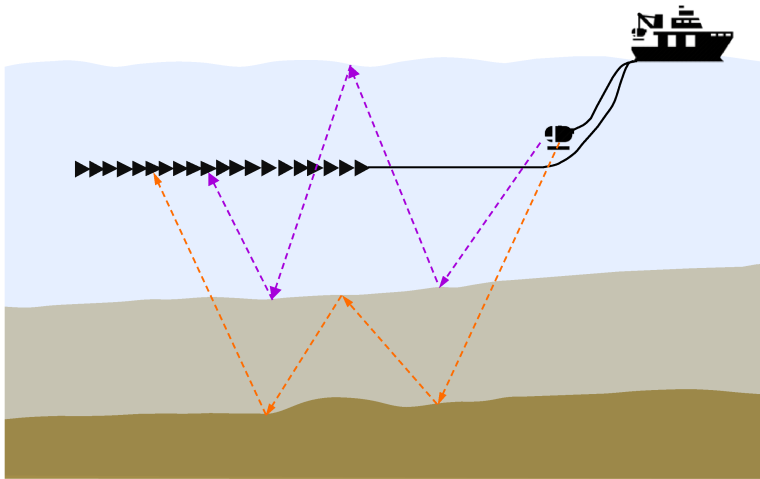
Figure 1.5: A schematic representation of a marine seismic acquisition survey with a surface multiple reflection (purple) as well as an internal multiple reflection (orange).

1.4. SURFACE AND INTERNAL MULTIPLES

In Figure 1.4 only the primary reflection and its ghost effects are annotated by arrows. However, in marine seismic there are two other types of multiple reflections: the surface multiples and the internal multiples. Examples of a surface multiple as well as an internal multiple are indicated, respectively, by purple arrows and orange arrows in Figure 1.5. Ghost wavefields first reflect from the water surface at the source side and/or reflect last from the water surface at the receiver side. Any other wavefield that reflects from the water surface is a surface multiple. Wavefields that reflect in the subsurface multiple times are so-called internal multiples. The source ghost, receiver ghost and source-receiver ghost of each surface multiple as well as each internal multiple are also recorded. Surface-related multiple elimination (SRME) is a well-known technique and requires deghosted data, therefore, source and receiver deghosting are usually carried out before SRME (Verschuur et al., 1992). In Chapter 2 we discuss SRME, while internal multiple elimination is outside the scope of this thesis.

1.5. THE EFFECT OF A DYNAMIC SEA SURFACE

Most deghosting as well as surface-related multiple removal methods assume that the sea surface is a perfectly flat reflector. Therefore, it is likely that there are errors in the processed data when there is a rough and dynamic (time-varying) sea surface. These errors will increase as the sea surface conditions become more severe. A widely used measure of the sea surface conditions is sea state, which is a measure of the height of the sea surface waves. Table 1 gives an overview of the sea states and their significant wave height (e.g. Ainslie, 2010). The significant wave height is the average peak-to-through

Table 1.1: Overview of sea states and their corresponding significant waveheight (SWH).

Sea state	Description	SWH (m)
0	Calm (glassy)	0
1	Calm (rippled)	0-0.1
2	Smooth (wavelets)	0.1-0.5
3	Slight	0.5-1.25
4	Moderate	1.25-2.5
5	Rough	2.5-4
6	Very Rough	4-6
7	High	6-9
8	Very High	9-14
9	Phenomenal	>14

height of the highest one-third of all waves taken into account and is related to the wind speed. A dynamic sea surface with a significant wave height of 2 m already affects the deghosted image as well as the data repeatability in time lapse acquisitions (Cecconello and Söllner, 2020; Laws and Kragh, 2002).

There are commonly two approaches to account for a dynamic sea surface in processing. One can account for a dynamic sea surface by approximating the dynamic sea surface with a single angle and frequency dependent reflectivity (Figure 1.6a) together with a flat sea surface (Blacquière and Sertlek, 2018; Orji et al., 2013). Including the exact dynamic shape (Figure 1.6b) is the other, exact approach and is pursued, e.g., in the methods described by King and Poole (2015) and Grion and Telling (2017). However,

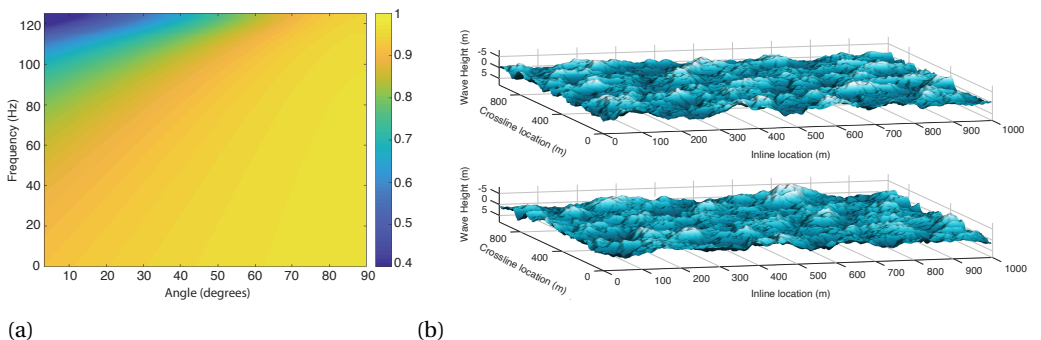(a)   (b)

Figure 1.6: Two approaches to account for a dynamic sea surface. a) Angle and frequency dependent reflectivity, Figure taken from Blacquière and Sertlek (2018). b) Two time-snapshots with a dynamic sea surface for sea state 5 and 3.5 s difference between them.

for both the approximate as well as the exact approach the necessary information, i.e. the dynamic shape of the sea surface, is not measured and has to be extracted from the seismic data (Grion and Telling, 2017; King and Poole, 2015; Kragh et al., 2004). In Chapter 3 we will include the estimation of the exact shape of the dynamic sea surface in an adaptive deghosting algorithm.

1.6. Receiver-side acquisition systems

There are many different acquisition systems used to obtain marine seismic data. A standard system on the receiver-side is a streamer at a constant depth relatively close to the water surface (from a few meters to tens of meters below the water surface). A streamer is an assembly of electrical wires or optical fibers that connects multiple hydrophones to the vessel. Some vessels tow multiple streamers to acquire more data per shot. Another receiver-side acquisition system is the slanted streamer, where the hydrophones are towed at a variable depth. The hydrophones are located a few meters below the sea surface for small offsets and the hydrophones are almost hundred meters below the water surface for large offsets. It provides higher resolution data and the signal-to-noise ratio is generally better, especially for the lower frequencies (Soubaras and Dowle, 2010). The improved signal-to-noise ratio is due to the deeper location of the hydrophones at larger offsets which are therefore less affected by ambient noise. The development of steerable cables allows streamers at a larger constant depth with respect to the water surface (approximately up to hundred meters below the water surface). In section 1.3 we have shown that the low-frequency content improves when the depth of the hydrophone with respect to the water surface increases. As a result, more low frequencies penetrate deeper into the subsurface, which results in improved imaging beneath salt bodies. In addition, seismic inversion will benefit from a better low-frequency content (ten Kroode et al., 2013). Proper receiver deghosting will improve the bandwidth for this
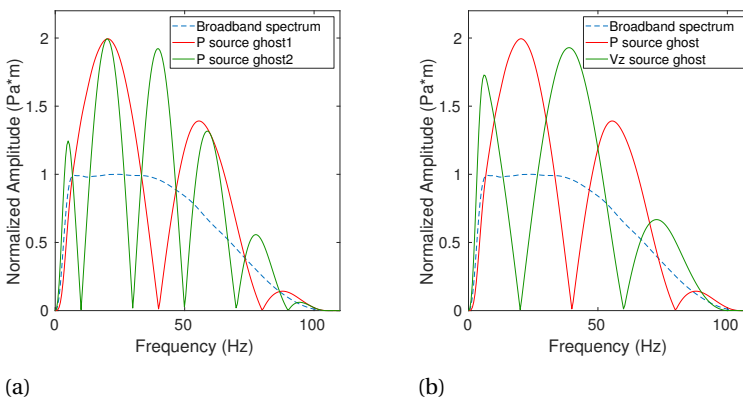

Figure 1.7: The spectra of the complimentary data with respect to the full bandwidth and the single component data. a) The spectra of an over/under streamer configuration ($\Delta z = 18.75$ m and $\Delta z = 37.5$ m). b) The spectra of the pressure component with receiver ghost and vertical component of the particle velocity with receiver ghost ($\Delta z = 18.75$ m).

1

type of streamers, regardless the specific depth profile. Even slanted streamers require proper receiver deghosting, despite the fact that their variable depth profile results in notch diversity (see sections 2.4, 2.5 and 3.5).

Other developments on receiver-side acquisition systems have led to the recording of complementary data. The double streamer configuration simultaneously records the pressure wavefield at two depth levels (their corresponding spectra are shown in Figure 1.7a). Posthumus (1993) described a method to deghost the acquired data from such an over/under streamer configuration. Alternatively, the complimentary vertical component of the particle velocity is recorded in addition to the pressure wavefield, both at the same depth (their corresponding spectra are shown in Figure 1.7b). A combination of the pressure and the vertical component of the particle velocity can decompose (and hence deghost) the wavefield into an upgoing and downgoing component. Multi- and dual component technologies both measure the vertical component of the particle velocity (Caprioli et al., 2012; Day et al., 2013; Letki and Spjuth, 2014; Tenghamn et al., 2007a). In this thesis we mainly focus on pressure-only data. However, in section 3.6 we will show that even a multi-component system can benefit from pressure-only deghosted data. Ocean-bottom nodes are specific multi-component receivers, most commonly used for monitoring purposes. Ocean bottom nodes are placed on the ocean floor and are able to record the elastic wavefield. The data quality of ocean bottom acquisition is superior to streamer data. The sources during ocean bottom acquisition are often still towed below the water surface, therefore ocean bottom data requires source deghosting.
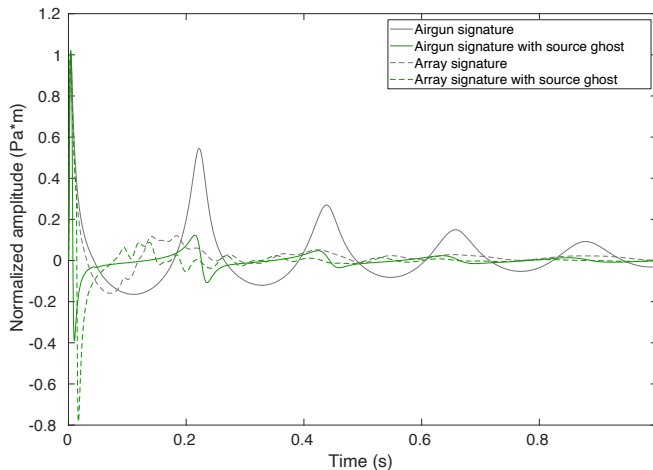

Figure 1.8: The original source signatures for a single airgun and an airgun array are plotted with gray color. The source signatures of a single airgun and airgun array with a source ghost are plotted with a green color. Sertlek and Ainslie (2015) developed the software to model these airgun signatures.

1.7. SOURCE-SIDE ACQUISITION SYSTEMS

At the source side, there are also multi-depth acquisiton systems, which could assist to remove the source ghost wavefield (Parkes and Hegna, 2011; Posthumus, 1993). Berkhout (2012) proposed dispersed source arrays consisting of multiple types of sources, each dedicated to a certain frequency range and each located at an appropriate depth. An example of a complimentary low-frequency source being used in exploration seismology is discussed by Dellinger et al. (2016).

The seismic data shown in this thesis, except for the data in Figure 1.1, are acquired with airguns. When an airgun fires, air is released into the water under high pressure and an acoustic wavefield is generated. The acoustic wavefield of a single airgun generates several unwanted damped oscillations after the initial pulse. These oscillations are the so-called bubbles, which are clearly visible in the airgun signatures shown in Figure 1.8. In practise, an array of airguns is used to reduce the unwanted bubbles, which again is visible in Figure 1.8. The airgun array used to obtain these signatures consists of 28 airguns with six different volumes. The green-colored signatures show the effect of the source ghost on its original source signature. When information about the source signature is known from near-field measurements or from an airgun model, it may be combined with source deghosting (Amundsen, 2017; Caprioli et al., 2019; Telling et al., 2018).

1.8. SPATIAL ALIASING CRITERIA

The Nyquist-Shannon theorem states that in order to reconstruct a signal it must be sampled at a rate greater than twice the highest frequency component f_{max}. In seismic data acquisition, the recorded signals, are sampled at discrete time intervals. The maximum time sampling Δt according to the sampling theorem is given by:

$$\Delta t < \frac{1}{2f_{max}}. \tag{1.2}$$

Seismic data are also recorded at discrete spatial locations. The spatial sampling Δx according to the sampling theorem is given by:

$$\Delta x < \frac{c_{min}}{2f_{max}sin(\alpha)}, \tag{1.3}$$

where c_{min} is the minimum propagation velocity and α is the maximum angle of approach of the recorded wavefield. For a derivation of the spatial sampling criterium the reader is referred to Geldart and Sheriff (2004). In practice, equation 1.3 is often violated for economic reasons. In that case so-called aliasing effects occur, in particular for the higher frequencies and the steeper angles. In order to overcome the effects of aliasing sometimes anti-aliasing methods are used in seismic processing. There are numerous spatial anti-aliasing methods (e.g. Trad, 2009; Zwartjes and Sacchi, 2007). In some seismic acquisition surveys even the spatial sampling requirements for these anti-aliasing methods are violated. During seismic processing of these surveys spatial aliasing still

1

has a negative effect on, e.g., deghosting (section 4.4), surface-related multiple removal and imaging. For more information on the latter we refer the reader to Yilmaz (2001).

1.9. THESIS OBJECTIVE AND OUTLINE

A general theme that is investigated in this thesis is the possibility to integrate deghosting with other seismic processes. Another objective is to overcome some of the remaining challenges in the deghosting of seismic data.

- In *Chapter 2* we integrate closed-loop surface related multiple elimination with receiver deghosting. It contains a comparison of this integrated approach with a sequential approach on synthetic data. It also shows the results on a field data experiment.
- In *Chapter 3* we propose an adaptive receiver deghosting algorithm. This algorithm integrates the estimation of the receiver ghost parameters into a receiver deghosting algorithm. It contains a comparison of this adaptive deghosting algorithm with a deterministic one. On field data it compares the adaptive algorithm with an up-down seperation technique.
- In *Chapter 4* we address the challenge of deghosting spatially aliased data by using a machine learning approach. The focus is on deghosting receiver-data obtained with coarsely-sampled sources.
- *Chapter 5* concludes the thesis and provides recommendations. For some of these recommendations initial results are shown.

2

INTEGRATED RECEIVER DEGHOSTING AND SURFACE-MULTIPLE ELIMINATION

Accurate surface-related multiple removal is an important step in conventional seismic processing, and more recently, primaries and surface multiples are separated such that each of them is available for imaging algorithms. Current developments in the field of surface-multiple removal aim at estimating primaries in a large-scale inversion process. Using such a so-called closed-loop process, in each iteration primaries and surface multiples will be updated until they fit the measured data. The advantage of redefining surface-multiple removal as a closed-loop process is that certain pre-processing steps can be included, which can lead to an improved multiple removal. In principle, the surface-related multiple elimination process requires deghosted data as input; thus, the source and receiver ghost must be removed. In this chapter we focus on the receiver ghost effect and assume that the source is towed close to the sea surface, such that the source ghost effect is well-represented by a dipole source. We integrate the receiver ghost effect within the closed-loop primary estimation process. Thus, primaries are directly estimated without the receiver ghost effect. After receiver deghosting, the upgoing wavefield is defined at zero depth, which is a flat sea surface. We successfully validate our method on 2D simulated data and on a 2D subset from 3D broadband field data with a slanted cable.

2.1. INTRODUCTION

For many marine data sets, accurate removal of surface multiples remains a nontrivial process, especially with a focus on modern broadband data with possible slanted streamers. To properly eliminate surface multiples, it is necessary that the input data are source and receiver deghosted. Dual streamer (Monk, 1990) and multi-component streamers (Caprioli et al., 2012; Tenghamn et al., 2007a) are hardware solutions at the receiver side. In the case of conventional streamers, deghosting is still a challenging preprocessing step. In general, the receiver ghost notch appears inside the desired frequency spectrum in current acquisition techniques that aim at broadband data. Consequently, ghost effects are removed in a separate preprocessing step to improve the image resolution significantly. At the receiver side, Amundsen et al. (2013) describe deghosting as a spatial deconvolution in the frequency domain. To remove the receiver ghost, Ferber et al. (2013) combine pressure data with an estimate of the particle velocity data. Beasley et al. (2013) and Robertsson et al. (2014) use the fact that the upcoming waves arrive earlier than the downgoing ghost waves, leading to causal deghosting filters. Ferber and Beasley (2014) use this principle to shift the ghost events out of the time window. In practice, uncertainties in the estimated water velocity, receiver depth, and a rough sea can lead to errors in the ghost model. To handle these uncertainties we propose an adaptive deghosting algorithm in Chapter 3 that takes into account small deviations in these parameters. Alternative methods to adaptively estimate these parameters and give the best deghosting result are proposed by Rickett et al. (2014), King and Poole (2015) and Grion et al. (2015). In this chapter, the source is assumed to be towed close to the sea surface, such that the source ghost effect is well-represented by a dipole effect. Due to nonlinear effects at the source side and coarse sampling, source deghosting requires a different approach. These limitations on the source side make it a more complex problem compared with the receiver side. Therefore, at the source side, the number of methods is limited for conventional seismic. Some examples are the work of Mayhan and Weglein (2013) and Amundsen and Zhou (2013) . In addition, Berkhout and Blacquière (2016) introduce source deghosting as a special case of deblending. In Chapter 4 we propose a machine learning approach to overcome the coarse sampling issue on the source side.

In this chapter, removing the receiver ghost is integrated with surface-multiple removal. After receiver deghosting, wavefields that are measured at the receiver depth are now estimated as upgoing wavefields at a zero depth. If one of the earlier receiver deghosting methods is not accurate, this can result in an inaccurate estimate of surface multiples. The surface-related multiple elimination (SRME) method (see a.o. Berkhout, 1982; Berkhout and Verschuur, 1997; Verschuur et al., 1992) has become one of the standard multiple removal tools because it can predict multiples without any knowledge on the subsurface. The theory of SRME uses the estimate of the primary data to predict the surface multiples. This estimated primary data set should ideally have a spike wavelet and no ghost effects. However, usually the wavelet effects are kept in, yielding predicted multiples that exhibit a wrong wavelet, which needs to be corrected for in adaptive subtraction. The latter is usually based on a minimum energy criterion, which is known for

not always being optimal for SRME (Aaron et al., 2008; Dragoset et al., 2008; Guitton and Verschuur, 2004; Nekut and Verschuur, 1998).

Therefore, a new approach to multiple removal was developed by van Groenestijn and Verschuur (2009a): estimation of primaries by sparse inversion (EPSI). The main difference with SRME is that prediction and adaptive subtraction are replaced by an inversion process: The primary reflection events are the unknowns in this algorithm and are parameterized in a suitable way. The primaries are estimated such that - together with the associated surface multiples - they explain the input data. In van Groenestijn and Verschuur (2009a), the adopted parameterization consists of band-limited spikes and an effective source wavelet. Examples on complex synthetic and field data sets are shown by van Groenestijn and Verschuur (2009b) and Savels et al. (2011). Baardman et al. (2010) discuss a refinement for dispersion effects, and Lin and Herrmann (2013) develop so-called robust EPSI, which is an implementation that is more robust in terms of optimization and is guaranteed to converge to a global minimum.

Recently, another implementation of the inversion scheme was introduced by Lopez and Verschuur (2015). Their so-called closed-loop SRME (CL-SRME) scheme directly estimates the observed primaries - including the wavelet - and the inverse source operator instead of the band-limited spikes and effective source wavelet in EPSI.

One advantage of writing primary estimation as an inversion problem is the fact that imperfections in the data, which usually have a distorting effect on the SRME-output, within EPSI/CL-SRME may be mitigated during the inversion process, if properly handled. This was already shown in van Groenestijn and Verschuur (2009a) and by Lopez and Verschuur (2015) for the missing near-offset data. In addition, ghost effects need to be accounted for in SRME-type multiple prediction (Weglein et al., 1997). Therefore, we will need to include the ghost effect in the CL-SRME formalism, such that we are directly estimating the observed primaries including the wavelet without the ghost influence. An initial version to include the ghost in EPSI was already described by Verschuur (2014). However, including the ghost in EPSI results in extrapolation artifacts due to the combination of applying the ghost operator and thresholding in the updating scheme. Including the ghost in CL-SRME can give smaller artifacts that can be handled with the inversion process, as we will show. Another disadvantage of including the ghost in the EPSI approach, as proposed by Verschuur (2014), is that the ghost operator and inverse ghost operator were assumed to cancel in the involved multiple prediction step. In case of a slanted cable, this assumption is no longer valid. In CL-SRME, it is possible to estimate the inverse ghost operator together with the inverse source wavelet and leave the ghost operator within the multiple prediction formulation. In the following sections, the theoretical framework of SRME and CL-SRME is described. After that, including the receiver ghost in CL-SRME is explained for a flat streamer and a depth-varying streamer. This method is applied to the 2D synthetic examples and a 2D field case.

2.2. SRME AND CL-SRME: A REVIEW

In Berkhout and Verschuur (1997), it has been proposed to rewrite the surface-related multiple removal scheme of Verschuur et al. (1992) as an iterative procedure:

$$\mathbf{P}_0^{(i+1)} = \mathbf{P} - \mathbf{P}_0^{(i)}\mathbf{A}^{(i)}\mathbf{P}, \qquad (2.1)$$

where $\mathbf{P}_0^{(i)}$ represents the prestack data containing the estimated primaries and the internal multiples in iteration i, $\mathbf{P}$ being the total data (primaries, internal multiples, and surface multiples), and $\mathbf{A}$ representing the so-called surface operator:

$$\mathbf{A} = \mathbf{S}^{-1}\mathbf{R}\mathbf{D}_m^{-1}, \qquad (2.2)$$

where the inverse source $\mathbf{S}^{-1}$ and the inverse receiver properties $\mathbf{D}_m^{-1}$ are combined with the reflectivity at the free surface $\mathbf{R}$. The notation is taken from Berkhout (1982). Note that in our formulation, it is assumed that the data $\mathbf{P}$ have no receiver ghost effects, exhibit a dipole source, and represent upgoing wavefields at the receivers. If a monopole source is towed not too deep, which is often the case, e.g., in our field data example, the source ghost effect may well-represent this dipole effect. Otherwise, proper source deghosting needs to be applied and a so-called obliquity factor needs to be included in the A-operator (see Weglein et al., 1997). Neglecting the obliquity factor will lead to inaccurate prediction of surface multiples in terms of amplitude and phase (see Weglein et al., 2003). In practice, accurate source deghosting is limited by coarse sampling in the source direction. To apply source deghosting in a similar way as on the receiver side, the data have to be reconstructed to a dense source sampling.

Each column of a data matrix, e.g., $\mathbf{P}$, contains a wave field (or a shot record) for one frequency. The primary data $\mathbf{P}_0$ can be written as the source matrix times the primary impulse response matrix:

$$\mathbf{P}_0 = \mathbf{X}_0\mathbf{S}. \qquad (2.3)$$

Each column of the source matrix contains the effective downgoing wavefield for one shot record. In practice, the directivity effects are often neglected or taken into account in a separate preprocessing step (a deghosting process), such that matrix $\mathbf{A}$ can be written as a frequency-dependent scalar $A(\omega)$ (Verschuur and Berkhout, 1997). Thus, the prediction and subsequent adaptive subtraction of the surface-related multiples can be written as:

$$\hat{\mathbf{M}}^{(i+1)} = \mathbf{P}_0^{(i)}A^{(i+1)}(\omega)\mathbf{P} \quad ; \quad \mathbf{P}_0^{(i+1)} = \mathbf{P} - \hat{\mathbf{M}}^{(i+1)}, \qquad (2.4)$$

where the second step usually assumes minimum energy in the output ($\mathbf{P}_0$).

It has been demonstrated that the adaptive subtraction of predicted multiples is the weak link in the SRME process because it allows multiples to locally match with strong primary energy, yielding distortions of the primaries and, as a consequence, leaving the residual multiple energy behind (see e.g. Abma et al., 2005; Guitton and Verschuur, 2004; Nekut and Verschuur, 1998). Therefore, in the CL-SRME algorithm, this subtraction process is avoided by making the primaries the unknowns in a large-scale inversion process.

To describe the CL-SRME algorithm (Lopez and Verschuur, 2015), we again consider equation 2.1. Through full waveform inversion, we try to estimate the unknown, multidimensional primaries $\mathbf{P}_0$ and surface operator $\mathbf{A} = \mathbf{S}^{-1}\mathbf{R}\mathbf{D}_m^{-1}$ such that the primaries, including the internal multiples $\mathbf{P}_0$ together with the surface multiples $\mathbf{P}_0\mathbf{A}\mathbf{P}$ can explain the total upgoing data $\mathbf{P}$. The difference between the total upgoing data $\mathbf{P}$ and the estimated primaries, including internal multiples plus surface multiples, $\hat{\mathbf{P}}_0 + \hat{\mathbf{P}}_0\hat{\mathbf{A}}\mathbf{P}$, is the residual, where the ˆ indicates an estimated value. The CL-SRME algorithm drives this residual to zero; i.e., it is minimizing the following objective function (see Lopez and Verschuur, 2015):

$$J = \sum_{\omega} \left|\left|\mathbf{P} - \hat{\mathbf{P}}_0 - \hat{\mathbf{P}}_0\hat{\mathbf{A}}\mathbf{P}\right|\right|^2 + \lambda \sum_{t} \left|\left|\hat{\mathbf{p}}_0\right|\right|_S, \tag{2.5}$$

where we usually assume that the surface reflection matrix $\mathbf{R} = -\mathbf{I}$, each data matrix contains one frequency component ω, and t is representing a time-slice. In equation 2.5, $\hat{\mathbf{P}}_0$ and $\hat{\mathbf{A}}$ represent the estimate of the primary data and the estimate of the surface operator that contains the inverse source wavelet, respectively. However, solving the first term of the objective function gives a nonunique solution for $\hat{\mathbf{P}}_0$ and $\hat{\mathbf{A}}$. Therefore, a sparsity-promoting regularization norm $\left|\left|\hat{\mathbf{p}}_0\right|\right|_S$ is added, where $\hat{\mathbf{p}}_0$ is representing the primaries in the time domain. This can be steered by a user-defined regularization constant. In practice, the total amplitude of the second term is in the order of 1% of the first term. The data residual can be used as a quality control for this constant, if λ is too high, primary energy will leak into the data residual, and it is no longer estimated by the method. To have a better control on the sparsity constraint, a linear Radon transform can be included in the algorithm, such that $\hat{\mathbf{p}}_0$ is assumed to be sparse in the linear Radon domain. In the field data example, using the linear Radon domain gave a significant uplift for the result, but in the synthetic case, there was no significant difference in the result of the estimated primaries.

2.3. Including the receiver ghost in CL-SRME

When the receiver ghost effect is included in CL-SRME, the forward model for equation 2.1 becomes:

$$\mathbf{P}_g = \mathbf{D}_g\mathbf{P}_0 + \mathbf{D}_g\mathbf{P}_0\mathbf{A}\mathbf{D}_g^{-1}\mathbf{P}_g, \tag{2.6}$$

where the detector operator $\mathbf{D}_g$ contains the ghost effect at the receiver side and $\mathbf{P}_g$ represents the measured data including the detector ghost. The total detector operator becomes $\mathbf{D} = \mathbf{D}_m\mathbf{D}_g$. Each column in matrix $\mathbf{D}_g$ contains the effective operator that modifies the upgoing wavefield at the surface (z_0) to the receiver level, being defined as:

$$\mathbf{D}_g(z_d, z_0) = \mathbf{F}(z_d, z_0) + \mathbf{W}(z_d, z_0)\mathbf{R}, \tag{2.7}$$

where $\mathbf{W}(z_d, z_0)$ describes the forward propagation from the surface - after reflection - toward the detector level z_d and $\mathbf{F}(z_d, z_0) \approx [\mathbf{W}(z_d, z_0)]^*$ describes an inverse propagation from the surface to the detector level, where superscript $*$ indicates the complex conjugate of the matrix. In the case in which the receiver cable is flat, each column $\vec{D}_g(z_d, z_0)$ can be calculated as the inverse spatial Fourier transform of the wavenumber operator:

$$\tilde{D}_g(k_x; \omega) = e^{+jk_z\Delta z} + Re^{-jk_z\Delta z}, \tag{2.8}$$

with k_z being the vertical wavenumber ($k_z = \sqrt{(k^2 - k_x^2)}$), with horizontal wavenumber k_x, wavenumber $k = \omega/c$, c being the propagation velocity in water, and $\Delta z = |z_0 - z_d|$. If we assume the flat cable situation, we can see in the last term of equation 2.6 that we first remove the ghost effect from the measurements $\mathbf{P}_g$, creating the upgoing wavefield at the surface, after which it is convolved with operator $\mathbf{A}$ and the primaries $\mathbf{P}_0$ to predict the multiples. Finally, the ghost effect has to be included in the predicted multiples to match it with the observed data. However, assuming that the subsurface structures are moderate, such that the arrival angles of the events do not change much from source to receiver side, these two ghost response matrices approximately cancel, which can be the case for a flat cable configuration:

$$\mathbf{P}_g \approx \mathbf{D}_g \mathbf{P}_0 + \mathbf{P}_0 \mathbf{A} \mathbf{P}_g. \tag{2.9}$$

The operator $\mathbf{D}_g$ - strictly speaking - cannot be used anymore in our matrix notation because the spatial location of the slanted cable is related to the spatial location of the source. The spatial location and corresponding depth of a receiver, therefore, moves along with the spatial location of the source in a fixed-spread configuration. In addition, the movement of a cable can cause time dependent variations in the receiver position as well. Therefore, an operator table is constructed containing matrices $\mathbf{D}_g$ for each receiver depth. For each shot record, i.e., column of the data matrix $\mathbf{P}$, a ghost operator $\mathbf{D}_{g,j}$ is constructed from this operator table that takes into account the different receiver depths. In fact, equation 2.6 should be written separately for each shot record with corresponding ghost operator because the receiver depths can vary for each shot:

$$\mathbf{P}_g = \mathbf{P}_{g_0} + \mathbf{P}_{g_0} \hat{\mathbf{A}} \mathbf{P}_{dg} \tag{2.10}$$

with,

$$\mathbf{P}_{g_0} = \left\{ \mathbf{D}_{g,1} \hat{\vec{P}}_{0,1}; \ldots ; \mathbf{D}_{g,j} \hat{\vec{P}}_{0,j}; \ldots ; \mathbf{D}_{g,N} \hat{\vec{P}}_{0,N} \right\}, \tag{2.11}$$

and

$$\mathbf{P}_{dg} = \left\{ \mathbf{D}_{g,1}^{-1} \vec{P}_{g,1}; \ldots ; \mathbf{D}_{g,j}^{-1} \vec{P}_{g,j}; \ldots ; \mathbf{D}_{g,N}^{-1} \vec{P}_{g,N} \right\}, \tag{2.12}$$

where $\mathbf{P}_{g_0}$ contains the primaries including the ghost operator and $\mathbf{P}_{dg}$ contains the measured data including the ghost effect convolved with the inverse ghost operator. Thus, for each specific shot record j for a data set with a total of N shots, a matrix-vector multiplication of the primary data $\hat{\vec{P}}_{0,j}$ and the corresponding ghost operator $\mathbf{D}_{g,j}$ and a matrix-vector multiplication of the measured data $\hat{\vec{P}}_{g,j}$ and the corresponding inverse ghost operator $\mathbf{D}_{g,j}^{-1}$ are carried out. In this case, the arrival angles of the events do change from source to receiver side and the approximation (see equation 2.10) does not hold anymore. Therefore, $\mathbf{D}_{g,j}^{-1}$ will be estimated from the ghost operator $\mathbf{D}_{g,j}$ using a stabilized matrix inversion for each frequency:

$$\mathbf{D}_{g,j}^{-1} \approx \mathbf{D}_{g,j}^{H} [\mathbf{D}_{g,j}^{H} \mathbf{D}_{g,j} + \epsilon \mathbf{I}]^{-1}, \tag{2.13}$$

with ϵ some stabilization value and $\mathbf{I}$ the identity matrix.

Knowing the receiver depths, even for a slanted cable, the ghost operator is deterministic and can easily be included in the CL-SRME algorithm.

Based on the forward models in equation (2.9) or (2.10), now two new objective functions can be determined for a flat and a slanted configuration that should be minimized, meaning driving the residual data to zero. We will use:

$$J = \sum_{\omega} \left|\left| \mathbf{P}_g - \mathbf{D}_g \hat{\mathbf{P}}_0 - \hat{\mathbf{P}}_0 \hat{\mathbf{A}} \mathbf{P}_g \right|\right|^2 + \lambda \sum_t \left|\left| \hat{\mathbf{p}}_0 \right|\right|_S, \tag{2.14a}$$

for the horizontal cable and

$$J = \sum_{\omega} \left|\left| \mathbf{P}_g - \mathbf{P}_{g0} - \mathbf{P}_{g0} \hat{\mathbf{A}} \mathbf{P}_{dg} \right|\right|^2 + \lambda \sum_t \left|\left| \hat{\mathbf{p}}_0 \right|\right|_S, \tag{2.14b}$$

for the slanted cable. This means that to evaluate an obtained estimate of the (ghost-free) primaries $\hat{\mathbf{P}}_0$, a forward ghosting process needs to be involved to compare the estimated (ghost-free) primaries and the estimated (ghost-free) multiples in case of the slanted cable with the observed data that include a ghost. Next, the gradients of the objective functions with respect to the primary data need to be determined, which read:

$$\nabla_{\hat{\mathbf{P}}_0^{(i)}} J = -2 \left\{ \mathbf{D}_g^H \mathbf{V}^{(i)} + \mathbf{V}^{(i)} [\mathbf{A} \mathbf{P}_g]^H \right\} + \mathscr{F} \left\{ \lambda \cdot \text{sgn}(\hat{\mathbf{p}}_0) \right\} \tag{2.15a}$$

and

$$\nabla_{\hat{P}_0^{(i)}} J = -2 \mathbf{D}_{g,j}^H \left\{ \vec{V}_j^{(i)} + (\mathbf{V}^{(i)} [\vec{A}_j^{\dagger} \mathbf{P}_{dg}]^H) \right\} + \mathscr{F} \left\{ \lambda \cdot \text{sgn}(\hat{\vec{p}}_{0,j}) \right\}, \tag{2.15b}$$

where $\mathbf{V}$ indicates the residual data in the case of data with a ghost, where the dagger symbol † indicates a row vector, $\mathscr{F}$ indicates the temporal Fourier transform and the gradient of the sparsity promoting term is expressed by the signum function. Note that in the calculation of the update for $\mathbf{P}_0$ or $\vec{P}_{0,j}$ now also one or two adjoint ghosting operators are involved. This adjoint ghost operator makes sure that the contribution to the primaries in the data gets a ghost-free character, as is expected for the primaries.

Besides these modifications to the forward model, the objective function and the gradient, the CL-SRME algorithm remains largely the same, as described by Lopez and Verschuur (2015).
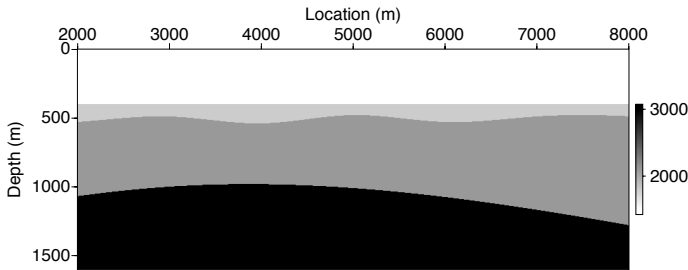

Figure 2.1: Velocity model for acoustic finite-difference modelling scheme. Note that the bottom also acts as reflector.

2.4. MODELED DATA

We will demonstrate the effect of ghosts on CL-SRME both for a flat and slanted cable. The data are modelled with an acoustic finite-difference scheme. The three-reflector velocity model with a reflecting bottom boundary for this scheme is illustrated in Figure 2.1. The source and receiver sampling is 15 m. Extended CL-SRME is applied to a fixed-spread configuration of 401 sources by 401 receivers with a sampling of 4 ms.
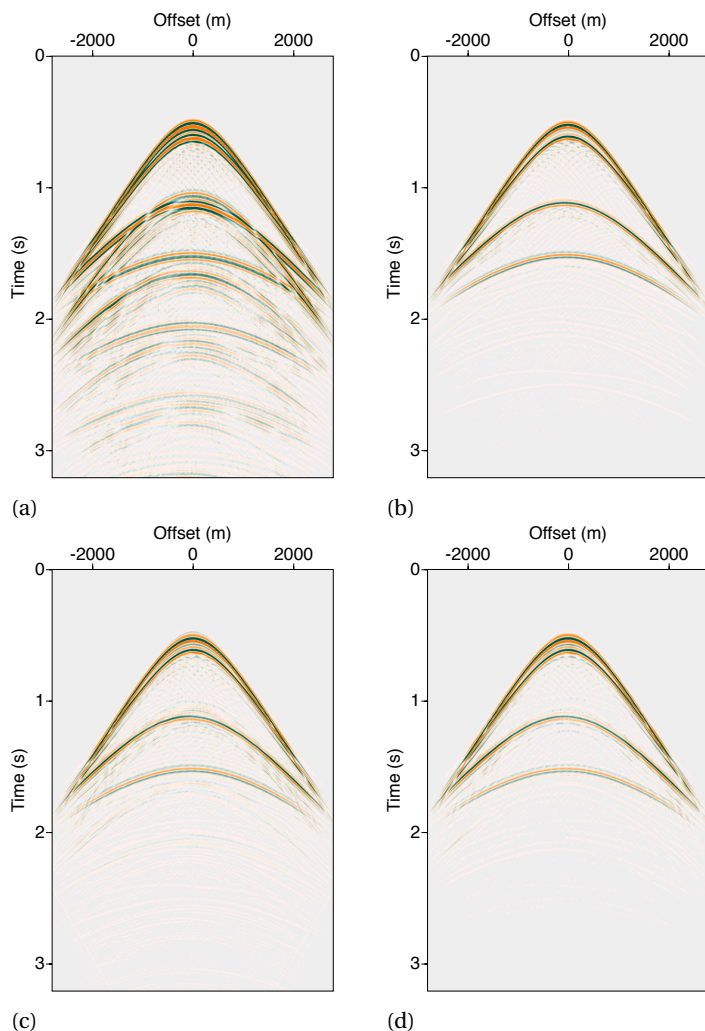

Figure 2.2: Results for a shot from the synthetic data with a 25 m receiver ghost effect. a) Input shot including the ghost. b) Modeled primaries. c) Primaries after deghosting followed by CL-SRME. d) Primaries after CL-SRME including the ghost.
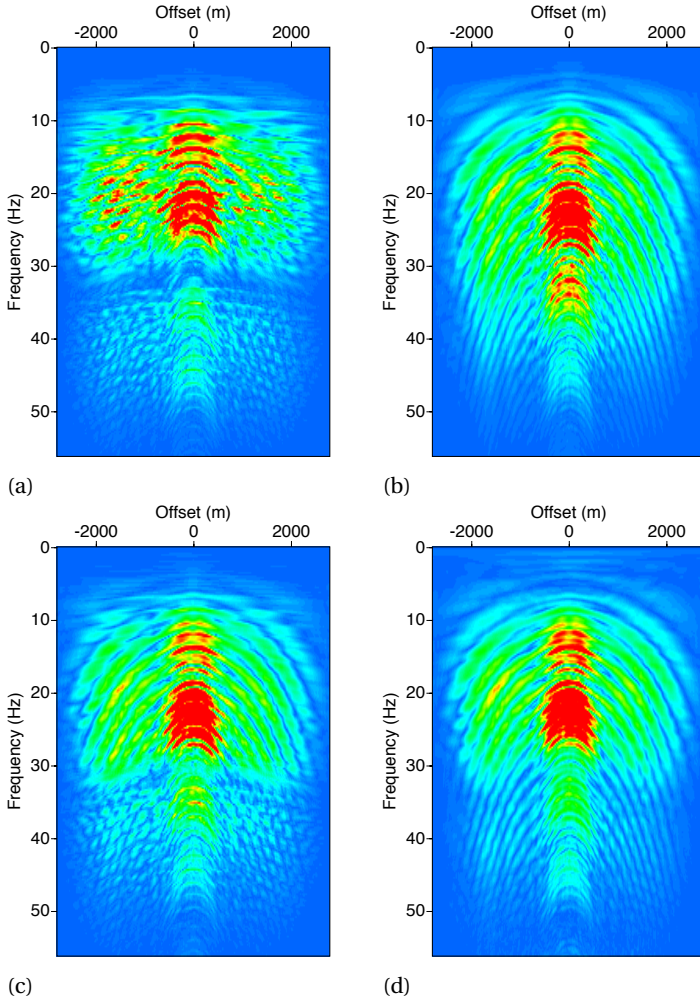
Figure 2.3: Results for a shot from the synthetic data with a 25 m receiver ghost effect in the frequency domain. a) Input shot including the ghost. b) Modeled primaries. c) Primaries after deghosting followed by CL-SRME. d) Primaries after CL-SRME including the ghost.

In the first case, the data are modeled with a cable at 25 m depth. A single shot from this data is illustrated in Figure 2.2a. To validate the results after CL-SRME, also a dataset set is modeled without the receiver ghost effect, thus with a cable at zero depth (Figure 2.2b). For better comparison, both these datasets are modeled with a source ghost at 5 m depth, which gives the data a dipole source character. To obtain Figure 2.2c, the inverse ghost operator from equation 2.13, calculated via stabilized least-squares inversion, is applied to the input shot (Figure 2.2a) and followed by CL-SRME. After this cascaded approach, most of the surface-multiple energy is removed. However, compared to the reference shot (Figure 2.2a), some surface-multiple energy leaked into the domain
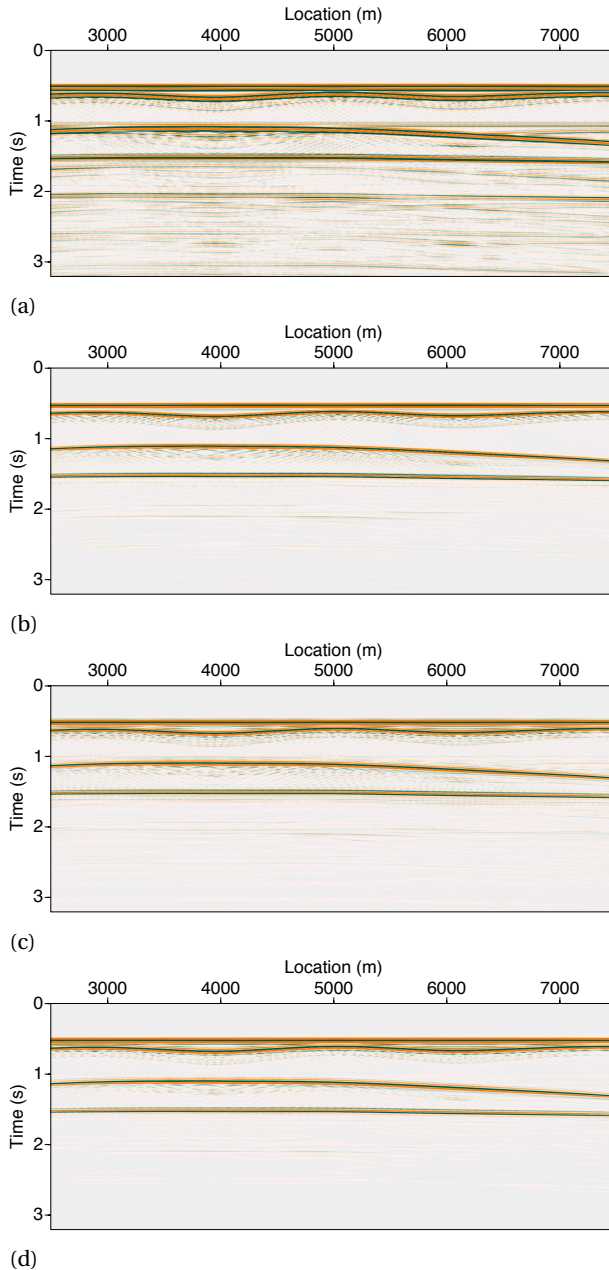
2

Figure 2.4: Results from extended CL-SRME for the synthetic data with a 25 m receiver ghost effect. a) Input stacked section including receiver ghost. b) Stacked section of modeled primaries. c) Stacked section of primaries after deghosting followed by CL-SRME. d) Stacked section of primaries after CL-SRME including the ghost.

of primaries, i.e., around the third event and below the bottom reflection. The ringing events above the bottom reflection already indicate that receiver deghosting was not accurate, and the results in the frequency domain confirm this (Figures 2.3a-2.3c). In the frequency domain, the notch effect of the ghost is visible at 30 Hz (Figure 2.3a), which corresponds to the cable depth of 25 m. In Figure 2.3c, there is still a clear imprint from the ghost notch that is supposed to be completely filled in (Figure 2.3b). In Figures 2.4a-2.4c, the input stacked section is compared with the stacked section of the reference primary data and with the stacked section after consecutive deghosting and CL-SRME.
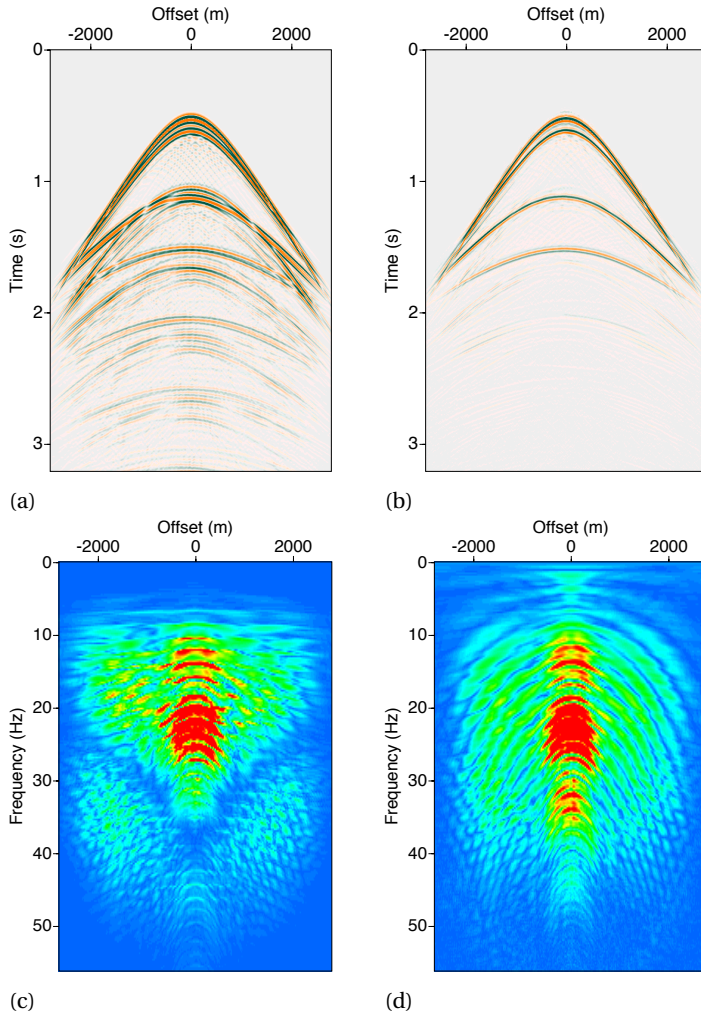

Figure 2.5: Results from CL-SRME with ghost effect for the input data with a 20-60 m slanted cable. a) Input shot with ghost. b) CL-SRME primaries. c) Input shot in the frequency domain. d) CL-SRME primaries in the frequency domain.

Again, it is visible that the surface-multiple energy leaked into the primary data domain after the cascaded approach.

The result for a single shot from CL-SRME including the receiver ghost is illustrated in Figure 2.2d. The primaries are estimated more accurately compared to the cascaded result (Figure 2.2c), and the sidelobes of the ghost events are better focused to a single event. The remaining surface-multiple energy around the third reflector and below the bottom reflector is better suppressed. However, there is sill some multiple energy visible. These events are also visible in the reference shot (Figure 2.2a); thus, they must be related to internal multiples. Only around offset 2000 m, below the bottom event, is some surface-multiple energy still present. After including the receiver ghost in CL-SRME, the notch effect is completely filled in (Figure 2.3d). Although there is some discrepancy for the amplitudes in the notch area, this result is significantly better than the cascaded case (Figure 2.3c). The same holds for the lower frequency area: Figure 2.3d shows an improved reconstruction of the information down to about 3Hz compared to Figure 2.3c. At less than 3 Hz, we see some inversion artifacts because for that range, the input data (Figure 2.3a) do not contain information. In Figure 2.4d, the stacked section after CL-SRME including the receiver ghost is illustrated. Again, a better surface-multiple removal is obtained; however, also internal multiples are a bit suppressed. Probably, relaxing the sparseness constraint can prevent the algorithm from doing this. Thus, including the ghost operator in CL-SRME gave a significant uplift, in the surface-multiple prediction and receiver deghosting, compared with applying a least-squares deghosting followed
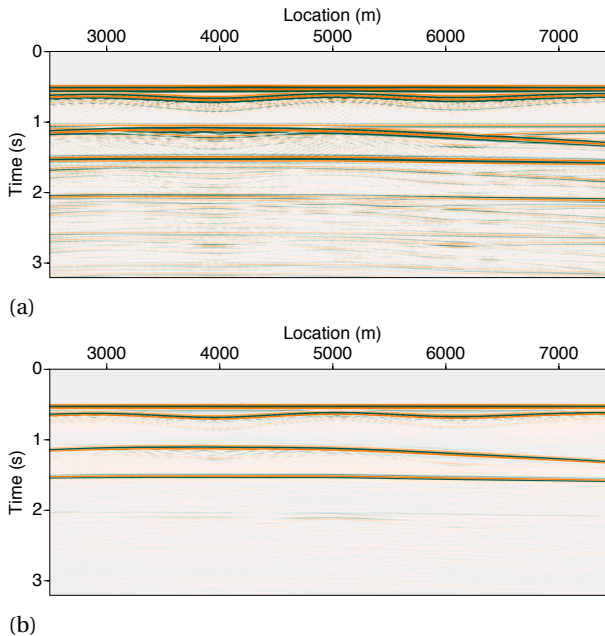

Figure 2.6: Results from CL-SRME for synthetic data with a 20-60 m slanted cable. a) Input stacked section with ghost. b) Stacked section of CL-SRME primaries.

by CL-SRME.

In the second case, the data are modeled using a slanted cable with a depth varying from 20 to 60 m. The results are illustrated in Figures 2.5 and 2.6. The deghosting effect for the slanted cable after including the ghost in CL-SRME is again quite accurate: The primary events that clearly display the slanted-cable ghost effect at the larger offsets (Figure 2.5a) are focused to one event after deghosting (Figure 2.5b). In the frequency domain (Figure 2.5c), the notch effect is visible and due to the slanted cable configuration; it becomes significantly more offset dependent compared with the fixed-depth case (Figure 2.3a). After extended CL-SRME (Figure 2.5d), the different order notches are filled in, although compared to the flat cable configuration, it is more noisy. In addition, more multiple energy leaked into the primary data domain compared with the flat cable situation, especially for larger offsets (see Figure 2.5b). The input stacked section in Figure 2.6a is compared with the output stacked section after extended CL-SRME in Figure 2.6b. Note again that somewhat more multiple energy leaked into the primary domain compared to the flat cable situation. These artifacts may come from the fact that in this method, an approximation for $[\mathbf{D}_j]^{-1}$ is used. Further research is needed to justify whether this is the reason for these artefacts.

2.5. BROADBAND FIELD DATA

Finally, we demonstrate the application of CL-SRME including the receiver ghost to a broadband (3-150 Hz) dataset from Australia, provided by CGG. CL-SRME is applied with the $\mathbf{D}_j$ operator now describing the effect of a slanted cable with a depth increasing from 8 to 57.5 m. The original source sampling is 37.5 m, and the original receiver sampling is 12.5 m. Reconstruction and near-offset interpolation are applied via a hybrid linear and parabolic Radon domain, respectively (see Verschuur et al., 2012) to obtain a source sampling and receiver sampling of 12.5 m and to fill in the near-offset data. CL-SRME is applied to a subset of 801 shots and receivers of this data set with a sampling of 2 ms. In Figure 2.7a, 2.8a, and 2.9a, the input data for CL-SRME are shown, respectively, in the shot, a magnified shot and a time-migrated domain. A band-pass filter and *f-k* filter are applied to the shots for display purposes. After time-migration, in addition, the spectrum is whitened. Figures 2.7b, 2.8b, and 2.9b are the ghost-free primaries, thus the outcome of CL-SRME. To delineate the effect of just the multiple removal, the ghost operator was applied to the final ghost-free result, as displayed in Figures 2.7c, 2.8c, and 2.9c. The estimated surface multiples are illustrated in Figures 2.7d, 2.8d, and 2.9d. The deghosting for the slanted cable after CL-SRME is quite accurate: the events at approximately 1.25s and 1.75s, indicated by the red arrows, that clearly display the slanted-cable ghost effect (Figures 2.7a, 2.7b, 2.8a, and 2.8b) become focused (Figures 2.7c and 2.8c). Also, the phase of the events is corrected by the algorithm. In Figures 2.7a and 2.8a, two surface multiples are indicated by the yellow arrows, and after CL-SRME (Figure 2.7c and 2.8c), most of the energy related to these surface multiples is removed. Nevertheless, overall in the shots, there is some surface-multiple energy left, so this can indicate that the wavelet is not yet estimated perfectly. The latter could be due to applying a 2D method to data with 3D amplitudes and/or due to an inaccurate near-offset interpo-
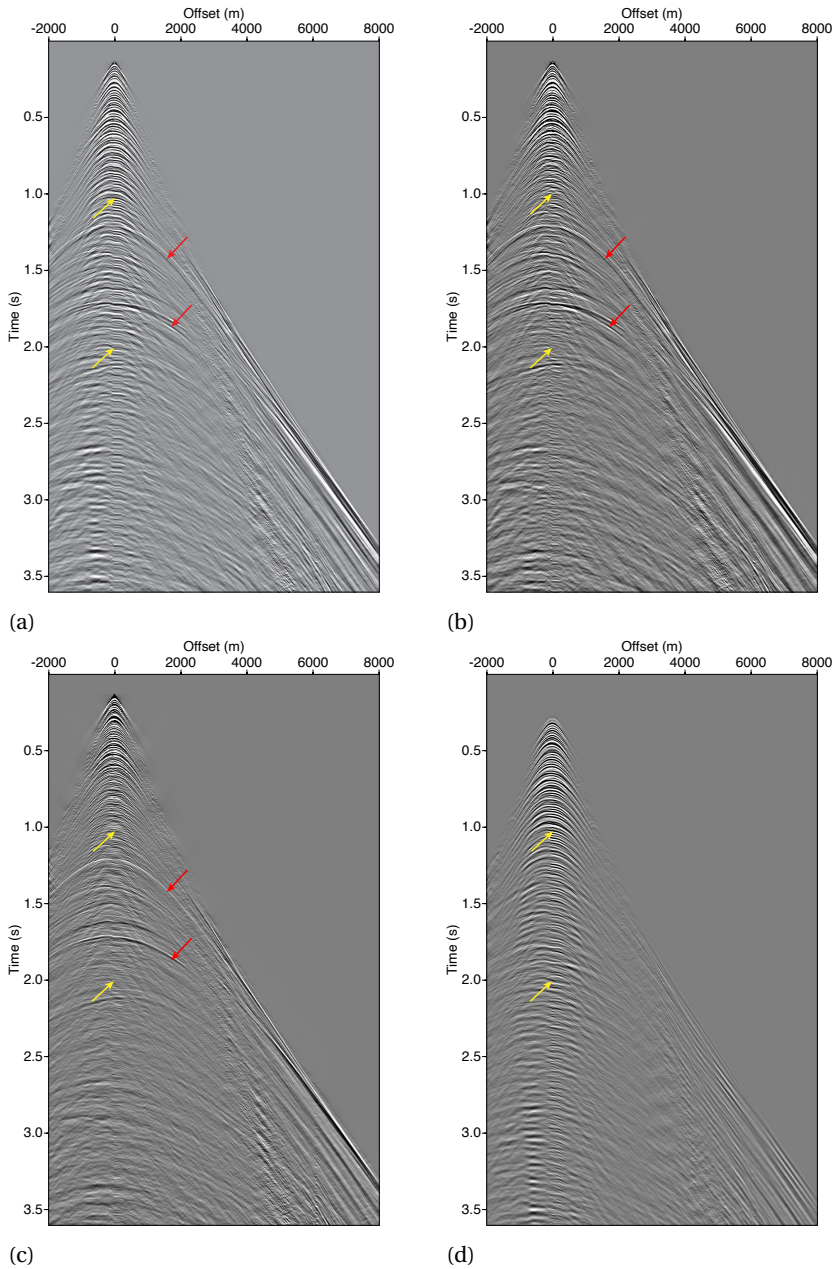
Figure 2.7: Results from CL-SRME for the field data with a slanted cable. The red arrows indicate receiver ghost effects, and the yellow arrows indicate surface multiples. a) Input shot with the ghost effect and surface multiples. b) CL-SRME primaries with the ghost effect. c) CL-SRME primaries without the ghost effect. d) CL-SRME surface multiples.
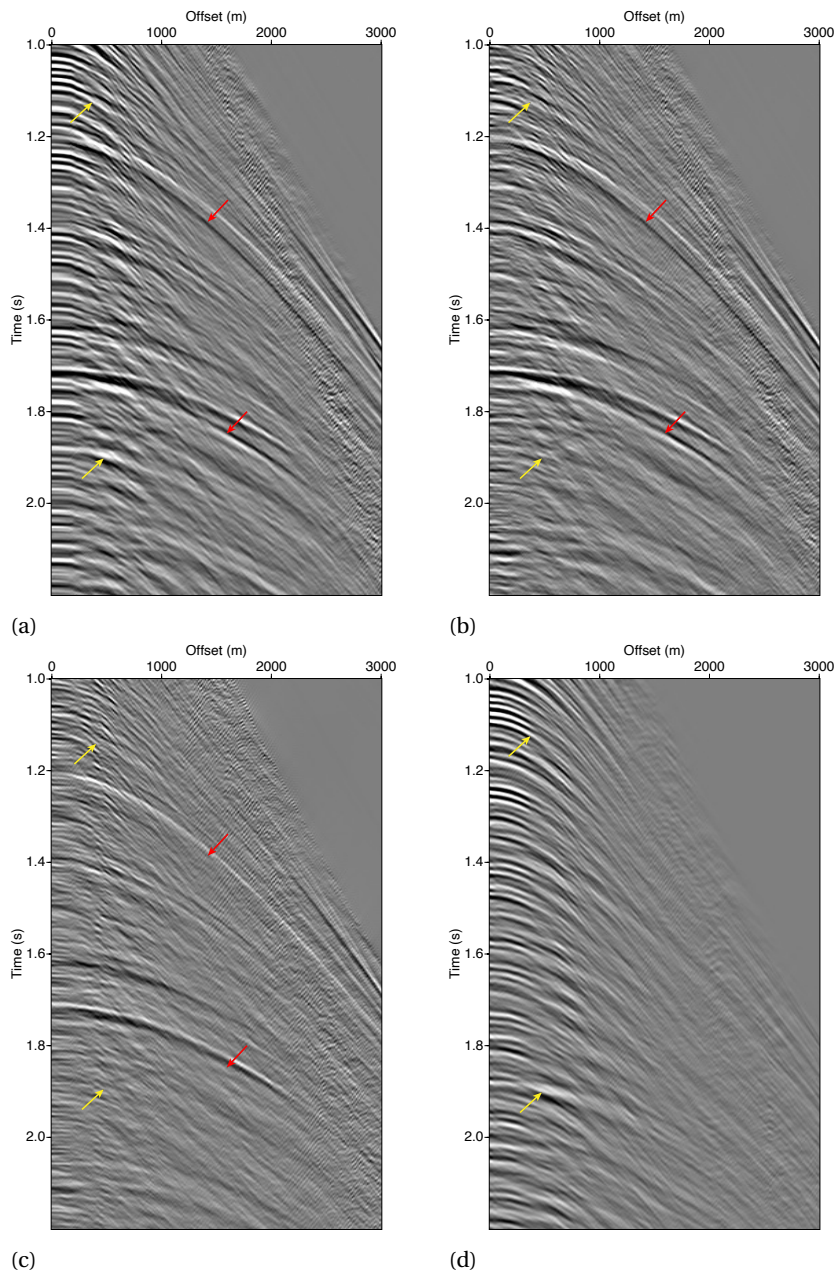
Figure 2.8: Magnified pictures from Figure 2.7. The red arrows indicate receiver ghost effects, and the yellow arrows indicate surface multiples. a) Input shot with the ghost effect and surface multiples. b) CL-SRME primaries with the ghost effect. c) CL-SRME primaries without the ghost effect. d) CL-SRME surface multiples.
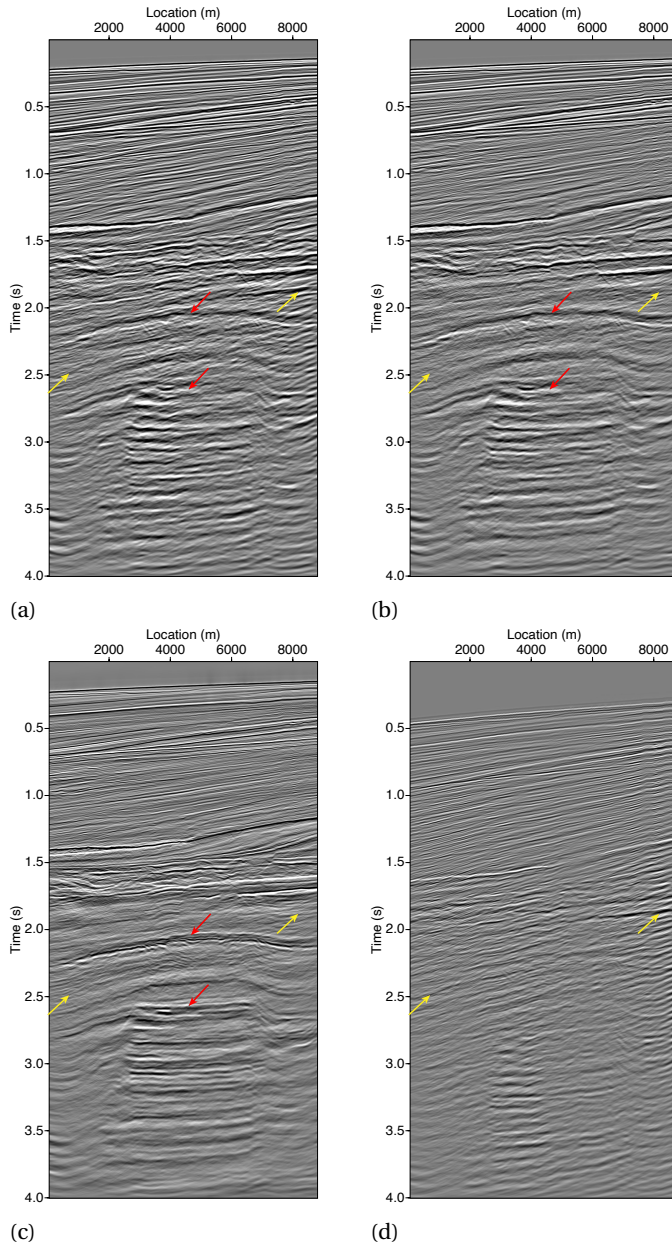
Figure 2.9: Results from CL-SRME for the field data with a slanted-cable ghost effect after time migration. The red arrows indicate receiver ghost effects, and the yellow arrows indicate surface multiples. a) Input time-migrated section with the ghost effect and surface multiples. b) CL-SRME time-migrated section for primaries with the ghost effect. c) CL-SRME time-migrated section for primaries without the ghost effect. d) CL-SRME time-migrated section for the surface multiples.

lation for this relatively shallow-water data set. On the other hand, if we focus on the time-migrated sections after CL-SRME most of the multiple energy is suppressed (see, i.e., the yellow arrows indicating multiples in Figures 2.9a-2.9c) and the resolution is significantly higher. For example, the red arrows in Figures 2.9a-2.9c indicate several events that become visible due to removing the ghost effect.

2.6. DISCUSSION

Most of the surface-multiple energy was removed from the field data, although there is some leakage into the primaries that probably can be handled by extending the CL-SRME to the full 3D case. The surface multiples will be matched as well as possible to the input data by the CL-SRME algorithm. However, a 2D approximation of wavefield propagation will never accurately explain wavefields that are 3D in practice. Especially, if there are dips present in the cross-line direction, which is very likely for this field data set, another cause for this surface-multiple leakage can be due to the limitations of near-offset interpolation for shallow reflectors. Lopez and Verschuur (2015) describe that it is possible to combine near-offset interpolation with CL-SRME by implementing the scheme in the focal domain. This approach will probably result in more accurate near offsets and surface multiples.

In a rough and or varying sea, the effective **R** is not equal to $-$**I**, especially for higher frequencies, see Orji et al. (2013). In practice, a wrong **R** will result in ringing events and to some extent, due to the L1-norm, the algorithm still would be able to suppress these effects. However, the algorithm can be helped by putting more prior knowledge of **R** in, if available. Another problem in practice is that exact knowledge of receiver locations is not available; there is always some uncertainty, and even a flat cable will have some depth variations along the streamer. This will result in a mismatch between estimated ghost and input data; however, to some extent, again due to the L1-norm, the algorithm still would be able to suppress these effects. Another way to handle these uncertainties can be estimating the ghost operator adaptively during the CL-SRME process.

An alternative to the method proposed in this chapter is to apply a more sophisticated receiver deghosting and CL-SRME in a cascaded manner. A dedicated deghosting algorithm can be implemented in a closed-loop manner without the surface-multiple prediction. In chapter 3 we introduce a dedicated deghosting closed-loop algorithm that is also able to adapt to small errors in the propagation operator. In Wang et al. (2014), a similar method is combined with interpolation in the crossline direction to make it applicable to 3D data with coarse sampling in one direction. In this chapter, we only demonstrate the limitations of a standard deghosting procedure followed by CL-SRME.

Note that the integrated solution is more efficient, the extra cost of CL-SRME when including the ghost effect is relatively low compared with standard CL-SRME: It is approximately 10%-15% more expensive in case of a slanted cable.

2.7. CONCLUSIONS

We demonstrated that the CL-SRME algorithm can be extended to handle receiver ghost effects. In the slanted cable case, we took into account that it is not valid to cancel out the ghost operators in the multiple prediction term. As a result we used an approximate inverse ghost operator during the multiple prediction process. The results after CL-SRME including the slanted-cable ghost effect for synthetic and field data are quite accurate. Minor residual surface multiple in the output may be due to using an approximate inverse ghost operator during the prediction. Extending this method to the full 3D case will be necessary to further improve the field data results.

3

ADAPTIVE ESTIMATION OF THE UPGOING WAVEFIELD

The estimation of the upgoing wavefield based on a ghost model is a well-known step in receiver deghosting. The shape of the rough and dynamic (time-varying) sea surface and the varying receiver depth should be included to carry out this step correctly. However, the exact shape of the dynamic sea surface is not commonly measured. Therefore, the ghost model is often inaccurate, introducing artifacts in the deghosted result. We have developed a data-driven, iterative, receiver deghosting method that includes the estimation of the dynamic shape of the sea surface and the varying receiver depth. The deghosting algorithm is based on, respectively, wavefield propagation from the varying receiver level up to the dynamic sea surface and wavefield propagation from the dynamic sea surface down to the varying receiver level. The depth of the receivers relative to the height of the dynamic sea surface is estimated and updated at each iteration. We validate the deghosting method on 2D simulated data recorded on a variable depth and 2D simulated data recorded with a dynamic sea surface. Our deghosting method gives a significant uplift on the simulated data, given that the initial ghost model is inaccurate. On the field data, recorded with a midwater, quasi-stationary cable, our deghosting method is able to correct the receiver depth and provides an accurate deghosting result. The performance of the deghosting method is similar to the performance of a multi-component decomposition method in this realistic scenario.

31

3.1. INTRODUCTION

In marine seismic acquisition, the receivers are located under the sea surface. Consequently, they first measure the upgoing wavefield and then, after some time, its reflection at the water-air interface, which is a downgoing wavefield. Due to the large impedance contrast between water and air, the reflection coefficient is very close to -1. The recorded, downgoing wavefield, being the receiver-side ghost wavefield, is related to the depth of the receivers and the shape of the sea surface. The same mechanism also generates the source-side ghost wavefield. The ghost wavefield causes interference in the wavenumber-frequency domain. Constructive interference causes a 6 dB signal enhancement at the so-called peaks of the spectrum, whereas destructive interference annihilates the signal in the so-called notches of the spectrum. The presence of the notches in the spectrum limits the usable bandwidth and interpretability of marine seismic data. Hence, removal of the ghost wavefield, referred to as deghosting, increases the usable bandwidth and improves the interpretability of the data. In conventional marine acquisition, pressure-only data are acquired at a constant streamer depth. Modern acquisition systems, however, may have a variable receiver depth (Soubaras and Dowle, 2010). At the source side, there are similar variable-depth acquisition systems (Caporal et al., 2018; Parkes and Hegna, 2011). The image resolution for constant and variable-depth acquisition improves after elimination of the ghost wavefield in processing, or, equivalently, after estimation of the upgoing wavefield (Amundsen et al., 2013; Ferber and Beasley, 2014; Robertsson et al., 2014; Soubaras, 2010; Wang and Peng, 2012). Multi- or dual-component sensors record the pressure and the vertical component of the particle velocity of a wavefield, which means that the free surface condition between those components is consistent. By combining the pressure and the vertical component of the particle velocity, the wavefield at the receiver side can be decomposed (and hence be deghosted) into the upgoing and downgoing pressure wavefield (Caprioli et al., 2012; Day et al., 2013; Tenghamn et al., 2007a).

This chapter focuses on pressure-only data, and we aim at removing the receiver-side ghost wavefield by processing based on a ghost model. Often, deghosting methods assume vertical wavefield propagation. The limitation of this assumption is evident in the wavenumber-frequency domain, in which the ghost notch is angle dependent (e.g., Amundsen, 1993). Under this assumption, it is not possible to properly take into account a rough sea surface and variable receiver level. A rough sea surface affects the travel-times and amplitude of the ghost wavefield. Therefore, some residual would be left in the data after deghosting, which usually appears as a ringing phenomenon (e.g., Egorov et al., 2018). In addition to the shape of the sea surface, the time-varying nature of the rough sea surface, referred to as a dynamic sea surface, will affect the ghost wavefield as well (e.g., Cecconello et al., 2017). There are numerous deghosting algorithms that make an effort to adapt to a dynamic sea surface. The effect of a dynamic surface can be approximated by a frequency- and angle-dependent reflectivity coefficient (Masoomzadeh et al., 2013; Orji et al., 2013). Blacquière and Sertlek (2018) demonstrate that the improvement provided by this approach is rather modest. More sophisticated methods based on wave propagation in the Radon domain are able to take into account smooth variations

of the height of the sea surface and variations of the receiver depth over a longer spatial distance (King and Poole, 2015; Masoomzadeh et al., 2013; Rickett et al., 2014). The forward propagation from the receiver level up to the sea surface and the subsequent forward propagation from the sea surface down to the receiver level are often combined in one step. This approach does not accurately describe wavefield propagation of the ghost wavefield, when the dynamic shape of the sea surface combined with a flat or variable receiver depth has a significant effect on the ghost wavefield. However, Grion and Telling (2016) use propagation operators in a two-step approach, respectively, from the receiver level up to the sea surface and from the sea surface down to the receiver level. The exact shape of the dynamic sea surface is required to calculate the correct propagation operators. However, in practice, this information is usually not available. There are several methods to estimate it from recorded data. Kragh et al. (2004) use the very low frequencies for this purpose. King and Poole (2015) calculate the shape of the sea surface with extrapolation and cross-correlation as an independent operation. Grion and Telling (2016) extract the shape of the sea surface from the frequency spectrum. Estimating spatial and temporal variations related to the ghost model from the seismic measurements with these methods is not trivial and it is likely that errors will propagate into the deghosted result.

We propose an inversion method that is based on the propagation operators that are able to account for changes in the height of the sea surface and variations of the receiver depth, not only over large spatial distances but also over short distances. The method is adaptive, i.e., the ghost model estimation is integrated in the deghosting process. Therefore, the method is more hands-off compared to other methods in the literature (Grion and Telling, 2017; King and Poole, 2015; Kragh et al., 2004).

First, we describe the theoretical framework of the data including the ghost effect. Then, we continue with the introduction of a deghosting algorithm that can handle a priori information of a variable receiver level as well as a rough, but static, sea surface. This method, referred to as deterministic deghosting, assumes that the parameters to calculate the ghost model are known. After that, we extend the deterministic deghosting method to a single time-window, adaptive deghosting method that can handle the unknown shape of the sea surface with respect to a flat or variable receiver depth. The multi time-window implementation, based on the work of Grion and Telling (2017), of this adaptive deghosting method is able to account for the dynamic character of the ghost model.

In the first example, numerical data are used to illustrate the effect of an inaccurate receiver depth in the ghost model for the case of deterministic deghosting. In addition, this example shows that the single time-window, adaptive deghosting method corrects errors related to the receiver depth with respect to the sea surface. This gives a significant uplift to the deghosted data. The second example illustrates that including the dynamics of the ghost model by using multiple time windows leads to an additional uplift of the deghosting result. In the final example, we apply deterministic and multi time-window adaptive deghosting to field data, acquired with a midwater cable system (Haumonte et al., 2016).

3.2. GHOST MODEL

The water surface reflectivity at the sea surface $z_0(x, y, t)$ is very close to -1 due to the large impedance contrast between water and air. Therefore, the combination of an upgoing and a downgoing wavefield is measured at the receiver level $z_d(x, y, t)$: The upgoing is the one that directly traveled up, and the downgoing one is its reflection from the sea surface. The latter is the so-called ghost wavefield at the receiver side. For a rough, yet stationary sea surface, i.e., ignoring the temporal dynamics for the moment, and following the matrix notation introduced by Berkhout (1985), monochromatic shot record $\vec{P}_j$, including the receiver ghost wavefield, can be formulated as:

$$\vec{P}_j(z_d; z_s) = \mathbf{D}_j(z_d)\mathbf{G}_j(z_d, z_d)\mathbf{X}(z_d, z_s)\vec{S}_j(z_s), \qquad (3.1)$$

where index j refers to the jth record, $\vec{S}_j$ describes the source properties including the ghost effect at the source side, $\mathbf{X}$ is the earth transfer function, and $\mathbf{D}$ describes the receiver distribution related to record j and its properties. Here, the ghost matrix at the receiver side for a single shot record is given by

$$\mathbf{G}_j(z_d, z_d) = \mathbf{I} - \mathbf{W}_j(z_d, z_0)\mathbf{W}_j(z_0, z_d), \qquad (3.2)$$

where $\mathbf{I}$ is the identity matrix, $\mathbf{W}_j(z_0, z_d)$ describes forward propagation from the receiver level up to the sea surface, $\mathbf{W}_j(z_d, z_0)$ describes forward propagation from the sea surface down to the receiver level, and the minus sign represents the strong sea surface reflectivity of -1. We now discuss how to compute the forward propagation for several situations related to the shape of the sea surface and the location of the receivers. Forward propagation in a homogenous medium from a flat sea surface to a varying receiver level is identical to the discrete implementation of the Rayleigh II integral (e.g., Berkhout, 1985; Gisolf and Verschuur, 2010; Wapenaar and Berkhout, 1989) for 3D wavefield extrapolation in the space-frequency domain. The rows of the propagation operator in $\mathbf{W}_j(z_d(x, y), z_0)$ are given by

$$\vec{W}_i^\dagger(z_d(x_i, y_i), z_0) = \mathscr{F}_{xy}^{-1}\left\{e^{j(k_x x_i + k_y y_i)}e^{-j\sqrt{k^2 - k_x^2 - k_y^2}|z_0 - z_d(x_i, y_i)|}\right\}, \qquad (3.3)$$

with the dagger symbol $\dagger$ indicating a row vector, $\mathscr{F}_{xy}^{-1}$ representing the inverse Fourier transform over the spatial wavenumbers k_x and k_y, $k = \omega/c$ representing the wavenumber, c being the propagation velocity in water and ω being the angular frequency. The
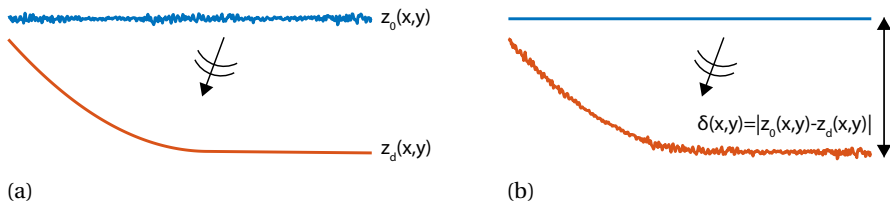

Figure 3.1: a). Propagation from a rough sea surface to a varying receiver level. b) Propagation from a flat sea surface to a varying receiver level including the shape of the initial surface using equation 3.3.

ith row propagates the wavefield to the lateral location (x_i, y_i) at the receiver level. We describe forward wavefield propagation from a flat receiver level to a rough sea surface in a similar way with the propagation operator $\mathbf{W}_j(z_0(x, y), z_d)$. An approximation of the forward wavefield propagation operator from a rough sea surface to a planar receiver level is given by

$$\mathbf{W}_j(z_d, z_0(x, y)) \approx \left[\mathbf{W}_j(z_0(x, y), z_d) \right]^T, \tag{3.4}$$

where T denotes the matrix transpose. Equation 3.4 is only exact for propagation from a planar initial surface. Figure 3.1 illustrates the situation for propagation from a rough sea surface $z_0(x, y)$ to a varying receiver level $z_d(x, y)$ versus propagation from a flat surface to a varying level that is a combination of the varying receiver level and the rough sea surface. Equations 3.3 and 3.4 do not properly take into account an arbitrary shaped initial surface (e.g., Berkhout, 1985; Gisolf and Verschuur, 2010; Wapenaar and Berkhout, 1989). Therefore, the forward propagated wavefield has an amplitude error, if the initial surface is non-flat. This amplitude error is relatively small for a mildly curved initial surface (Sun et al., 2018; van den Berg and Fokkema, 1980). The exact wavefield propagation operator from a rough sea surface to a planar receiver level is given by

$$\mathbf{W}_j(z_d, z_0(x, y)) = \left[\mathbf{F}_j(z_0(x, y), z_d) \right]^{-1}, \tag{3.5}$$

with $\mathbf{F}_j(z_0(x, y), z_d)$ representing the backward-propagation operator from a planar receiver level to a rough sea surface. Sun et al. (2018) combine equations 3.3 and 3.5 to describe forward propagation in two steps from a varying receiver level, to an intermediate planar surface z_i, with $\left[\mathbf{F}_j(z_d(x, y), z_i) \right]^{-1}$, to the rough sea surface with $\mathbf{W}_j(z_0(x, y), z_i)$. Followed by another two-step propagation from the rough sea surface, to the intermediate planar surface with $\left[\mathbf{F}_j(z_0(x, y), z_i) \right]^{-1}$, to the varying receiver level with $\mathbf{W}_j(z_d(x, y), z_i)$. Note that calculating the inverse of the backward-propagation operator is computationally expensive, especially for large matrices.

In the case of an ideal spatial receiver sampling, i.e., sampling according to the Nyquist criterion, with unit receivers, and a unit source, equation 3.1 becomes

$$\vec{P}_j(z_d; z_0) = \mathbf{G}_j(z_d, z_d) \vec{X}_j(z_d, z_0). \tag{3.6}$$

where vector $\vec{X}_j(z_d, z_0)$ now corresponds to the deghosted shot record, being identical to the upgoing wavefield at the receiver level.

3.3. DETERMINISTIC DEGHOSTING

Our aim is to develop an inversion procedure to estimate the upgoing wavefield $\hat{X}_j$ (where the caret accent ˆ indicates an estimated version of $\vec{X}_j$), such that once we "add" the ghost, $\mathbf{G}\hat{X}_j$, the result is equal to the measured shot record $\vec{P}_j$. In this deterministic deghosting method, prior information of the receiver level and the rough, static sea surface is required to calculate the ghost model. The dynamic character of the sea surface will be discussed in the next section. Because of the notches in the spectrum of the data with ghost, the solution is not unique: i.e., we are dealing with an underdetermined system. This means that we have to provide additional information. We assume that of all

possible solutions, the one we look for is the sparsest in the space-time domain. There-
fore, we include a sparsity-promoting regularization term in the objective function:

$$J = J_1 + J_2, \text{with } J_1 = \sum_\omega ||\hat{V}_j||_F \text{ and } J_2 = \lambda \sum_t ||\hat{x}_j||. \tag{3.12}$$

Here, $\hat{V}_j = \vec{P}_j - \mathbf{G}_j \hat{X}_j$ is the residual, subscript F refers to the Frobenius norm, ω is the
angular frequency, $\hat{x}_j$ is the estimated ghost-free data in the time domain, and t is the
time. The residual term J_1 ensures that the inversion procedure indeed leads to a solu-
tion. The sparsity-promoting L_1-regularization term J_2 ensures that the procedure leads
to the desired solution. Here, λ is a user-defined regularization constant whose optimal
value depends on the signal-to-noise ratio (S/N). Note that according to Parseval's theo-
rem, the residual could be evaluated in the space-frequency domain (as shown in equa-
tion 3.12) or in the space-time domain with the exact same result. Because we apply the
ghost operator in the space-frequency domain, we define the residual in that domain.
We use a steepest-descent method to solve equation 3.12 with respect to the ghost-free
data (see Algorithm 1). At each iteration i, the gradient with respect to $\hat{X}_j$ is calculated

---

Algorithm 1: Steepest-descent method for deterministic deghosting

Initialization: $i \Leftarrow 0$, $\hat{X}_j^{(0)} \Leftarrow 0$ and $\hat{V}_j^{(0)} \Leftarrow \vec{P}_j$.
Calculate $\mathbf{G}_j$ (see equation 4.2).
while *stopping criterium is not satisfied* **do**

Compute gradient of J_1 with respect to $\hat{X}_j$ for each ω (proof in Appendix A):

$$\nabla_{\hat{X}_j^{(i)}} J_1 \Leftarrow -2\mathbf{G}_j^H \hat{V}_j^{(i)}, \tag{3.7}$$

Compute gradient of $J_2 = \lambda \sum_t ||\hat{x}_j||$ from equation 3.12 with respect to $\hat{x}_j$ for
each t:

$$\nabla_{\hat{x}_j^{(i)}} J_2 \Leftarrow \lambda \cdot \text{sgn}(\hat{x}_j^{(i)}). \tag{3.8}$$

Adding equations 3.7 and 3.8 gives the total gradient:

$$\Delta \hat{X}_j^{(i)} \Leftarrow \nabla_{\hat{X}_j^{(i)}} J_1 + \nabla_{\hat{X}_j^{(i)}} J_2, \tag{3.9}$$

where $\nabla_{\hat{X}_j^{(i)}} J_2$ is the temporal Fourier transform of $\nabla_{\hat{x}_j^{(i)}} J_2$.
Update $\hat{X}_j^{(i)}$ using α subject to $J \to min$:

$$\hat{X}_j^{(i+1)} \Leftarrow \hat{X}_j^{(i)} + \alpha \Delta \hat{X}_j^{(i)}. \tag{3.10}$$

Update iteration number: $i \Leftarrow i+1$, and calculate new residual:

$$\hat{V}_j^{(i)} \Leftarrow \vec{P}_j - \mathbf{G}_j \hat{X}_j^{(i)}. \tag{3.11}$$

end

to update $\hat{X}_j$, see equations 3.7-3.10. The step size α in equation 3.10 is computed by a line search such that $J(\hat{X}_j^{(i+1)}) = J(\hat{X}_j^{(i)} + \alpha\Delta\hat{X}_j^{(i)})$, with $\Delta\hat{X}_j^{(i)} = \nabla_{\hat{X}_j^{(i)}} J(\hat{X}_j^{(i)})$, is minimized. Alternatively, other gradient methods (e.g., conjugate gradient) could be implemented to increase the rate of convergence.

3.4. EXTENSION TO ADAPTIVE DEGHOSTING

To be able to deal with the dynamics of the sea surface and the receiver depth, we include the estimation of the ghost model in our deghosting scheme. We call this adaptive deghosting. The ghost model is parameterized with the depth of the cable for each location, $z_d(x, y, t)$, and the level of the sea surface, $z_0(x, y, t)$. To reduce the number of parameters, we introduce $\delta(x, y, t)$, being the difference between z_d and z_0. The objective function given by equation 3.12 is then minimized with respect to $\vec{X}_j$ and δ (see Algorithm 2). If both the levels z_0 and z_d are unknown we are limited to use the approximate solution given by equations 3.3 and 3.4. This might result in an amplitude mismatch between estimated ghost and input data for a rough sea surface and varying receiver level. In that case the sparsity constraint needs to reduce the artefacts due to this amplitude mismatch. If z_0 or z_d is known, then δ can be the difference between the unknown level and an intermediate level, such that the deghosting algorithm can use the exact propagation operators.

We use multiple time windows to handle the dynamic property of the ghost model. Each time window may have its own specific, time-invariant ghost model. Grion and Telling (2017) demonstrate that such an approach provides accurate results. In Algorithm 2, the subscript m indicates a single time window and M is the total number of time windows; i.e., $\delta(x, y, t)$ is replaced by M versions of $\delta_m(x, y)$. Furthermore, we put the scalars $\delta_m(x, y)$ along the diagonal of a matrix $\hat{\mathcal{D}}_m$. Based on the estimated ghost model parameters $\hat{\delta}_m$, we calculate the ghost operator $\hat{\mathbf{G}}_m$ for each time window. Here, the caret accent $\hat{}$ represents the estimated versions of δ_m and $\mathbf{G}_m$, respectively. A multi time-window approach might introduce artifacts for events that are close to the edges of a window. To reduce such effects, there is an area of overlap in the time domain. The $\prod$-sign indicates a concatenation of windows and the symbols $\mathcal{F}$ and $\mathcal{F}^{-1}$ represent, respectively, the Fourier and inverse Fourier transform (see equations 3.17 and 3.20). Note that we include a ghost operator in the calculation of step sizes α and β. The algorithm updates the estimates of the ghost-free data $\hat{X}_{j,m}$ and the ghost-model parameter, $\hat{\delta}_m$, in a flip-flop manner. In the adaptive scheme, the update of the ghost-free data for a single time-window is identical to its update in the non-adaptive scheme (see equations 3.13-3.16). In equation 3.18 the gradient of the objective function with respect to $\hat{\mathcal{D}}_m$ is given. In equation 3.19, we use this gradient to update the distance $\hat{\delta}_m$, which is used to calculate a new estimate of the ghost operator $\hat{\mathbf{G}}_m$. We enforce causality by muting predicted events before the first event. The cost of a single update of the ghost-model parameter and single update of the ghost-free data are similar in the different deghosting schemes. The examples in this Chapter require 10-15 iterations for the ghost model parameter, approximately 100 iterations for the ghost-free data and the computational cost of the multi time-window implementation is two to three times higher than the cost of the

3

single-

Algorithm 2: Steepest-descent method for adaptive deghosting

---

for *time windows* $m = 1$ *to* M **do**

> Initialization: $i \Leftarrow 0$, $\hat{X}_{j,m}^{(0)} \Leftarrow 0$, $\hat{V}_{j,m}^{(0)} \Leftarrow \vec{P}_{j,m}$, $\hat{\delta}_m \Leftarrow \vec{\delta}_{init}$.
>
> Calculate $\hat{\mathbf{G}}_{j,m}^{(0)}$ (see equation 4.2).

end

while *stopping criterium is not satisfied* **do**

> **for** *time windows* $m = 1$ *to* M **do**
>
>> Compute gradient of $J_{1,m}$ with respect to $\hat{X}_{j,m}$ for each ω (proof in Appendix A):
>>
>> $$\nabla_{\hat{X}_{j,m}^{(i)}} J_{1,m} \Leftarrow -2[\hat{\mathbf{G}}_{j,m}^{(i)}]^H \hat{V}_{j,m}^{(i)}, \tag{3.13}$$
>>
>> Compute gradient of $J_{2,m}$ with respect to $\hat{x}_j$ for each t:
>>
>> $$\nabla_{\hat{x}_{j,m}^{(i)}} J_2 \Leftarrow \lambda \cdot \text{sgn}(\hat{x}_{j,m}^{(i)}). \tag{3.14}$$
>>
>> Adding equations 3.13 and 3.14 gives the total gradient:
>>
>> $$\Delta \hat{X}_{j,m}^{(i)} \Leftarrow \nabla_{\hat{X}_{j,m}^{(i)}} J_{1,m} + \nabla_{\hat{X}_{j,m}^{(i)}} J_{2,m}, \tag{3.15}$$
>>
>> where $\nabla_{\hat{X}_{j,m}^{(i)}} J_2$ is the temporal Fourier transform of $\nabla_{\hat{x}_{j,m}^{(i)}} J_2$.
>>
>> Update $\hat{X}_{j,m}^{(i)}$ using α subject to $J_m \rightarrow min$:
>>
>> $$\hat{X}_{j,m}^{(i+1)} \Leftarrow \hat{X}_{j,m}^{(i)} + \alpha \Delta \hat{X}_{j,m}^{(i)}. \tag{3.16}$$
>
> **end**
>
> Update iteration number: $i \Leftarrow i + 1$, concatenate windows and calculate new residual:
>
> $$\vec{V}_j^{(i)} \Leftarrow \vec{P}_j - \mathscr{F}\left\{ \prod_{m=1}^M \mathscr{F}^{-1}\{\hat{\mathbf{G}}_{j,m}\hat{X}_{j,m}^{(i)}\} \right\} \tag{3.17}$$
>
> **for** *time windows* $m = 1$ *to* M **do**
>
>> Compute gradient of equation 3.12 with respect to $\hat{\mathcal{D}}_m$ (proof in Appendix A):
>>
>> $$\nabla_{\hat{\mathcal{D}}_m^{(i)}} J_m \Leftarrow -\sum_\omega \left[\frac{d\mathbf{G}_{j,m}^{(i)*}}{d\Re\hat{\mathcal{D}}_m^{(i)}} \right] \hat{V}_{j,m}^{(i)} [\hat{X}_{j,m}^{(i)}]^H. \tag{3.18}$$
>>
>> Update $\hat{\delta}_m$ using β subject to $J_m \rightarrow min$:
>>
>> $$\hat{\delta}_m^{(i+1)} \Leftarrow \hat{\delta}_m^{(i)} + \beta diag(\nabla_{\hat{\mathcal{D}}_m^{(i)}} J_m). \tag{3.19}$$
>>
>> Calculate $\hat{\mathbf{G}}_{j,m}^{(i+1)}$ using $\hat{\delta}_m^{(i+1)}$.
>> Update iteration number: $i \Leftarrow i + 1$.
>
> **end**
>
> Concatenate windows and calculate new residual:
>
> $$\hat{V}_j^{(i)} \Leftarrow \vec{P}_j - \mathscr{F}\left\{ \prod_{m=1}^M \mathscr{F}^{-1}\{\hat{\mathbf{G}}_{j,m}^{(i)}\hat{X}_{j,m}^{(i)}\} \right\}. \tag{3.20}$$

end

---

time-window implementation. The algorithm is stopped when the objective function is approximately 0.1% of its initial value.

Solving the following relation gives an estimate of the window size t_m:

$$\left| 4hcos(\frac{2\pi x}{\lambda} + \frac{\pi t_m}{T_p})sin(\frac{\pi t_m}{T_p}) \right| \geq \frac{c}{4f_{max}}, \tag{3.21}$$

where the left side is the absolute difference between two harmonic sea-surface waves, with h being the wave height, T_p the peak wave period, λ the wavelength of the sea surface wave, and x the spatial location. The left side is multiplied by two to take into account that waves travel upward to the sea surface and downward from the sea surface. The peak wave period and wavelength of the sea surface wave are calculated from the wave height according to Pierson and Moskowitz (1964). The right side is the vertical seismic resolution, with c being the propagation velocity in water and f_{max} the maximum frequency of the seismic wavefield. We use the smallest window size that solves equation 3.21 in the multi time-window adaptive deghosting algorithm. If there are no solutions, or if the window size exceeds the recording time, the sea surface does not strongly affect the seismic data and the single-time-window, adaptive deghosting algorithm is sufficient. Because a harmonic wave is a rather simplified representation of the sea surface, some tuning of the window size could give an uplift to the deghosting results.

3.5. NUMERICAL EXAMPLE

We use the velocity model from Figure 3.2 in a finite-difference scheme to generate a 2D shot record with receiver ghost and also a version without a receiver ghost (i.e., containing the upgoing wavefield only) as a reference. The source is very close to the sea surface, and the receiver spacing in the lateral direction is 5 m. The receiver depth geometry is slanted, ranging from 10 to 80 m including small depth variations along the
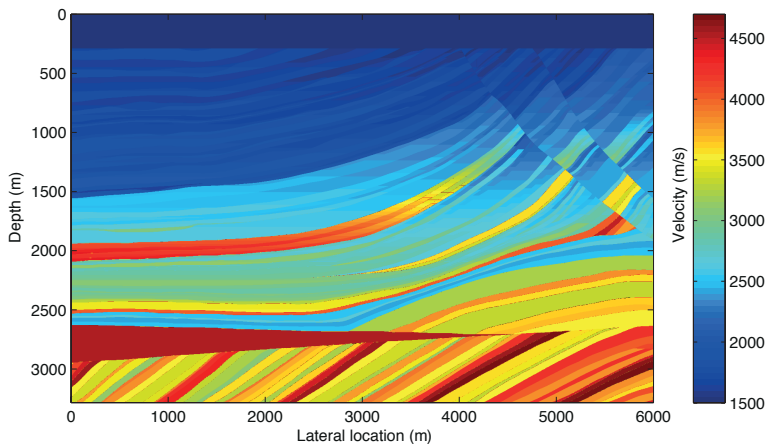

Figure 3.2: Velocity model for the acoustic finite-difference modeling including a water layer at the top

line (see Figure 3.3). The sea surface is flat, so there is no dynamic effect in this synthetic example. We show the shot record and a magnified inlay in Figure 3.4a in the time domain. In Figure 3.5a we show the shot record in the frequency domain. There are clear notches, related to the slanted cable. We use 2D propagation operators for deterministic and adaptive deghosting of the numerical data. First, we carry out deterministic deghosting using the actual ghost model (see Figure 3.4c). We use the difference with the modeled upgoing wavefield (Figure 3.4b) given in Figure 3.4f to validate the result. The difference is quantified by the signal-to-noise ratio (S/N) as follows:

$$S/N = 10 log \Big(\sum_x \sum_t \frac{|\vec{x}_j|^2}{|\hat{\vec{x}}_j - \vec{x}_j|^2} \Big),$$
(3.22)

with $\vec{x}_j$ being the modeled upgoing wavefield and $\hat{x}_j$ the estimated upgoing wavefield after deghosting in the space-time domain.

The S/N for deterministic deghosting is equal to 18.1 dB. Then, we use an inaccurate ghost model for deghosting. The geometry of this inaccurate model has an average error of 2 m with respect to the actual cable geometry (Figure 3.3). Applying the inaccurate ghost model with deterministic deghosting has a destructive effect on the result (see Figures 3.4d, 3.4g, and 3.5d). Artifacts may be observed, resulting in a very poor S/N of −1.0 dB. The poor deghosting result is also clear from the overamplified notches in the spectrum of Figure 3.5d. Figures 3.4e, 3.4h and 3.5e show the adaptive result, initialized with the same inaccurate ghost model. This gives a significant uplift to an S/N of 15.1 dB, which is rather close to the 18.1 dB that was reached for the deterministic case with the correct receiver depth. Figure 3.3 shows the obtained cable geometry, which resembles the correct cable geometry quite well. The ringing artifacts are almost completely gone (Figure 3.4e), and the notches in the frequency spectrum are filled with the correct amplitude.
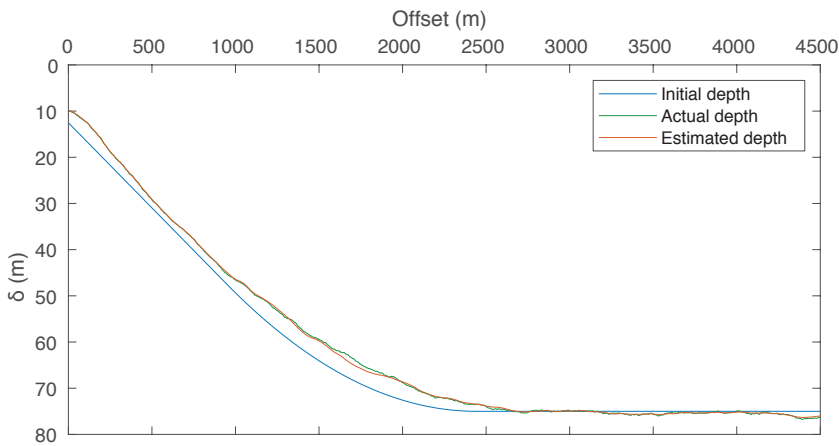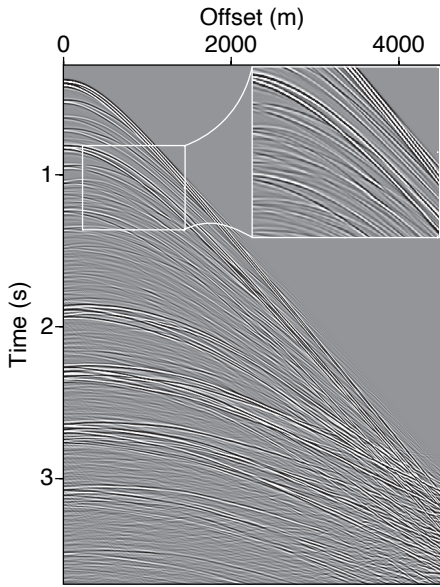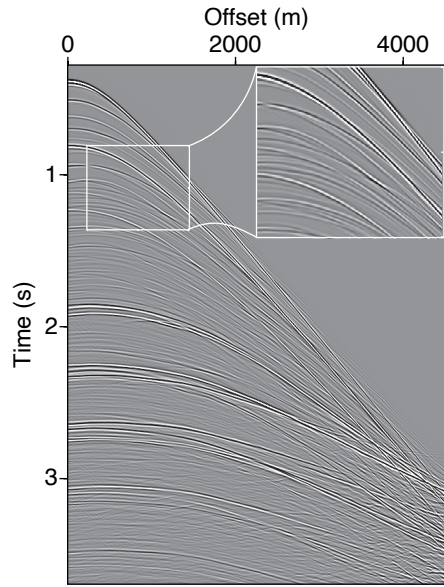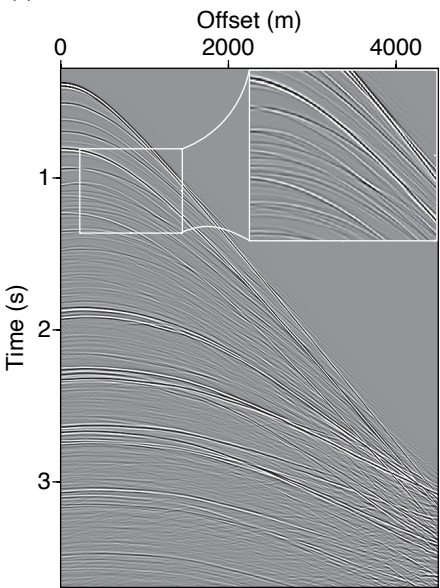

Figure 3.3: The actual depth of detectors is used for deterministic deghosting with actual ghost model, the initial depth is used for deterministic deghosting with inaccurate ghost model and starting ghost model for adaptive deghosting method and the estimated depth is obtained after adaptive deghosting.
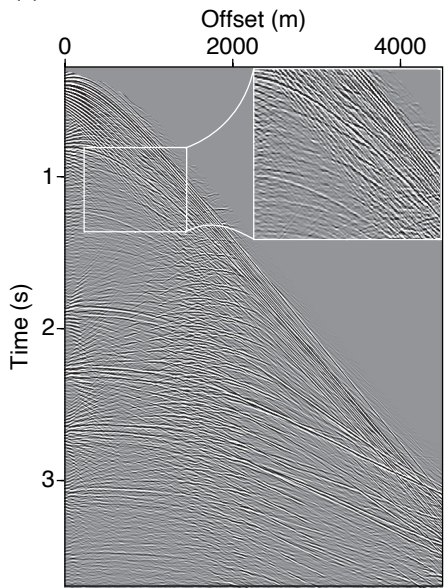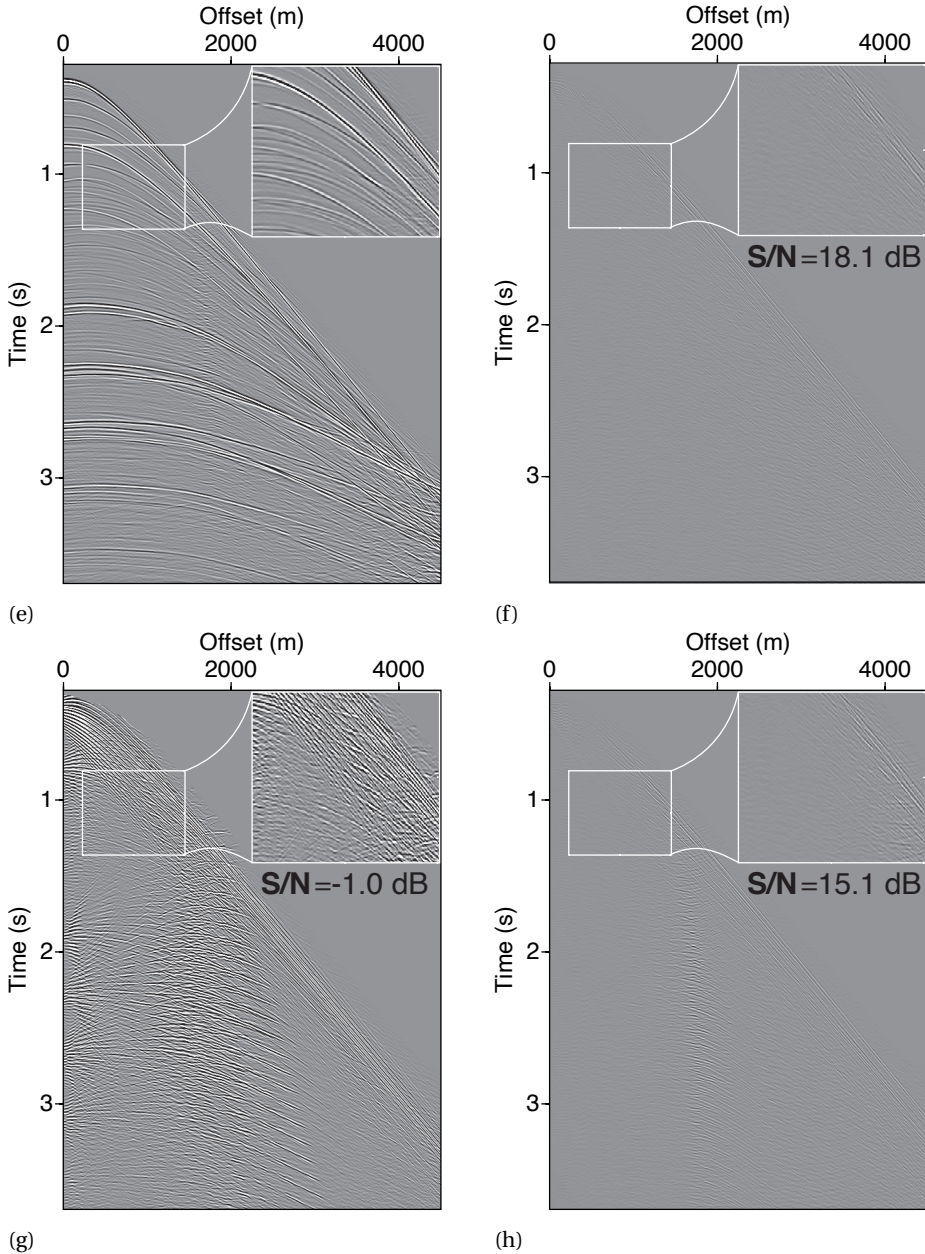
(a)

(b)

(c)

(d)

Figure 3.4: Results for the synthetic shot with a 10-80 m slanted cable (a) Input shot with the ghost. (b) Modeled upgoing wavefield. c) Shot after deterministic deghosting with actual ghost model. (d) Shot after deterministic deghosting with inaccurate ghost model. (e) Shot after adaptive deghosting. f) difference between b and c. g) difference between b and d. h) difference between b and e.
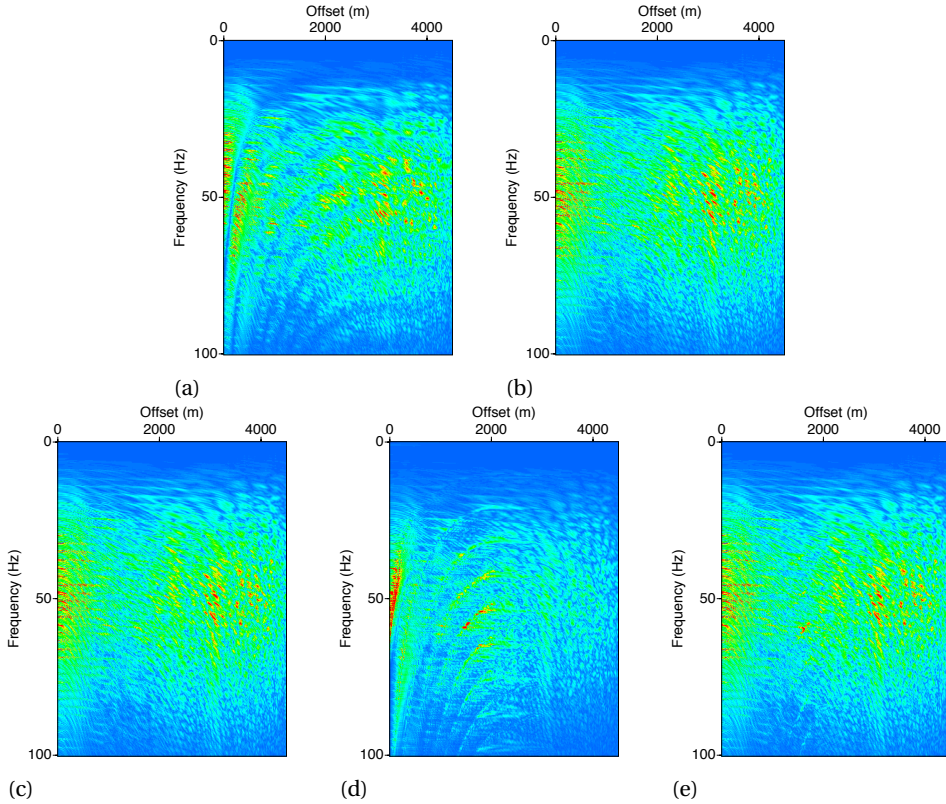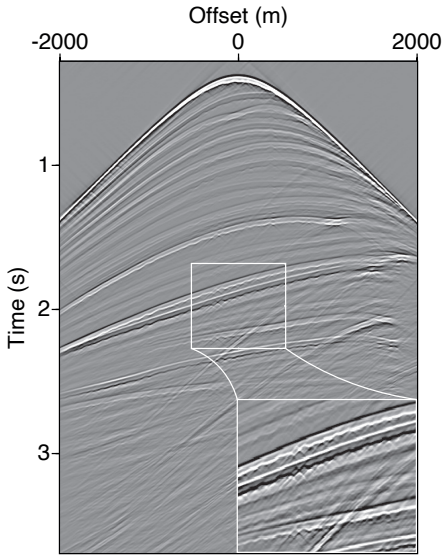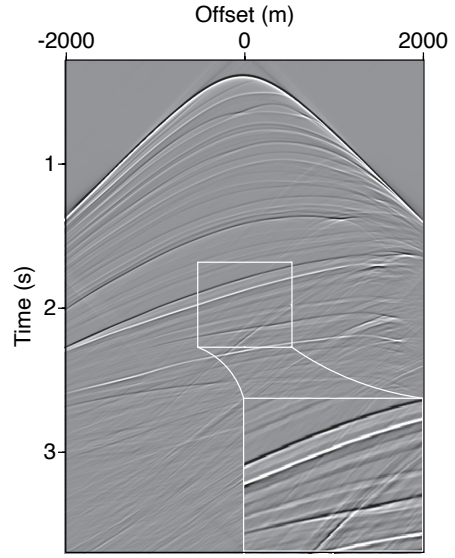
Figure 3.5: Results for the synthetic shot with a 10-80 m slanted cable in the frequency domain (a) Input shot with the ghost. (b) Modeled upgoing wavefield. c) Shot after deterministic deghosting with actual ghost model. (d) Shot after deterministic deghosting with inaccurate ghost model. (e) Shot after adaptive deghosting with inaccurate ghost model.

In the second example, we model 2D data including a dynamic sea surface. A finite-difference scheme uses the velocity model from Figure 3.2 to generate a shot record (containing primaries and internal multiples) with receivers located at a fixed, 30 m depth, and a spatial interval of 7.5 m. We model the dynamic sea surface according to Pierson and Moskowitz (1964) on a 3 m grid with a significant wave height of 4.5 m and maximum wave height of 8 m. We include the effect of the dynamic sea surface on the 2D receiver ghost by composing the results from tens of different ghost operators representing the dynamic sea surface (Blacquière and Sertlek, 2018). An alternative approach would be to include the dynamic sea surface in the finite-difference scheme (Konuk and Shragge, 2018). The source-ghost effect is not included in the modeling. In Figure 3.6a we show the shot record that contains the dynamic ghost effect. The magnified inlays in Figure 3.6 are amplified by a factor of two for display purposes. The imprint of the dynamic sea surface is clearly visible on the downgoing ghost wavefield as small time variations. These are absent on the primary upgoing wavefield that has never interacted with the sea surface.
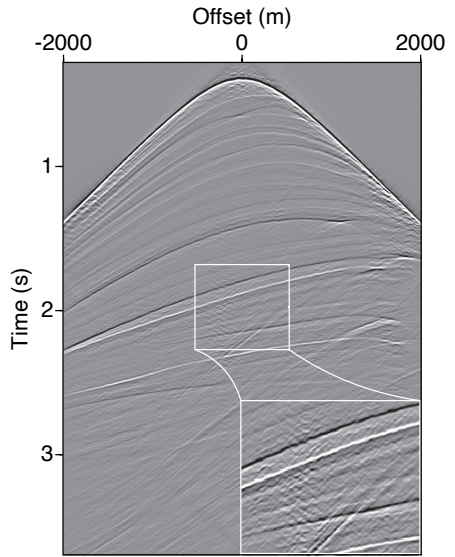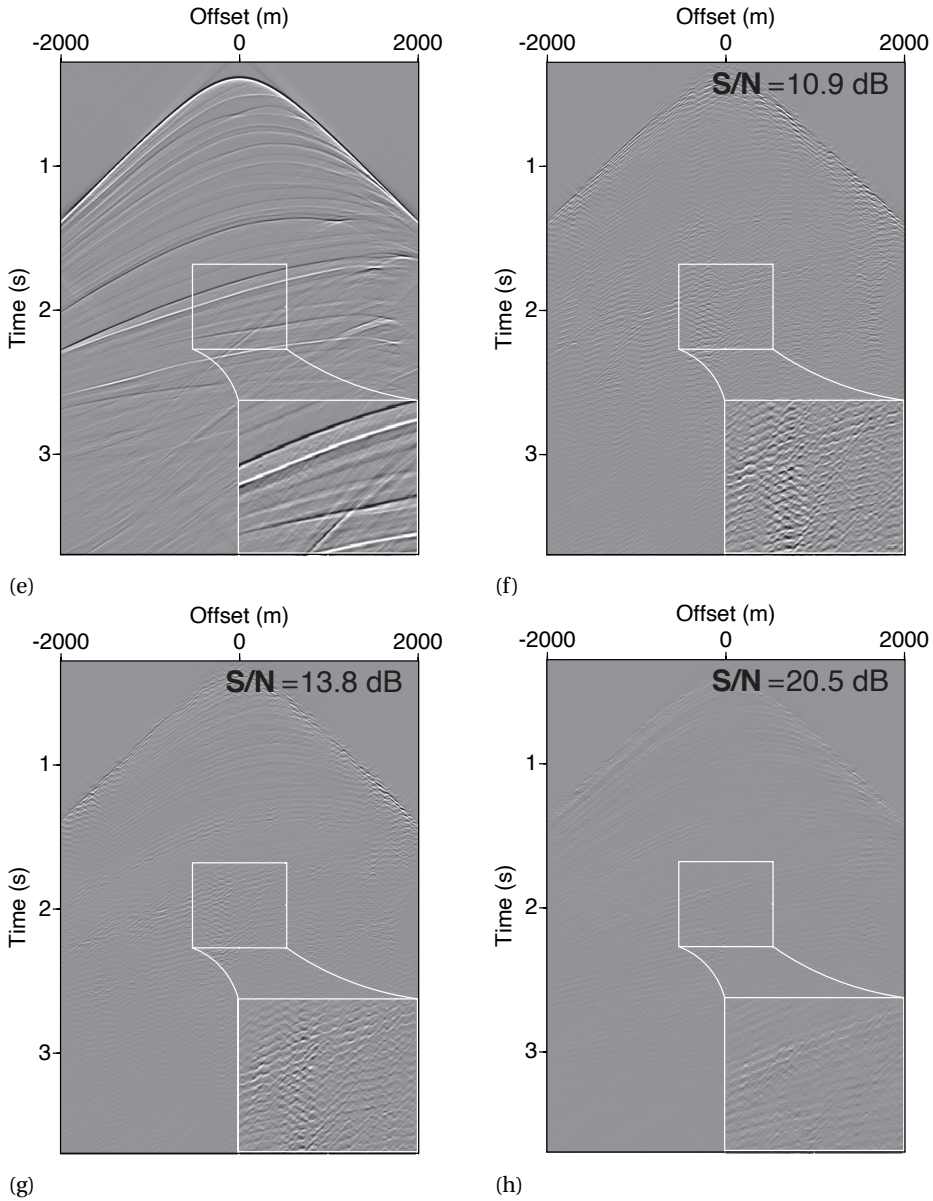
(a)

(b)
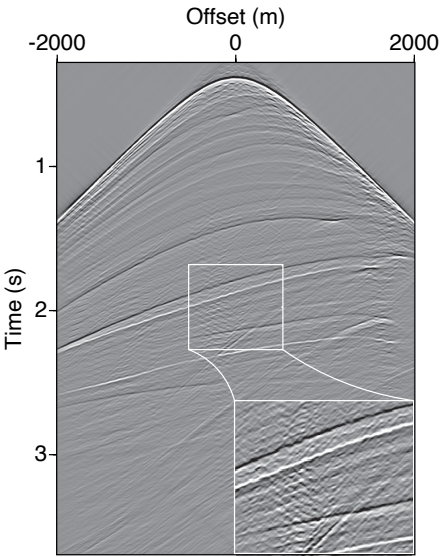
(c)

(d)

Figure 3.6: Results for the synthetic shot with dynamic sea surface and receivers at 30 m (a) Input shot with the ghost. (b) Modeled upgoing wavefield. c) Shot after deterministic deghosting with inaccurate ghost model. (d) Shot after single time-window adaptive deghosting. (e) Shot after multi time-window, adaptive deghosting. f) difference between b and c. g) difference between b and d. h) difference between b and e.
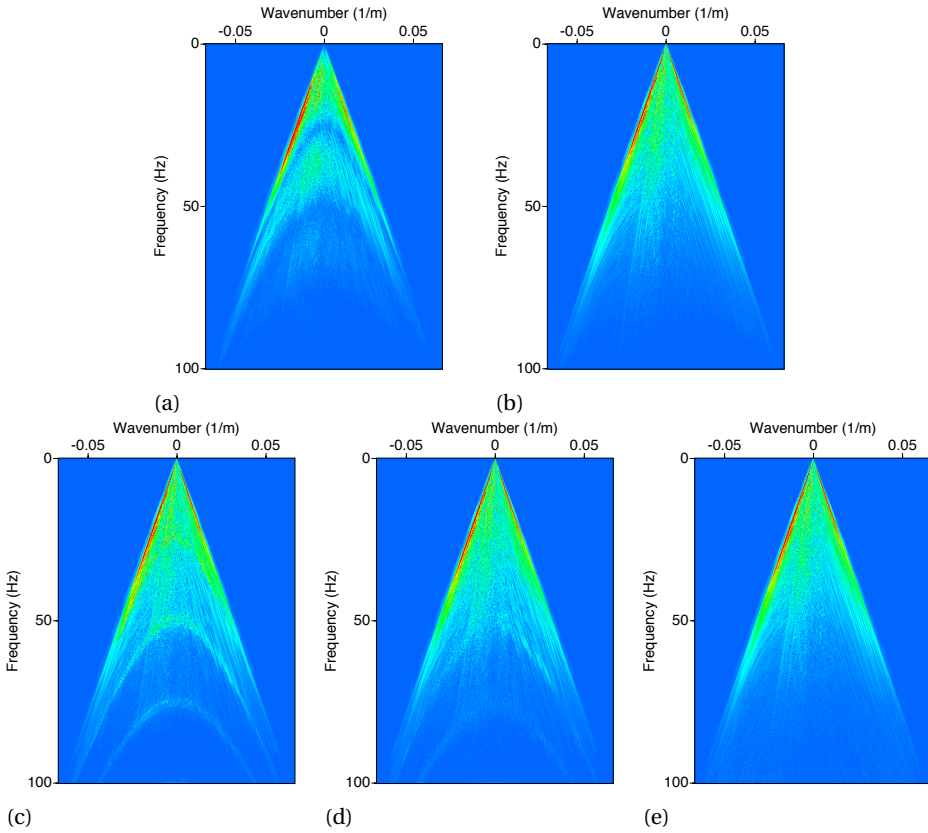
Figure 3.7: Results for the synthetic shot with dynamic sea surface and receivers at 30 m in the wavenumber-frequency domain. (a) Input shot with the ghost. (b) Modeled upgoing wavefield. c) Shot after deterministic deghosting with inaccurate ghost model. (d) Shot after single time-window adaptive deghosting. (e) Shot after multi time-window, adaptive deghosting.

There are notches visible in the wavenumber-frequency domain that correspond to the depth of the receivers with respect to the dynamic sea surface (Figure 3.7a). Figure 3.6c contains the result of deterministic deghosting assuming a flat sea surface. We show the difference with the modeled upgoing wavefield (Figure 3.6b) in Figure 3.6f. The ringing artifacts, visible in the magnified inlay, indicate that single-time-window, deterministic deghosting is not accurate. The corresponding S/N is equal to 10.9 dB. In the wavenumber-frequency domain, these artifacts show up as over-amplified amplitudes in the notch areas. Figures 3.6d and 3.6g show that we can reduce these events using single-time-window adaptive deghosting, which results in a S/N of 13.8 dB. However, the result in the space-time domain (Figure 3.6d), the difference with the modeled upgoing wavefield (Figure 3.6g) and the representation in the wavenumber-frequency domain indicate that the deghosting result is still not optimal. Figures 3.6e, 3.6h, and 3.7e show that multi time-window adaptive deghosting results in a significant further uplift. The ringing artifacts are considerably reduced, the notches in the wavenumber-frequency

domain are filled without over-amplification and the S/N is equal to 20.5 dB. Based on the maximum wave height of 8 m, a window size of approximately 0.4 s is sufficient to handle the dynamic effect. The parameter λ that controls the sparsity term was set to 0.01. Increasing λ better suppresses the ringing artifacts, but at the same time, it leads to more distortion in the upgoing wavefield.

3.6. Field data example

We apply our deterministic and adaptive deghosting method to a field data set from the Mediterranean Sea. Autonomous surface vessels control the depth of a midwater, quasi-stationary cable, and keep it at approximately 102 m. A small air-gun array of 150 in^3 is deployed at a depth of 7 m. The spatial sampling of the sources as well as the receivers is 25 m. The temporal sampling is 2 ms. The data set contains pressure and 3C particle velocity recordings. In this study, we only use the pressure data for deghosting. A more detailed description of the acquisition setup is given by Haumonte et al. (2016). A sparsity-promoting algorithm (Verschuur et al., 2012) removes noise from the data in local Radon domains. Figure 3.8a shows the shot record consisting of 60 receivers in the space-time domain. This record is used as input for deghosting. Because of the line geometry, 2D processing was applied. Figures 3.9a and 3.10a show, respectively, a magnified part of the shot record and the space frequency domain representation of Figure 3.8a. The notch diversity is a result of the varying depth with respect to the sea surface, indicated by the arrows in Figure 3.10a. We apply deterministic deghosting (see Figures 3.8b, 3.9b, and 3.10b) to the shot record assuming a flat sea surface and receivers at a fixed depth of 102 m to illustrate the effect of an incorrect ghost model. The ghost event is not well removed from the data and "ringing" artifacts occur, indicated by the arrows in Figures 3.8b and 3.9b. The notch area is overamplified in parts of the frequency domain, indicated by the arrows in Figure 3.10b. The residual ghost energy and overamplified notches indicate that a ghost model based on a flat sea surface and a fixed cable depth is not sufficiently accurate for this data set. Based on the information from the ship's logbook, the sea surface had a wave height between 0.1 and 0.5 m during data acquisition. We use a window size of 1.4 s related to a wave height of 0.5 m, a maximum frequency of 200 Hz, and a propagation velocity of 1500 m/s (see equation 3.21). The multi time-window adaptive deghosting method removes the ghost wavefield (see Figures 3.8c and 3.9b) and correctly fills the notch area in the frequency domain, indicated by the arrows in Figures 3.8c, 3.9c, and 3.10c. Figure 3.11 shows the optimum ghost model parameter δ for each time window. Parameter λ which controls the sparsity term, is set to 0.04 for each window. The S/N of the multi time-window adaptive deghosting result is 6.5 dB better than that of the deterministic deghosting result. Figures 3.8d, 3.9d, and 3.10d show that this difference is related to ringing and overamplification of the notch area.

To obtain the upgoing wavefield, Haumonte et al. (2016) sum a scaled version of the vertical particle-velocity data to the hydrophone data. This is called PZ-summation. In Figure 3.12, we compare the upgoing wavefield from PZ-summation with the deghosted data from multi time-window adaptive deghosting for, respectively, the full bandwidth, frequencies larger than 30 Hz (Figure 3.12c and 3.12d), and the frequency band ranging from 55 to 73 Hz (Figures 3.12e and 3.12f). Figure 3.12a shows that after PZ-summation,
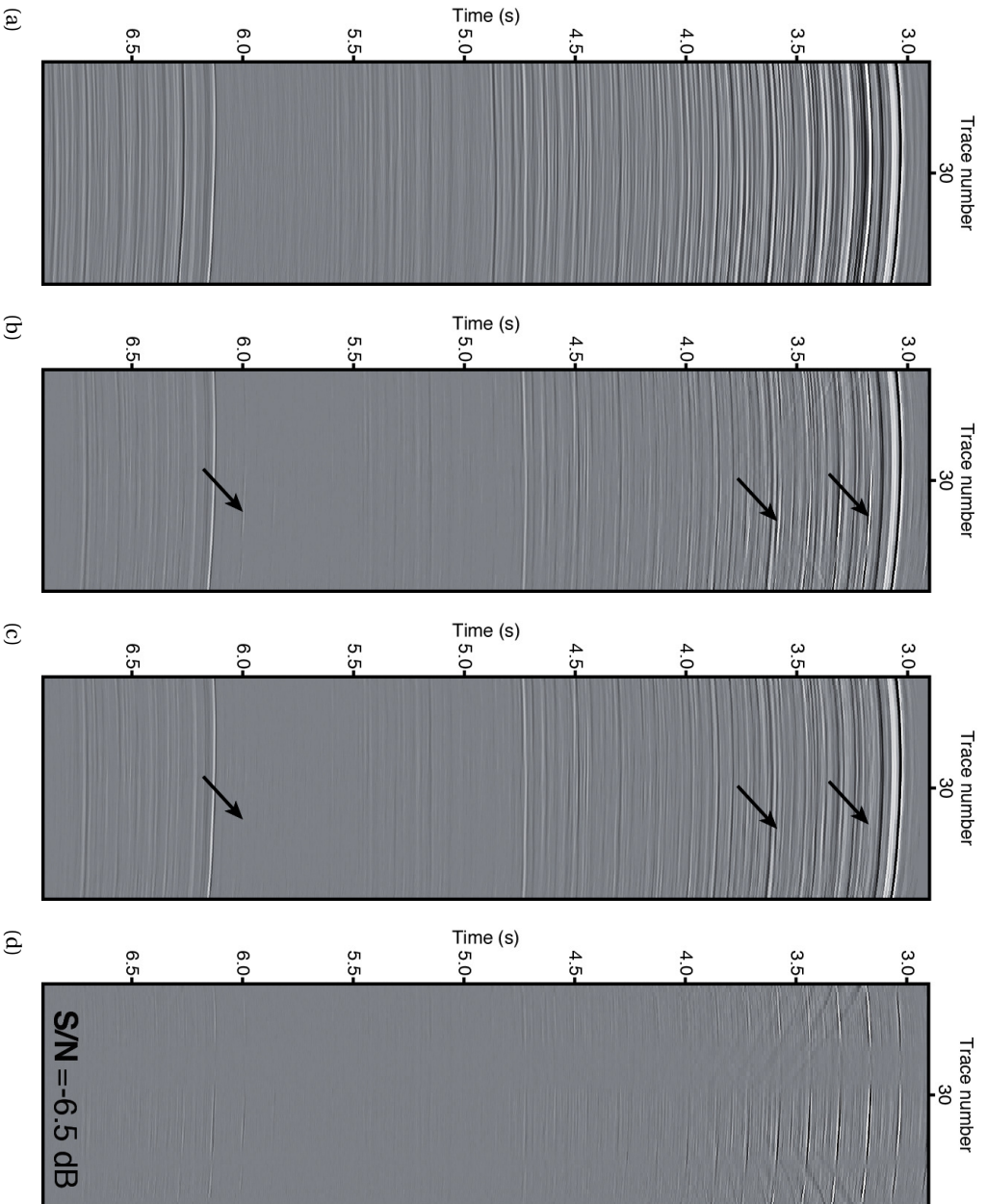
Figure 3.8: Results for a shot record with a smooth sea surface and receivers at a depth of approximately 102 m. a) Input shot with the ghost. b) Shot records after deterministic deghosting assuming a flat sea surface and receiver depth of 102 m. c) Shot records after multi time-window, adaptive deghosting. d) difference between b and c
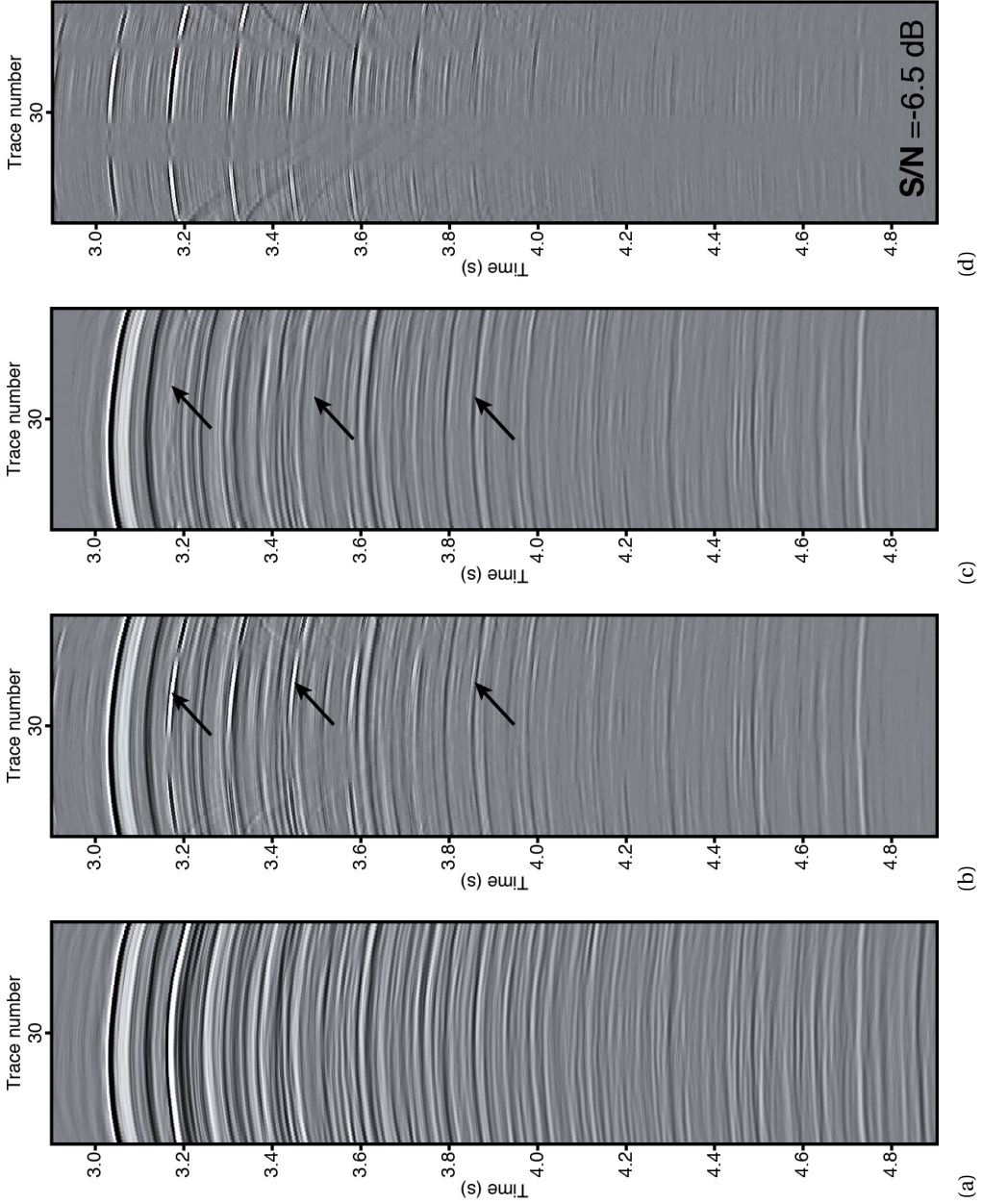
Figure 3.9: Magnified pictures from Figure 3.8. a) Input shot with the ghost. b) Shot records after deterministic deghosting assuming a flat sea surface and receiver depth of 102 m. c) Shot records after multi time-window, adaptive deghosting. d) Difference between b and c
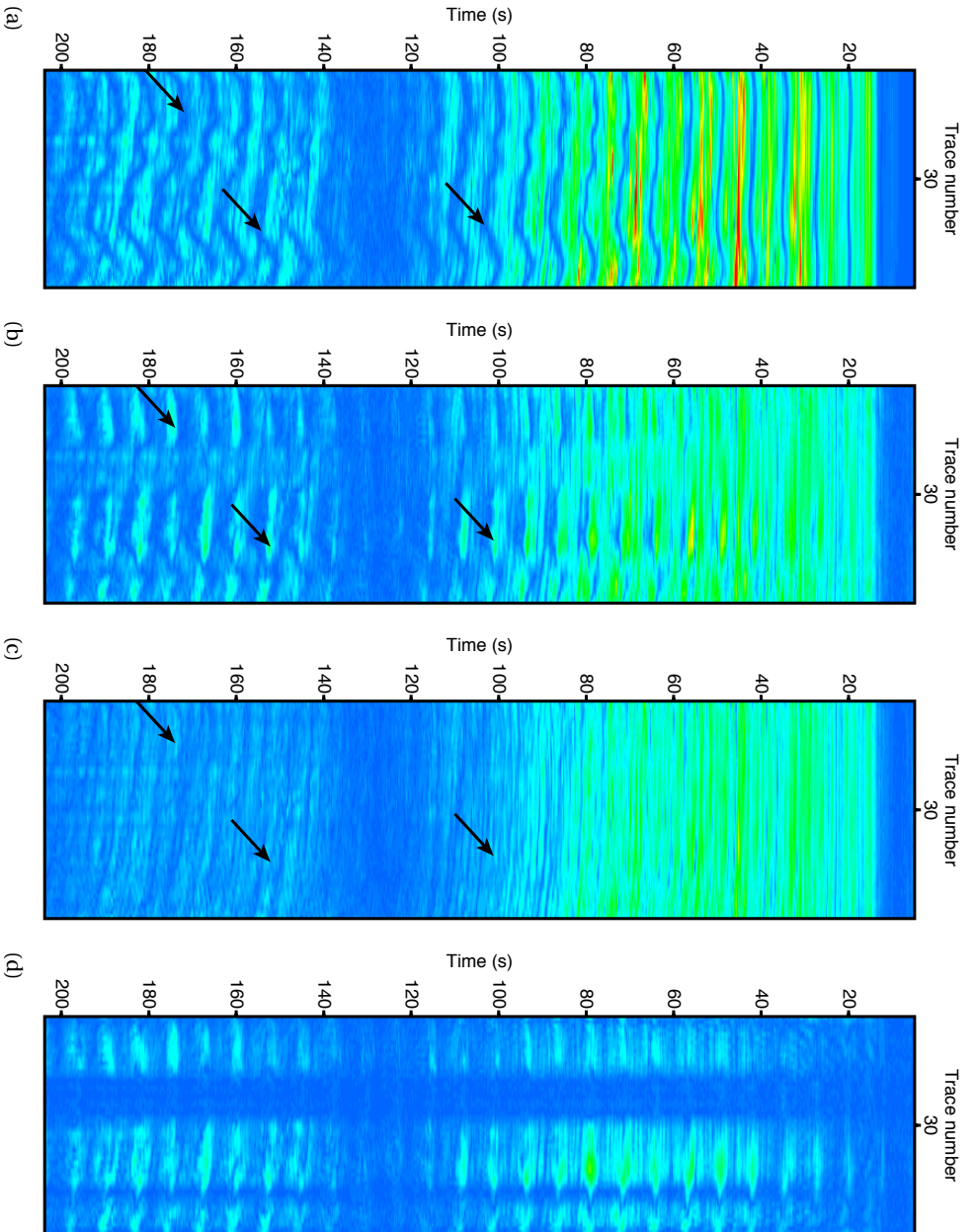
Figure 3.10: The frequency spectra corresponding to Figure 3.8. a) Input shot with the ghost. b) Shot records after deterministic deghosting. c) Shot records after multi time-window, adaptive deghosting. d) Difference between b and c
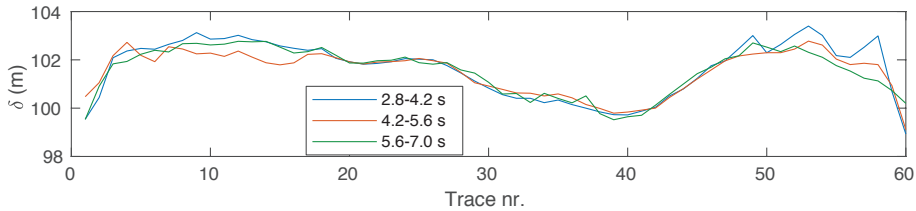
Figure 3.11: The estimated ghost parameter $\hat{\delta}$ for each time window.

the low-frequency noise of the verticle particle-velocity data overshadows the upgoing wavefield. For the frequencies above 30 Hz, the events after adaptive deghosting in Figure 3.12d well resemble the events of the upgoing wavefield after PZ-summation in Figure 3.12c (see the yellow arrows). There are some small discrepancies, though, between Figures 3.12c and 3.12d, indicated by the red arrows. In the notch areas in the range from 55 to 73 Hz (Figures 3.12c and 3.12d), both results are almost identical (see the yellow arrows in Figures 3.12d and 3.12e). The differences could originate from the PZ-summation method as well as from the multi time-window, adaptive deghosting method. The result of PZ-summation depends on a perfect calibration of the vertical particle-velocity data in relation to the hydrophone data. The multi time-window adaptive deghosting method was most likely limited by the use of 2D wavefield propagation operators and fixed water velocity. The use of 3D wavefield propagation operators would improve the adaptive deghosting method; however, the coarse sampling, especially in the crossline direction in a conventional marine seismic acquisition, limits the applicability of 3D wavefield propagation operators. The results of multi time-window adaptive deghosting indicate that the ghost energy was removed and the amplitudes in the notches were filled in correctly. Furthermore, the results well resemble the PZ-summation results for the higher frequencies.

3.7. Discussion

Most of the ghost energy was removed from the field data with our 2D method. The adaptiveness of the method makes an effort to correct for 3D effects as well. However, it is expected that an extension of the method to 3D would lead to a further improvement. Even more improvement is expected by integrating the results of multi time-window adaptive deghosting with results obtained by processing particle-velocity data, which are recorded by the accelerometers of the 4C cable. The particle-velocity data contain information related to the notch frequencies of the hydrophone data and vice versa. Although the accelerometers provide data with a high noise level, especially in the low-frequency band, a hybrid method that combines pressure-only and multi-component techniques (Caprioli et al., 2012; Poole and Cooper, 2018; Sanchis and Elboth, 2014) is expected to give a further uplift to the field-data deghosting results.

The speed of sound in the water may not be constant as it is a function of pressure, temperature and salinity (Leroy et al., 2008). These quantities may temporally and spa-

3

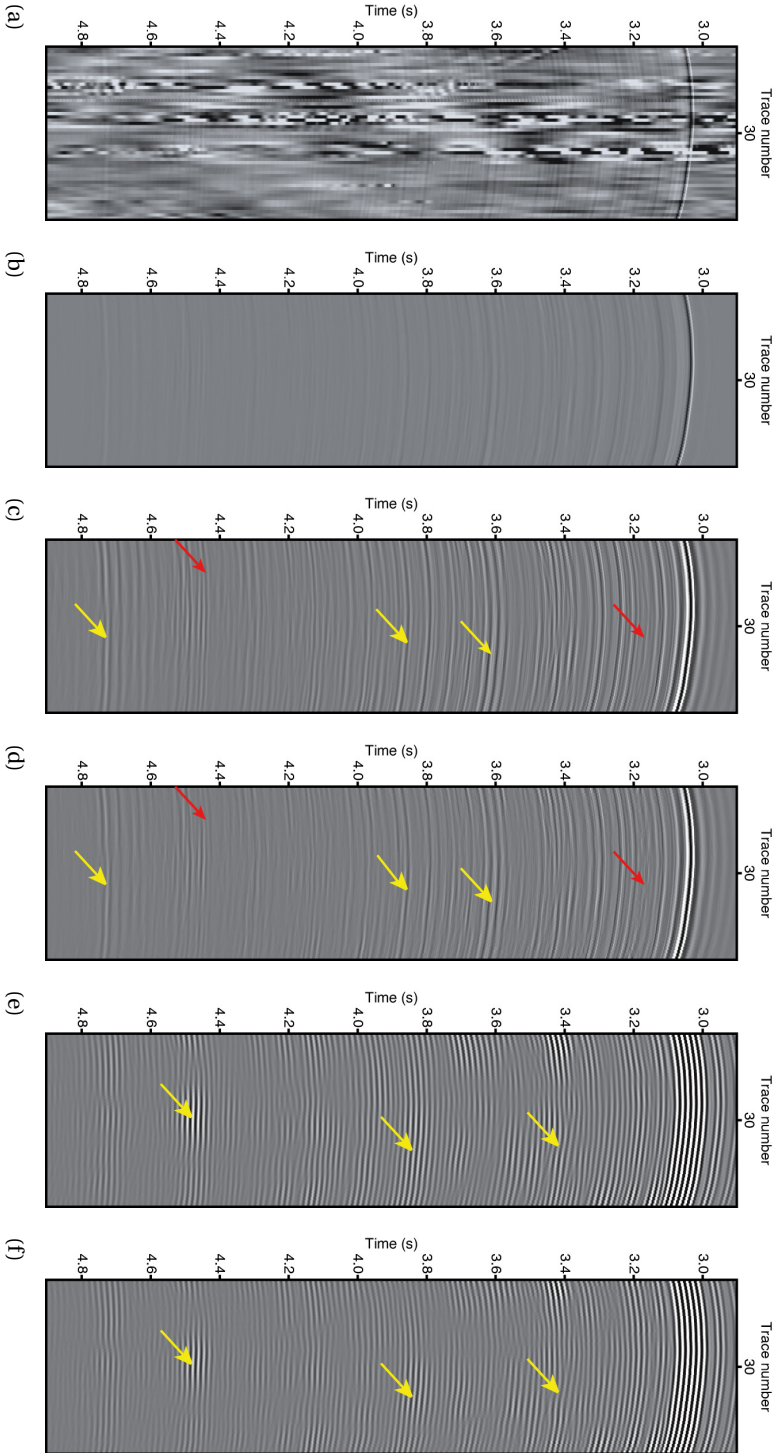Figure 3.12: Comparison of upgoing wavefield after PZ-summation and multi time-window, adaptive deghosting for a single shot record. a) Upgoing wavefield after PZ-summation (full bandwith). b) Deghosted shot record (full bandwith). c) Upgoing wavefield after PZ-summation (30 − 200 Hz). d) Deghosted data (30 − 200 Hz). e) Upgoing wavefield after PZ-summation (55 − 73 Hz). f) Deghosted data (55 − 73 Hz).

tially vary, thereby influencing the wave propagation. The adaptiveness of the deghosting algorithm will account for these effects to some extent. If there is prior knowledge about the water velocity we can include it in the wave propagation operators. Alternatively, the estimation of the speed of sound in water can be included in the deghosting method similar to the varying receiver depth with respect to the dynamic sea surface.

The deterministic and adaptive methods have been developed for receiver-side deghosting in the common-shot domain. Based on symmetry arguments, one would expect that they could also be applied for source-side deghosting in the common-receiver domain. However, the situation is not fully symmetric. This is because each shot has a different activation time, which means that the sea surface differs from shot to shot. In that case, a common receiver gather can no longer be considered to be the result of a single physical experiment. As a consequence, the source-side ghost wavefield in the common-receiver domain will contain trace-to-trace jitter (Blacquière and Sertlek, 2018). When used for source-side deghosting in the common-receiver domain, the method is taking the physics into account properly in the case of a flat sea surface only. Unfortunately, in many cases, source-side deghosting in the common-receiver domain would be impossible with our method due to coarsely sampled sources. The alternative would be to carry out source-side deghosting in shot records. However, when observed in the common-shot domain, the source-ghost wavefield has travelled through the Earth with all its complexity, which affects the angle-dependent ghost wavefield (Blacquière and Sertlek, 2018). Only in the case of a horizontally layered Earth, the proposed multi time-window, adaptive method is exact for source deghosting in shot records. Further research is needed to extend the method to source deghosting, taking into account these complications.

The sea surface generates the ghost wavefields as well as the surface-related multiples. Surface multiples contain one or more imprints of the dynamic sea surface, depending on their order. The source and receiver ghost imprints of the sea surface come on top of this. The task of a deghosting algorithm is to remove the source and/or receiver ghost. This means that after successful deghosting, the surface-related multiples (should) still contain one or more imprints of the dynamic sea surface. It is the task of a multiple-elimination algorithm to handle these imprints. This is not easy, since different orders of multiples may arrive at (almost) the same time, e.g., a first-order multiple with one surface imprint may arrive simultaneously with a second-order surface multiple with two, different, surface imprints. As a consequence, an approach that uses multiple time windows to handle the dynamics, similar to the one we developed for deghosting, would not be suitable for multiple elimination. Many multiple-elimination algorithms involve an adaptive subtraction of the estimated surface multiples from the data, which deals with the dynamic surface imprint on the multiples to some extent (e.g. Abma et al., 2005; Guitton and Verschuur, 2004; Verschuur et al., 1992). Further research is required to improve the multiple estimation process in the presence of a dynamic sea surface, and possibly in a process that combines deghosting and multiple elimination (Cecconello et al., 2019; Vrolijk et al., 2017).

3.8. CONCLUSIONS

We demonstrated that small errors in the ghost model have a negative effect on the results of deterministic deghosting. It is shown for synthetic data recorded on a variable depth that the proposed single time-window adaptive deghosting method gives a significant uplift and is able to correct small depth errors. In addition, it is possible to account for the dynamic sea surface using a multi time-window, adaptive approach. The deghosting results from field data recorded with a midwater, quasi-stationary cable demonstrate that the multi time-window, adaptive deghosting method is able to deal with the uncertainties that are present in the initial ghost model in the case of a realistic scenario.

4

SOURCE DEGHOSTING OF COARSELY-SAMPLED COMMON-RECEIVER DATA

It is well known that source deghosting can best be applied to common-receiver gathers, while receiver deghosting can best be applied to common-shot records. The source-ghost wavefield observed in the common-shot domain contains the imprint of the subsurface, which complicates source deghosting in common-shot domain, in particular when the subsurface is complex. Unfortunately, the alternative, i.e., the common-receiver domain, is often coarsely sampled, which complicates source deghosting in this domain as well. To solve the latter issue, we propose to train a convolutional neural network to apply source deghosting in this domain. We subsample all shot records with and without the receiver ghost wavefield to obtain the training data. Due to reciprocity this training data is a representative data set for source deghosting in the coarse common-receiver domain. We validate the machine-learning approach on simulated data and on field data. The machine learning approach gives a significant uplift to the simulated data compared to conventional source deghosting. The field-data results confirm that the proposed machine-learning approach is able to remove the source-ghost wavefield from the coarsely-sampled common-receiver gathers.

4.1. Introduction

In marine seismic acquisition sources are towed under the sea surface. Due to the large impedance contrast between water and air, the sea surface reflection coefficient is very close to -1 (more precise -0.99956). Therefore, at the sea surface the upgoing part of the source wavefield becomes a downgoing wavefield, the so-called source-ghost wavefield. The same mechanism is responsible for the receiver-ghost wavefield which is the sea surface reflection of the total upgoing wavefield. The source- and receiver-ghost wavefields cause notches in the wavenumber-frequency domain. The presence of these notches in the spectrum, due to destructive interference, limits the usable bandwidth and interpretability of marine seismic data. This is the main reason why it is desired to remove the source- as well as the receiver-ghost wavefield. These processes are called source and receiver deghosting. Note that multi-level and multi-component acquisition systems (Day et al., 2013; Tenghamn et al., 2007b) measure additional information to fill in the notches due to the receiver-ghost wavefield. To fill in notches due to the source-ghost wavefield, multi-level sources have been proposed as well (Caporal et al., 2018; Hopperstad et al., 2008; Parkes and Hegna, 2011).

In this Chapter we focus on conventional pressure-only data acquired with a streamer and with an airgun array acting as a single source. In this case most receiver deghosting methods require common-shot records that are densely sampled in the inline direction. A full-3D wavefield receiver deghosting method requires densely sampled receivers in both the inline and crossline direction. It is quite common that there are acquisition gaps at the source side as well as at the receiver side in marine seismic acquisition due to economic reasons, obstructions such as islands and oil rigs, unfavourable topography and environmental regulations. In practise, the acquisition gaps at the source side are often larger than at the receiver side. Large gaps in the source acquisition limit the applicability of source deghosting methods, that are best suited for densely sampled common-receiver data.

There are methodologies such as carpet shooting (Walker et al., 2014) that provide dense source sampling, but in this Chapter, we focus on the effects and the implications of coarse source sampling on source deghosting. At the receiver side multi-component data can assist to overcome the sampling requirement by integrating receiver interpolation with up-down decomposition (Tang and Campman, 2017). Sun and Verschuur (2017) proposed a method for pressure data at the detector side that implicitly handles sparse data. Interpolation of seismic sources with large acquisition gaps is not straightforward, especially if the subsurface is complex. Non-linear effects complicate source deghosting as well. Parkes and Hatton (1986) described the so-called 'shot effect' that resulted in such non-linear behaviour. Ghost cavitation is another non-linear effect that can occur near the water-air interface (Khodabandeloo and Landrø, 2018; Landrø et al., 2011). Near-field hydrophone measurements can be used to derive a far-field signature that includes the ghost effect with its non-linearities, which can be used to estimate the source-deghosted data (Hampson, 2017; Kryvohuz and Campman, 2017; Telling and Grion, 2019; Ziolkowski et al., 1982). Source deghosting is often carried out in the common-shot domain to satisfy the sampling requirements. However, when ob-

served in the common-shot domain, the source-ghost wavefield has travelled through the Earth with all its complexity, which causes the removal of the source-ghost wavefield in this domain to be far from straightforward (Blacquière and Sertlek, 2018).

We propose a machine learning approach to remove the source-ghost wavefield in the coarsely sampled common-receiver domain. The architecture of the network that we use in this Chapter is based on recently developed convolutional neural networks (CNN) in deep learning for medical image recognition (Quan et al., 2016; Ronneberger et al., 2015). These networks are applicable in the case of a limited amount of training data and are known to be effective for data that resemble the training data. Neural networks were introduced in geophysics quite some time ago, e.g. in seismic inversion (Nath et al., 1999; Röth and Tarantola, 1994) and interpretation (Glinsky et al., 2001). In more recent years, the development of powerful graphic processing units (GPUs) has led to numerous deep learning algorithms in seismic processing (Mikhailiuk and Faul, 2018; Siahkoohi et al., 2019b; Sun and Demanet, 2018), interpretation (Huang et al., 2017; Pham et al., 2019; Ross and Cole, 2017; Shi et al., 2018) and inversion (Araya-Polo et al., 2018; Das et al., 2019; Lewis and Vigh, 2017).

In the first part of the Chapter we describe the theoretical framework of source deghosting carried out in the common-receiver domain and receiver deghosting carried out in the common-shot domain. Then, we show the limitation of source deghosting carried out in the coarsely sampled common-receiver domain. After that, we demonstrate the limitations of a source deghosting method carried out in a densely sampled common-shot domain.

In the second part of this Chapter we introduce a strategy to obtain a suitable CNN-training data set. We assume that receivers are densely sampled and sources are coarsely sampled. To ensure that the shot records resemble the receiver gathers we first need to redatum the receivers to the source level and replace the original receiver-ghost wavefield with a receiver-ghost wavefield that corresponds to that same level, i.e., the source level. After that we subsample the receivers to mimic the coarse sampling of the sources. Now, we have input training data that consist of coarsely sampled shot records including the source- and receiver-ghost wavefields. We also prepare output training data that consist of receiver-deghosted coarsely sampled shot records. After the training, we test the network for the purpose of source deghosting of coarsely sampled receiver gathers. In the first machine learning example, we train and apply the CNN to numerical data. This example shows that we are able to train a network and obtain a significant uplift of the source-deghosted data. In the second machine learning example, we test the method on a field data set, acquired offshore Australia.

4.2. Ghost Model

As mentioned, the reflectivity at the sea surface is very close to -1. Therefore, at the source level $z_s(x, y)$, the total downgoing wavefield is the combination of the direct source wavefield and its reflection at the sea surface. The latter is the so-called source-ghost wavefield. Similarly, at the receiver level $z_d(x, y)$ the combination of the direct upgoing

4

and reflected downgoing wavefield is measured. The latter is the so-called receiver-ghost wavefield. There are various methods to include the shape and dynamics of a rough sea surface (e.g. Grion and Telling, 2016; King and Poole, 2015; Vrolijk and Blacquière, 2020b). However, in this Chapter we neglect the shape and dynamics of the sea surface and assume that the sea surface is well represented by a horizontal sea surface z_0. We formulate a monochromatic seismic data set $\mathbf{P}$, including the receiver- and source-ghost wavefields, according to the matrix notation introduced by Berkhout (1985) as

$$\mathbf{P}(z_d; z_s) = \mathbf{D}(z_d)\mathbf{G}(z_d, z_d)\mathbf{X}(z_d, z_s)\mathbf{G}(z_s, z_s)\mathbf{S}(z_s), \tag{4.1}$$

where $\mathbf{S}$ describes the locations and spectral properties of the sources, $\mathbf{X}$ is the transfer function of the subsurface below the source and receiver level, $\mathbf{D}$ describes the locations and spectral properties of the receivers, and $\mathbf{G}$ is the source or the receiver ghost matrix. The source ghost matrix at the source side is given by:

$$\mathbf{G}(z_s, z_s) = \mathbf{I} - \mathbf{W}(z_s, z_0)\mathbf{W}(z_0, z_s), \tag{4.2}$$

where $\mathbf{W}(z_0, z_s)$ describes forward propagation from the source level up to the sea surface and $\mathbf{W}(z_s, z_0)$ describes forward propagation from the sea surface down to the source level, the minus sign represents the strong sea surface reflectivity of -1. The receiver ghost matrix is similar to the source ghost matrix, with propagation matrices corresponding to the receiver level z_d. In the case of a flat sea surface and a horizontal receiver level z_d or a horizontal source level z_s, we can replace the matrix multiplication in the space-frequency domain by a simple multiplication in the wavenumber-frequency domain with the ghost operator:

$$\tilde{G}(k_x; \omega) = 1 - e^{-2jk_z\Delta z}, \tag{4.3}$$

where k_z is the vertical component of the wave vector.

In the case of ideal spatial receiver sampling, i.e., sampling according to the Nyquist criterion and unit receivers, the detector matrix becomes a unity matrix, i.e., $\mathbf{D}(z_d) = \mathbf{I}$, and the right-hand side of equation 4.1 becomes the following matrix product:

$$\mathbf{G}(z_d, z_d)\mathbf{X}(z_d, z_s)\mathbf{G}(z_s, z_s)\mathbf{S}(z_s). \tag{4.4}$$

A shot record representation of matrix product 4.4 is given by column vector

$$\mathbf{G}(z_d, z_d)\mathbf{X}(z_d, z_s)\mathbf{G}(z_s, z_s)\vec{S}(z_s). \tag{4.5}$$

Applying the inverse of $\mathbf{G}(z_d, z_d)$ to expression 4.5 gives the receiver-deghosted shot record

$$\mathbf{X}(z_d, z_s)\mathbf{G}(z_s, z_s)\vec{S}(z_s). \tag{4.6}$$

In practise, it is not straightforward to obtain the source-deghosted shot record from expression 4.6. Because expression 4.6 must be multiplied from the left by the matrix product: $\mathbf{X}(z_d, z_s)[\mathbf{G}(z_s, z_s)]^{-1}[\mathbf{X}(z_d, z_s)]^{-1}$. For the special case of a laterally invariant subsurface the symmetric Toeplitz matrices $\mathbf{X}$ and $\mathbf{G}$ commute, i.e.,$\mathbf{X}(z_d, z_s)\mathbf{G}(z_s, z_s)\vec{S}(z_s) = \mathbf{G}(z_s, z_s)\mathbf{X}(z_d, z_s)\vec{S}(z_s)$, which simplifies shot record source deghosting. We will see this

later in an example given in Figure 4.2.

In the case of ideal spatial source sampling, with unit sources, meaning that $\mathbf{S}(z_s) = \mathbf{I}$, the right-hand side of equation 4.1 becomes:

$$\mathbf{D}(z_d)\mathbf{G}(z_d, z_d)\mathbf{X}(z_d, z_s)\mathbf{G}(z_s, z_s). \tag{4.7}$$

A receiver gather is represented by

$$\vec{D}^\dagger(z_d)\mathbf{G}(z_d, z_d)\mathbf{X}(z_d, z_s)\mathbf{G}(z_s, z_s), \tag{4.8}$$

where the dagger symbol † indicates a row vector. Now, applying the inverse of $\mathbf{G}(z_s, z_s)$ to expression 4.8 gives a source-deghosted receiver gather, which is given by

$$\vec{D}^\dagger(z_d)\mathbf{G}(z_d, z_d)\mathbf{X}(z_d, z_s). \tag{4.9}$$

Again, it is not straightforward to obtain the receiver-deghosted receiver gather from expression 4.9. We take the transposed of expression 4.9 to obtain

$$\mathbf{X}(z_d, z_s)^T\mathbf{G}(z_d, z_d)\vec{D}(z_d), \tag{4.10}$$

using $\mathbf{G}(z_d, z_d) = \mathbf{G}(z_d, z_d)^T$ because of reciprocity, where superscript T indicates the transposed of a matrix. Now, the similarity with expression 4.6 is evident.

Above, we have formulated source deghosting carried out in the common-receiver domain (expressions 4.5 and 4.6) and receiver deghosting carried out in the common-shot domain (expressions 4.8 and 4.9). In the following section, numerical examples demonstrate that for a laterally invariant subsurface, source deghosting carried out in the common-shot domain is similar to source deghosting carried out in the common-receiver domain. However, for a complex subsurface source deghosting carried out in the common-receiver domain is preferable to source deghosting carried out in the common-shot domain.

4.3. THE EFFECT OF A COMPLEX SUBSURFACE

We first generated ghost-free 2D seismic data with a finite-difference scheme using the laterally invariant velocity model from Figure 4.1a. After that, we only added the source ghost using equation 4.3. For now we did not model the receiver ghost, because we first put all emphasis on the source ghost. Sources as well as receivers were located at a depth of 15 m with a spatial sampling of 5 m. In Figures 4.2a and 4.2b we show, respectively, a receiver gather and a shot record. As expected, they are identical. In Figures 4.2c and 4.2d we show the corresponding representations in the wavenumber-frequency domain. The spectra have a clear first-order angle-dependent notch, which is at 50 Hz for vertical wavefield propagation. This frequency can be easily computed from the water velocity c and the source depth z_s, being 1500 m/s and 15 m, respectively via $f_{notch} = 0.5c/z_s$. The amplitude roll-off towards 0 Hz is the effect of the zeroth-order notch.
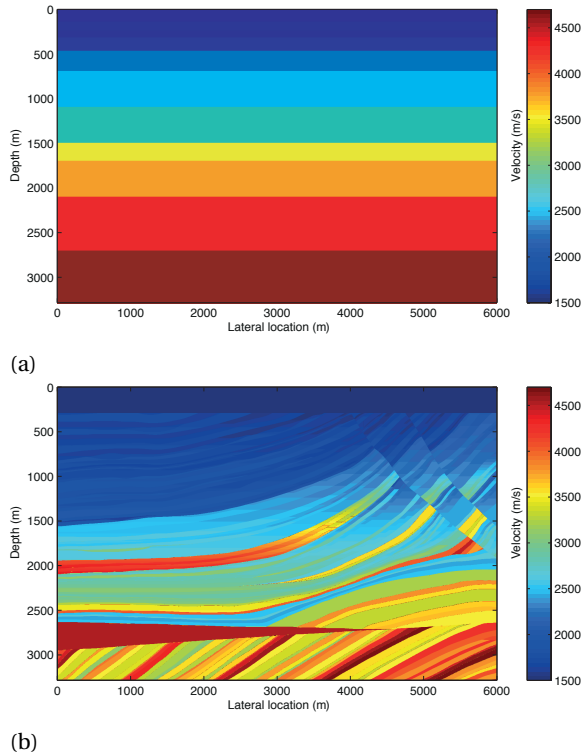
(a)

4

(b)

Figure 4.1: Velocity models used for acoustic finite-difference modeling. a) Velocity model of a laterally invariant subsurface. b) Velocity model of a complex subsurface (Marmousi model including water layer on top).

In the next example, we generated a similar data set, but now using the Marmousi subsurface model shown in Figure 4.1b rather than the laterally invariant subsurface model of Figure 4.1a. We show a receiver gather in Figure 4.3a and a shot record in Figure 4.3b. Unlike in the previous example, they are not identical. The difference in Figure 4.3c shows that the source-ghost wavefield, once observed in the common-shot domain, is affected by the complex subsurface. In the wavenumber-frequency domain the first-order notch is clearly visible in the common-receiver domain (see Figure 4.3d). However, Figures 4.3e and 4.3f show that the first-order notch is blurred in the wavenumber-frequency spectrum of the receiver gather.

In Chapter 3 we gave a detailed description of a deghosting algorithm based on sparse inversion as well as its adaptive variant. The latter was used to obtain our deghosting results. In Figure 4.4a we show the result of applying source deghosting to the receiver gather of 4.3a. The difference with the original ghost-free data (see Figure 4.4b) is quantified by the signal-to-noise ratio (S/N) as follows:

$$S/N = 10log\Big(\sum_x \sum_t \frac{|\vec{p}_0|^2}{|\vec{p}_0 - \langle \vec{p}_0 \rangle|^2}\Big), \tag{4.11}$$
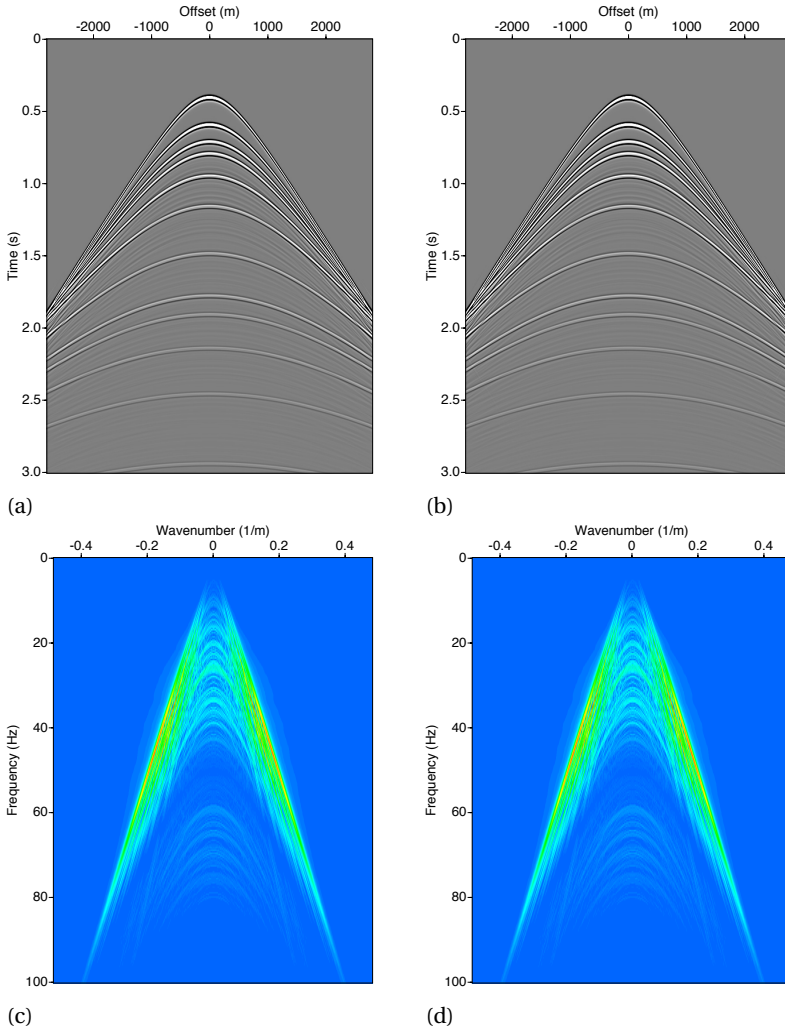
Figure 4.2: Data including the source-ghost wavefield in various domains for a laterally invariant model and a source depth of 15 m. a) A receiver gather including the source ghost. b) A shot record including the source ghost. d) The wavenumber-frequency spectrum of the receiver gather including the source ghost. e) The wavenumber-frequency spectrum of the shot record including the source ghost.

with $\vec{p}_0$ being the modeled ghost-free data and $\langle\vec{p}_0\rangle$ the deghosted result in the space time domain. The S/N in this example is equal to 39.8 dB. A selected area with a time range of 2.2 s to 2.6 s and an offset range of -2250 m to -1250 m has a S/N of 39.8 dB and another selected area with a time range of 1.52 s to 1.92 and offset range of 1000 m to 2000 m has a S/N of 41.0 dB. The deghosting algorithm promotes sparsity in the space-time domain, which stabilizes the inversion. Therefore, no obvious deghosting artifacts are present in the data domain (see Figures 4.4a and 4.4b) and notches in the

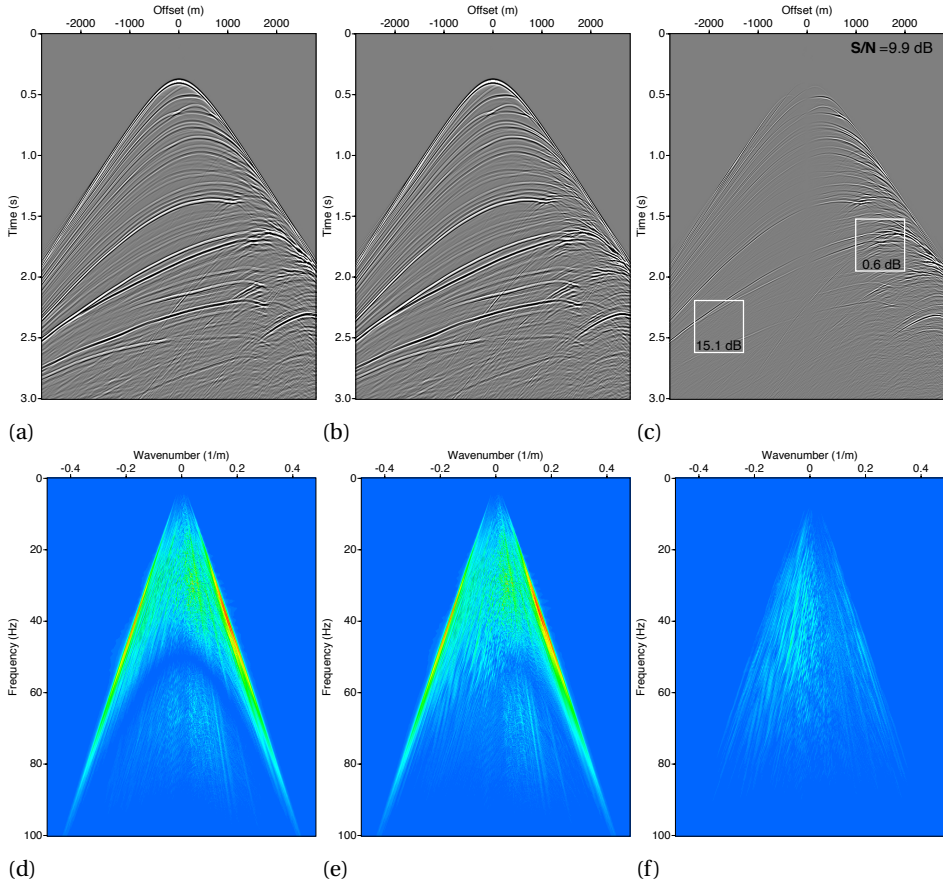(a)   (b)   (c)

(d)   (e)   (f)

Figure 4.3: Data including the source-ghost wavefield in various domains for the Marmousi model and a source depth of 15 m. a) A receiver gather including the source ghost. b) A shot record including the source ghost. c) Difference between Figures 4.3a and 4.3b. d) The wavenumber-frequency spectrum of the receiver gather including the source ghost. e) The wavenumber-frequency spectrum of the shot record including the source ghost. f) Difference between Figures 4.3d and 4.3e.

wavenumber-frequency domain are filled with the correct amplitudes (see Figures 4.4c and 4.4d).

We have demonstrated that the source-ghost wavefield, once observed in the common-shot domain, is affected by the complex subsurface. Consequently, this will have an effect on the quality of source deghosting in the common-shot domain, which we demonstrate in Figure 4.5. To obtain the result in Figure 4.5a we applied a different source deghosting algorithm, being adaptive, to the shot record of Figure 4.3b. This deghosting algorithm can adapt the depth of each source as a function of time. In this way, it can handle the source ghost observed in the common-shot domain, i.e., after being affected by the complex Earth, to some extent. The difference in Figure 4.5b shows that there are some weak ringing artefacts and amplitude losses. The corresponding wavenumber-
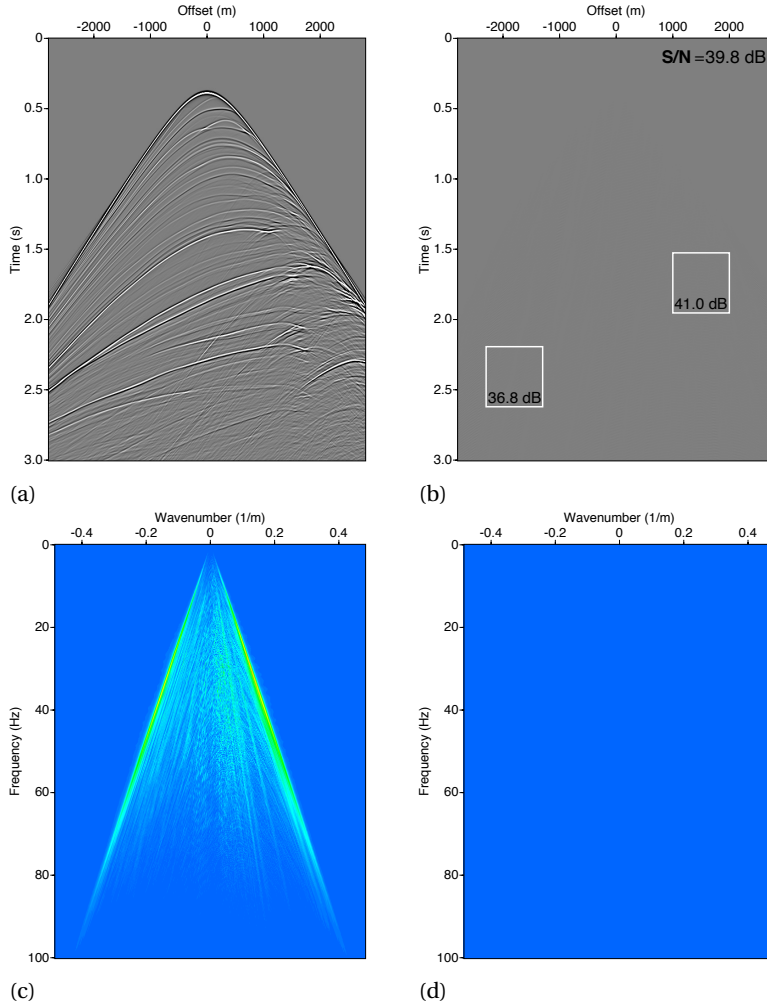
Figure 4.4: The source-deghosting result based on sparse inversion of the data shown in Figure 4.3a. a) Common-receiver gather after source deghosting. b) Difference between Figure 4.4a and modeled ghost-free receiver gather. c) The wavenumber-frequency spectrum of Figure 4.4a. d) The wavenumber-frequency spectrum of Figure 4.4b.

frequency spectra of Figures 4.5a and 4.5b are given in Figures 4.5c and 4.5d. The overall and selected signal-to-noise ratios in Figure 4.5b are equal to respectively, 9.0 dB, 0.6 dB and 15.1 dB. These numbers are significantly lower than the signal-to-noise ratios that we obtained in the common-receiver domain (Figure 4.3b). Hence, this example illustrates that it is essential that source deghosting is carried out in the common-receiver domain to obtain an optimal source deghosted result.
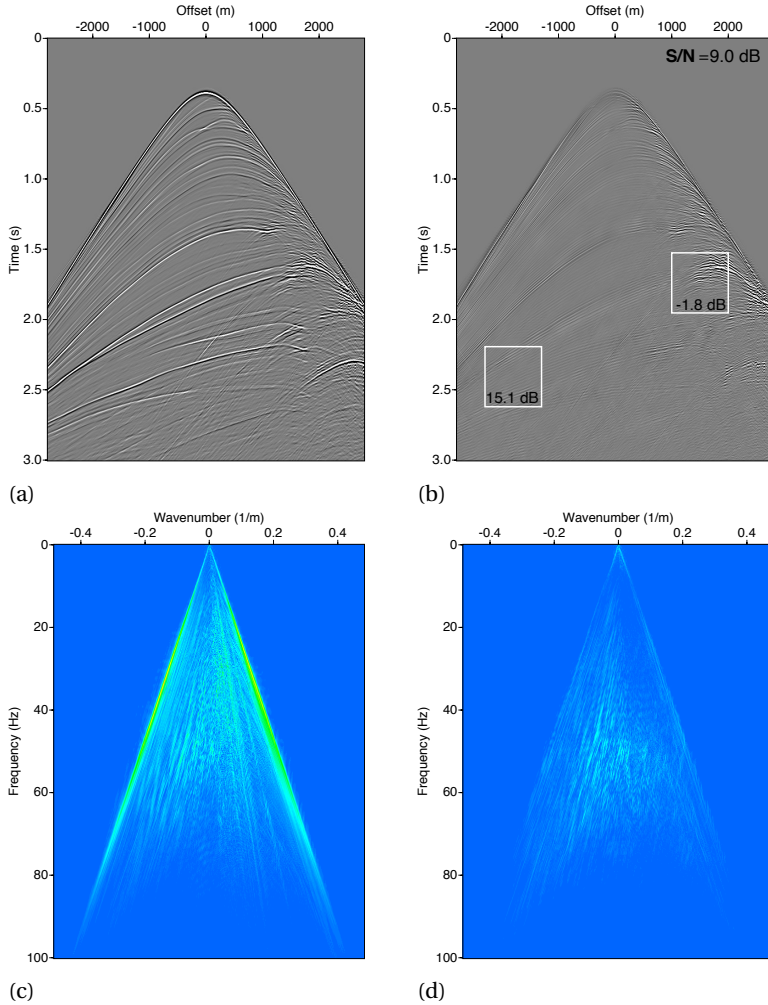
Figure 4.5: The adaptive source-deghosting result of Figure 4.3b. a) Shot record after source deghosting. b) Difference between Figure 4.5a and modeled ghost-free shot record. c) The wavenumber-frequency spectrum of Figure 4.5a. d) The wavenumber-frequency spectrum of Figure 4.5b

4.4. THE EFFECT OF COARSELY SAMPLED DATA

We have demonstrated that source deghosting should be carried out in the common-receiver domain in the case of a complex subsurface to obtain optimum results. However, in practise, this domain is often coarsely sampled. This complicates source deghosting as this would cause aliasing artifacts. In Figure 4.6a we show a coarsely sampled receiver gather from the Marmousi model with the large spatial source sampling of 75 m. In practise, such a coarse source sampling often occurs in the crossline direction. The result is that the data is aliased, which leads to the well-known wrap-around effects in the
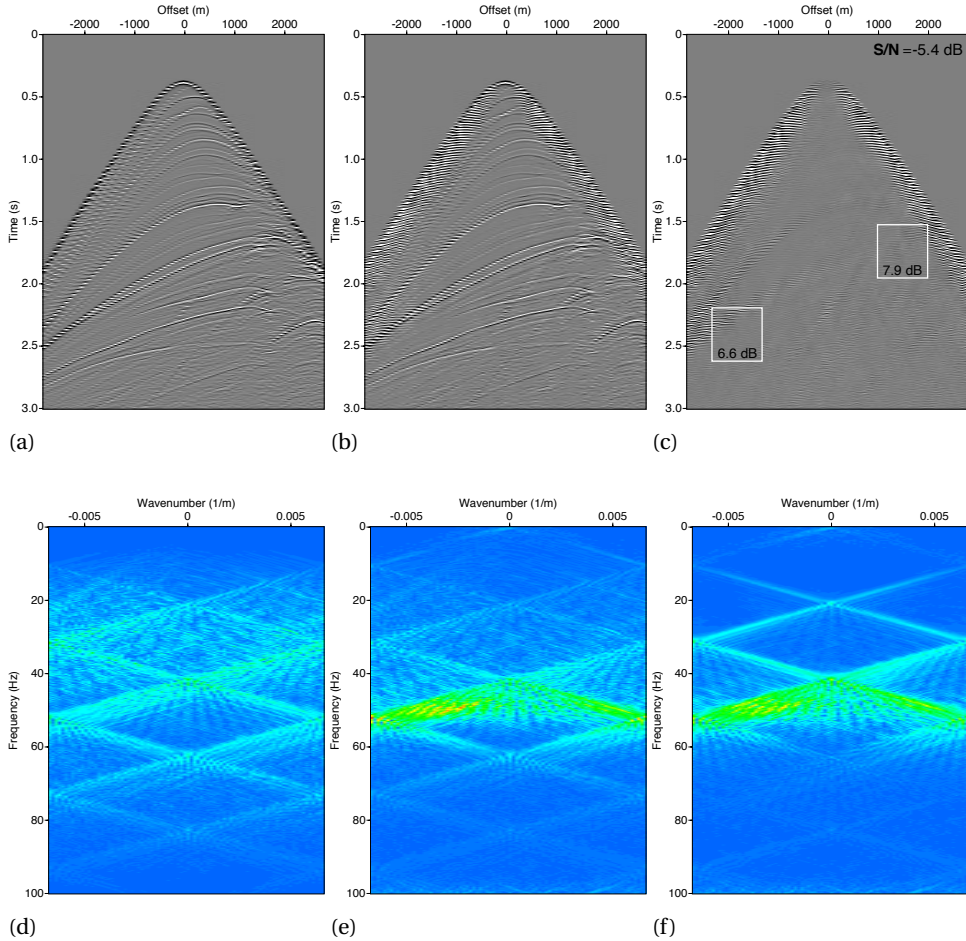
Figure 4.6: a). Modeled, coarsely sampled, ghost-free common-receiver gather. b) Common-receiver gather after deghosting. c) Difference between Figure 4.6a and Figure 4.6b. d) The wavenumber-frequency spectrum of Figure 4.6a. e) The wavenumber-frequency spectrum of Figure 4.6b. f) The wavenumber-frequency spectrum of Figure 4.6c.

wavenumber-frequency domain (see Figure 4.6c). Especially, the high frequencies are affected by the coarse sampling. Our sparse inversion deghosting method can handle coarsely sampled receiver gathers to some extent. The result is given in Figures 4.6b and 4.6e in, respectively, the space-time and wavenumber-frequency domain. In Figures 4.6c and 4.6f we show the difference with respect to the ghost-free data. The aliasing artifacts have a detrimental effect on the S/N, which is as low as -5.4 dB. Thus, in case of coarsely sampled sources we have to deal with the following dilemma. In the common-receiver domain the quality of source deghosting is limited by coarse source sampling, while in the common-shot domain the quality of source deghosting is limited by the complex

subsurface. In the following section we propose a machine learning approach to handle this dilemma.

4.5. CNN SOURCE DEGHOSTING OF COARSELY SAMPLED COMMON-RECEIVER DATA

We have demonstrated that a coarse sampling in the common-receiver domain causes artifacts in the results of source deghosting. To overcome this issue, we propose to train a Convolutional Neural Network (CNN) with supervised learning to apply source deghosting to coarsely sampled receiver gathers. We start with the seismic data given by the following matrix product:

$$\mathbf{D}_\delta(z_d)\mathbf{G}(z_d, z_d)\mathbf{X}(z_d, z_s)\mathbf{G}(z_s, z_s)\mathbf{S}_\Delta(z_s), \tag{4.12}$$

where the subscript Δ indicates a coarse sampling (here for the sources), with spatial interval Δx, while subscript δ indicates a dense sampling (here for the receivers), with spatial interval δx. The relation between the two is given by $\Delta x = n\delta x$, where n is an integer number.

The input training data consist of coarsely sampled shot records including the source-ghost wavefield as well as the receiver-ghost wavefield, whereas the output training data consist of receiver-deghosted coarsely sampled shot records. We apply the following processing steps to generate the training data. At first, we apply receiver deghosting to matrix product 4.12. After that, we redatum the receivers to the level of the sources (see Figures 4.7a and 4.7b) using wavefield propagation on the pressure data, such that it becomes

$$\mathbf{D}_\delta(z_s)\mathbf{X}(z_s, z_s)\mathbf{G}(z_s, z_s)\mathbf{S}_\Delta(z_s). \tag{4.13}$$

In seismic acquisition receivers are usually located below the source(s), and forward wavefield propagation must be carried out to obtain equation 4.13. In case receivers are located above the source, backward wavefield propagation must be carried out. Wavefield propagation is described by e.g., Wapenaar and Berkhout (1989) from a flat receiver level and by Sun et al. (2018) from an arbitrary receiver level. In this Chapter we only use a forward propagation step in the field data example, because in the other examples the sources and receivers are located on the same level. Forward propagation can be carried out accurately when receivers are sampled according to the Nyquist criterion. We then numerically add the receiver-ghost wavefield to obtain

$$\mathbf{D}_\delta(z_s)\mathbf{G}(z_s, z_s)\mathbf{X}(z_s, z_s)\mathbf{G}(z_s, z_s)\mathbf{S}_\Delta(z_s), \tag{4.14}$$

where the receiver-ghost wavefield is now related to the level of the sources. This step ensures that the shot records of matrix product 4.14, being our training data, are similar to the receiver gathers of matrix product 4.14, except that their spatial sampling is different. In the next step we subsample the receivers of matrix products 4.13 and 4.14 such that the spatial receiver sampling becomes identical to the coarse source sampling (see Figure 4.7c). Given that n is the rate between the source and the receiver sampling, the index k of the first detector can have values ranging from 1 to n. This means that
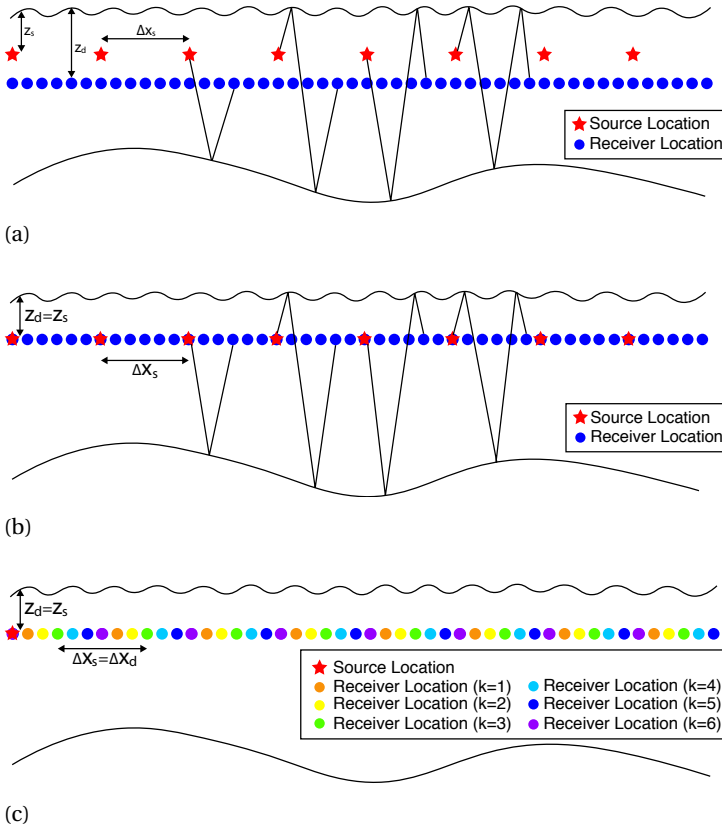
Figure 4.7: The preprocessing steps to obtain the training data. The four raypaths in a) and b) are respectively, the direct event, the source ghost, the receiver ghost and source-receiver ghost. a). The coarsely-sampled sources at source level z_s and densely-sampled receivers at receiver level z_d. b) The original receiver ghost is replaced with a receiver ghost that corresponds to receivers at the depth level of the sources ($z_d = z_s$). c) A densely-sampled shot record is subsampled for $n = 6$.

n different subsampled data sets can be made of each shot record. Only if the source and receiver locations coincide, the dataset is reciprocal (see $k = 1$ in Figure 4.7c). The n subsampled data sets, being the input training data, are obtained from matrix product 4.14 and can be formulated as:

$$\left[\mathcal{X}^{train}\right]_k = [\mathbf{D}_\Delta(z_s)]_k \mathbf{G}(z_s, z_s)\mathbf{X}(z_s, z_s)\mathbf{G}(z_s, z_s)\mathbf{S}_\Delta(z_s), \quad \text{for} \quad k = 1, 2, ..., n. \quad (4.15)$$

To obtain the output training data we subsample the receivers of matrix product 4.13 such that

$$\left[\mathcal{Y}^{train}\right]_k = [\mathbf{D}_\Delta(z_s)]_k \mathbf{X}(z_s, z_s)\mathbf{G}(z_s, z_s)\mathbf{S}_\Delta(z_s), \quad \text{for} \quad k = 1, 2, ..., n. \quad (4.16)$$

The CNN handles each shot record combination from equation 4.15 with receiver ghost and 4.16 without receiver ghost as an individual training pair. Once the network has been

trained, we apply the network to remove the source-ghost wavefield from the transposed of matrix product 4.15, which is given by:

$$\left[\mathcal{X}\right]_k = \mathbf{S}_\Delta(z_s)^T \mathbf{G}(z_s, z_s)\mathbf{X}(z_s, z_s)\mathbf{G}(z_s, z_s)[\mathbf{D}_\Delta(z_s)]_k^T, \quad \text{for} \quad k = 1, 2, ..., n. \tag{4.17}$$

Notice the similarity with equation 4.15. Therefore, we can now use the CNN to carry out the source deghosting, which results in:

$$\left[\mathcal{Y}\right]_k = \mathbf{S}_\Delta(z_s)^T \mathbf{X}(z_s, z_s)\mathbf{G}(z_s, z_s)[\mathbf{D}_\Delta(z_s)]_k^T, \quad \text{for} \quad k = 1, 2, ..., n. \tag{4.18}$$

Undoing the transposition, and using $D_\delta = \sum_{k=1}^n D_\Delta$ we obtain:

$$\mathbf{D}_\delta(z_s)\mathbf{G}(z_s, z_s)\mathbf{X}(z_s, z_s)\mathbf{S}_\Delta(z_s), \tag{4.19}$$

which after conventional receiver deghosting, carried out on the well-sampled shot records, becomes:

$$\mathbf{D}_\delta(z_s)\mathbf{X}(z_s, z_s)\mathbf{S}_\Delta(z_s). \tag{4.20}$$

If desired this can be redatumed to $\mathbf{D}_\delta(z_d)\mathbf{X}(z_d, z_s)\mathbf{S}_\Delta(z_s)$, which represents the fully deghosted version of equation 4.1. Following this approach, the network can be applied to the same data distribution to ensure the reliability of the network.

4.6. CNN Architecture

The CNN architecture used in this Chapter is based on the work of Ronneberger et al. (2015) and Quan et al. (2016) on convolutional encoder-decoder networks. These networks have been applied successfully in the medical field with a limited amount of training data and in terms of the amount of data that resembles our case. This type of network consists for example of four encoding layers and four decoding layers connected
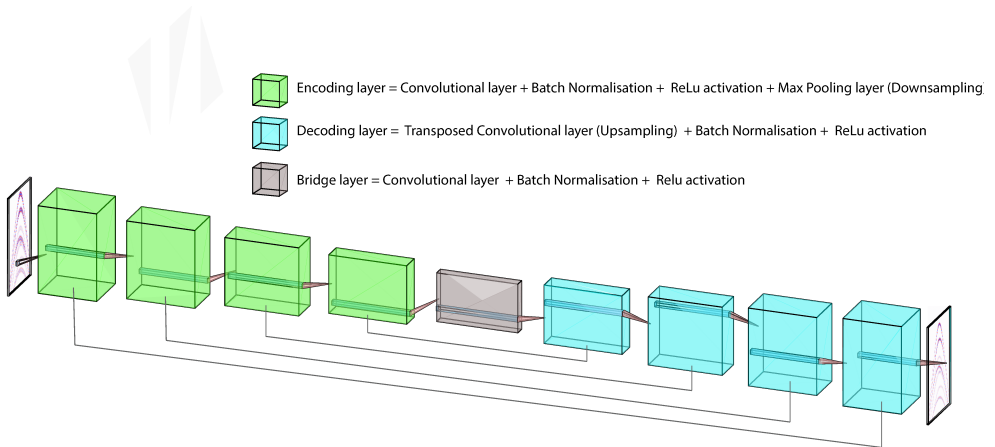

Figure 4.8: The architecture of the convolutional neural network, showing the encoder-decoder structure and the residual connections between each encoding and decoding block.

by a bridge (see Figure 4.8). Each encoding layer consist of a convolutional layer, a batch normalization layer, an activation layer and a max pooling layer. The max pooling layer downsamples the data with a factor of two in both the time and space direction. Each decoding layer consist of a transposed convolutional layer, a batch normalization layer and an activation layer. The transposed convolutional layer upsamples the data and makes sure that the number of filters is equal to its connected encoding layer. The encoding layers are connected with a summation to a corresponding decoding layer, which makes the network fully residual. The components of the bridge are similar to those of the encoding layer, but without a max pooling layer. The number of filters gradually increases towards the bridge block and then gradually decreases towards the predicted output. The activation layer consist of a ReLU (rectified linear unit) function. We used stochastic gradient descent to minimize the L2-misfit between training input and output. In addition, we modified the size of the kernel to handle the seismic data properly.

4.7. CNN SOURCE DEGHOSTING: NUMERICAL EXAMPLE

We modeled seismic data for the Marmousi velocity model shown in Figure 4.1b. We modeled 80 shot records with 1200 receivers, a spatial receiver sampling of $\delta x = 5$ m and

Table 4.1: The sensibility of the overall CNN performance of the training data, validation data and application data with respect to the number of layers, the learning rate and the filter numbers.

Network Perfomance (dB)			
Network Parameters	Training data (1200 pairs)	Validation data (300 pairs)	Application data (1200 pairs)
encoding Layers=4 decoding Layers=4 learning-rate=0.01 filter numbers=64,128,256,512,1024	27.4	23.3	22.6
encoding Layers=4 decoding Layers=4 learning-rate=0.001 filter numbers=64,128,256,512,1024	27.0	23.2	22.5
encoding Layers=4 decoding Layers=4 learning-rate=0.01 filter numbers=16,32,64,128,256	21.6	20.9	20.5
encoding Layers=3 decoding Layers=3 learning-rate=0.01 filter numbers=64,128,256,512,1024	26.7	23.2	22.5

a spatial source sampling of $\Delta x = 75$ m in a fixed spread configuration. The sources as well as the receivers were located at $z_s = z_d = 15$ m under the sea surface and now both the ghost wavefields were included in the modelling. We applied receiver subsampling with a factor $n = 15$, i.e., from $\delta x = 5$ m to $\Delta x = 75$ m to these 80 modeled shot records to obtain the input training data. To obtain the output training data we applied receiver deghosting before the receiver subsampling. In total we used 1200 training pairs, which is equal to the number of shot records, being 80, times n. We used an additional 300 pairs to validate the network and to determine the number of filters, number of layers
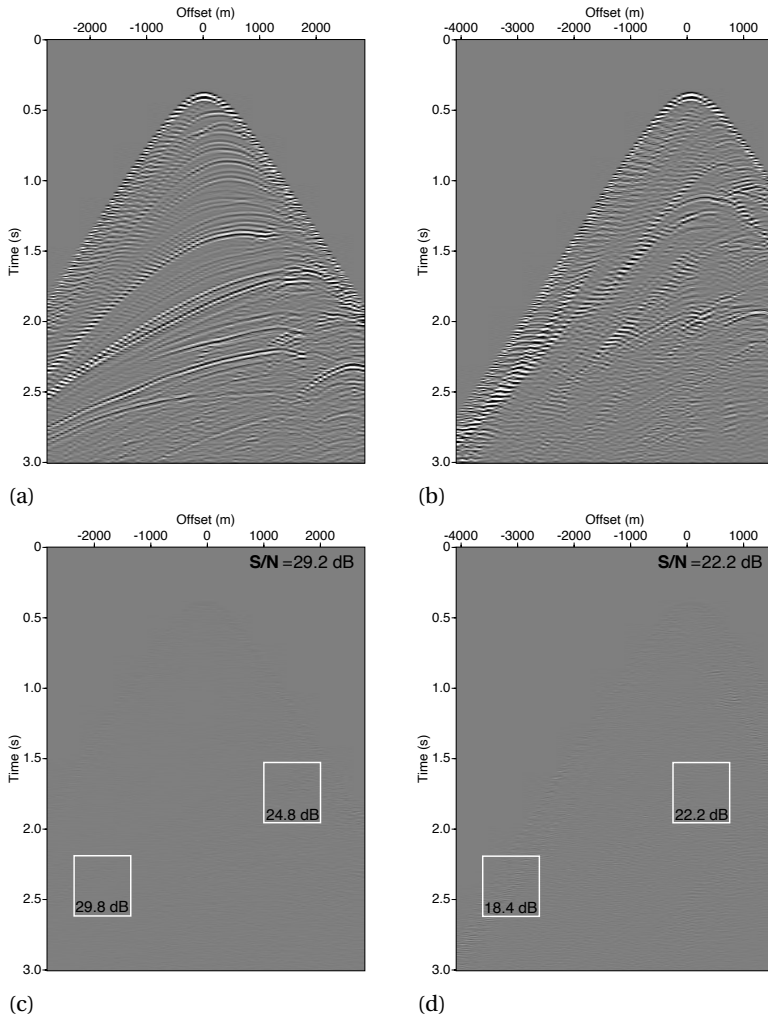

Figure 4.9: The results of the CNN for two input training shot records. a) Shot record (lateral source location: 2925 m) after CNN receiver deghosting. b) Shot record with source (lateral source location: 4725 m) after CNN receiver deghosting. c) Difference between Figure 4.9a and corresponding output training shot record. d) Difference between Figure 4.9b and corresponding output training shot record.

and the learning rate. We show the performance on the training data and validation data in Table 4.1. These results indicate that the performance of the network is quite robust with respect to changes in the learning rate and the size of the network. Only the results obtained with a smaller amount of filters significantly reduced the performance of the network. The results that we show in the data and frequency domain are obtained using a CNN with four encoding layers, four decoding layers and a learning rate of 0.01. The number of filters increases from 64 to 1024 at the bridge block, after which the filter size recursively decreases to 64.

In Figure 4.9a we show a subsampled receiver-deghosted shot record with a lateral source position of 2925 m. After training (100 epochs), the differences between the CNN receiver-deghosted shot record and its corresponding training output has an overall S/N
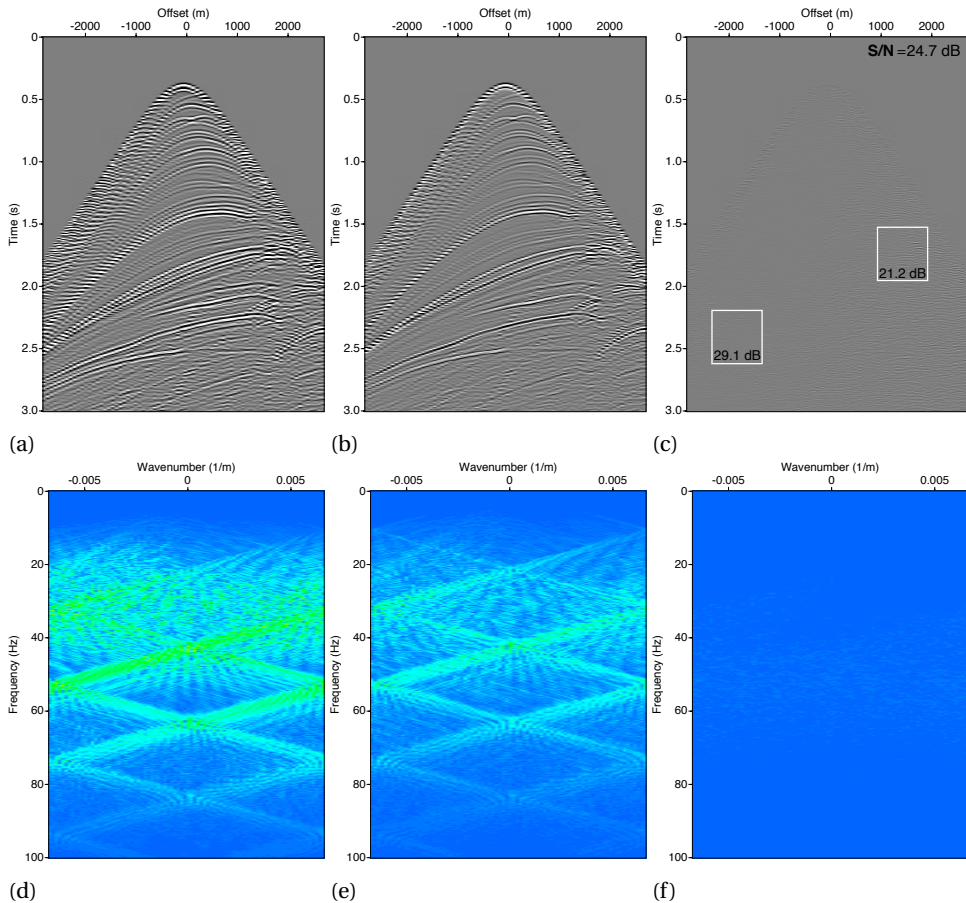

Figure 4.10: The CNN result for a coarsely sampled receiver gather with a lateral receiver location at 2890 m. a) Receiver gather including the source as well as the receiver ghost. b) Receiver gather after CNN source deghosting. c). Difference between Figure 4.10b and modeled source-ghost-free receiver gather. d), e) and f) The wavenumber-frequency spectra of Figures 4.10a, 4.10b and 4.10c.

of 29.2 dB and signal-to-noise ratios of respectively, 29.8 dB and 24.8 dB for the selected areas (see Figure 4.9c). In Figure 4.9b we show a subsampled validation record with a lateral source position of 4325 m. The differences in the selected areas with the modeled source-ghost-free receiver gathers in Figure 4.9d have signal-to-noise ratios of 18.4 dB and 22.2 dB and an overall S/N of 22.2 dB. We applied the CNN to remove the source-ghost wavefield from coarsely sampled receiver gathers as well. We show examples in Figures 4.10 and 4.11 for receiver gathers with lateral receiver locations of 2890 m and 4750 m, respectively. Note that the receiver ghost is still present. The differences in Figure 4.10c and 4.11c have signal-to-noise ratios between 16.0 dB and 29.1 dB. The wavenumber-frequency spectra show there is only a small amount of residual energy around the notch frequency of 50 Hz related to vertical propagation (see Figures 4.10f
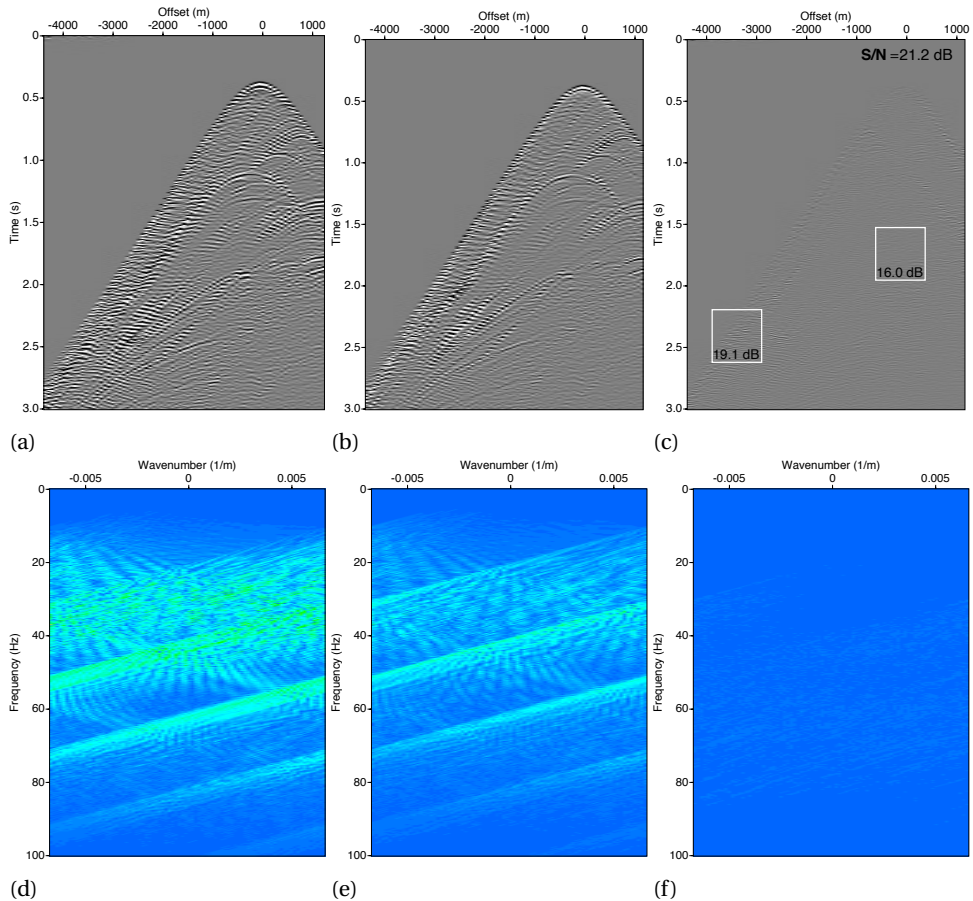

Figure 4.11: The CNN result for a coarsely-sampled receiver gather with a lateral receiver location at 4750 m. a) Receiver gather including the source as well as the receiver ghost. b) Receiver gather after CNN source deghosting. c). Difference between Figure 4.11b and modeled source-ghost-free receiver gather. d), e) and f) The wavenumber-frequency spectrum of Figures 4.11a, 4.11b and 4.11c.

and 4.11f). The CNN result gives a significant uplift compared to the source-deghosted result of Figure 4.4b. Note that the overall performance on the application data is comparable to the overall performance on the validation data (see Table 4.1).

In Figure 4.12a we show a shot record corresponding to Figures 4.10b and 4.11b. Next, we applied receiver deghosting based on sparse inversion to the well-sampled source-deghosted shot records, leading to fully deghosted records. An example of a shot record before and after receiver deghosting can be found in Figures 4.12a and 4.12b. The corresponding wavenumber-frequency spectra are shown in Figures 4.12d and 4.12e. The difference with the modeled ghost-free shot gather is shown in Figures 4.12c and 4.12f. The selected areas in Figure 4.12c have signal-to-noise ratios of 20.3 dB and 26.6
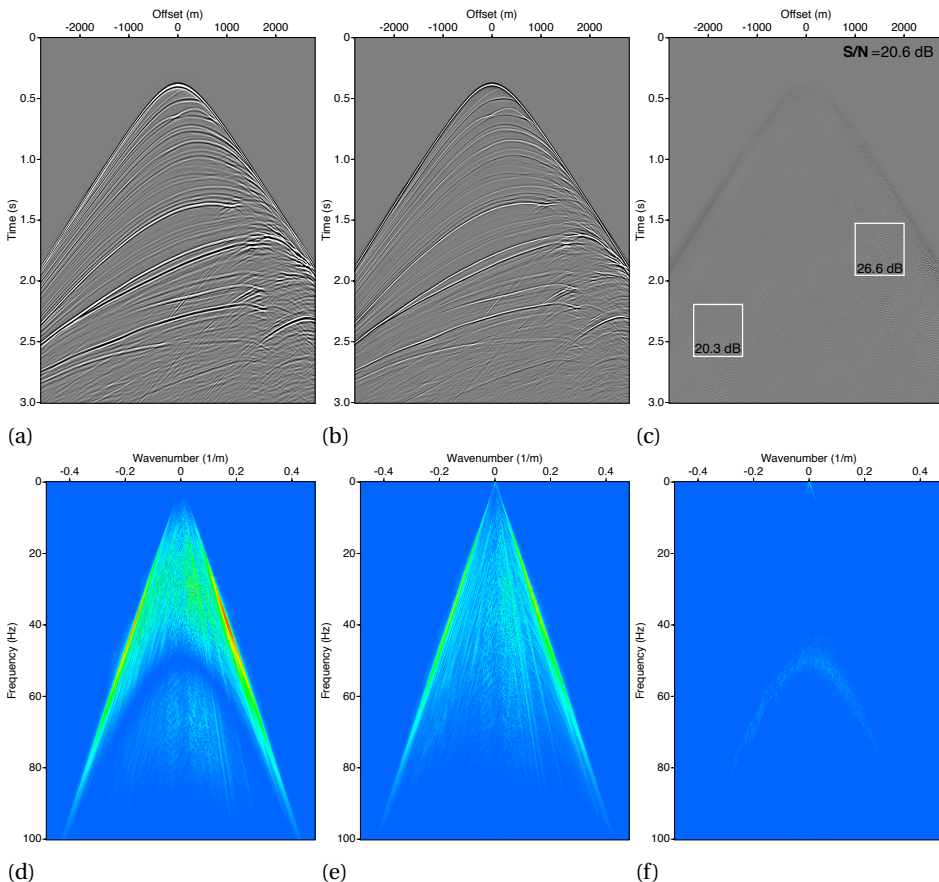
4

Figure 4.12: Receiver deghosting after source deghosting. a) Input: shot record after CNN source deghosting carried out in the common-receiver domain. b) Output: shot record of Figure 4.12a after receiver deghosting using sparse inversion carried out in the common-shot domain. c) Difference between Figure 4.12b and the modeled ghost-free shot record. d), e) and f) The wavenumber-frequency spectra of Figures 4.12a,4.12b and 4.12c.

dB and an overall S/N of 20.6 dB. Again, the result of the CNN has a higher S/N than the conventional deghosting result shown in Figure 4.5a. This is due to latter method being carried out in the 'wrong' domain, which limits it quality, while the CNN does not suffer from this issue.

4.8. CNN SOURCE DEGHOSTING: FIELD DATA EXAMPLE

We applied the machine learning approach for applying source deghosting to coarsely sampled receiver gathers taken from a field data set, acquired offshore Australia. For this
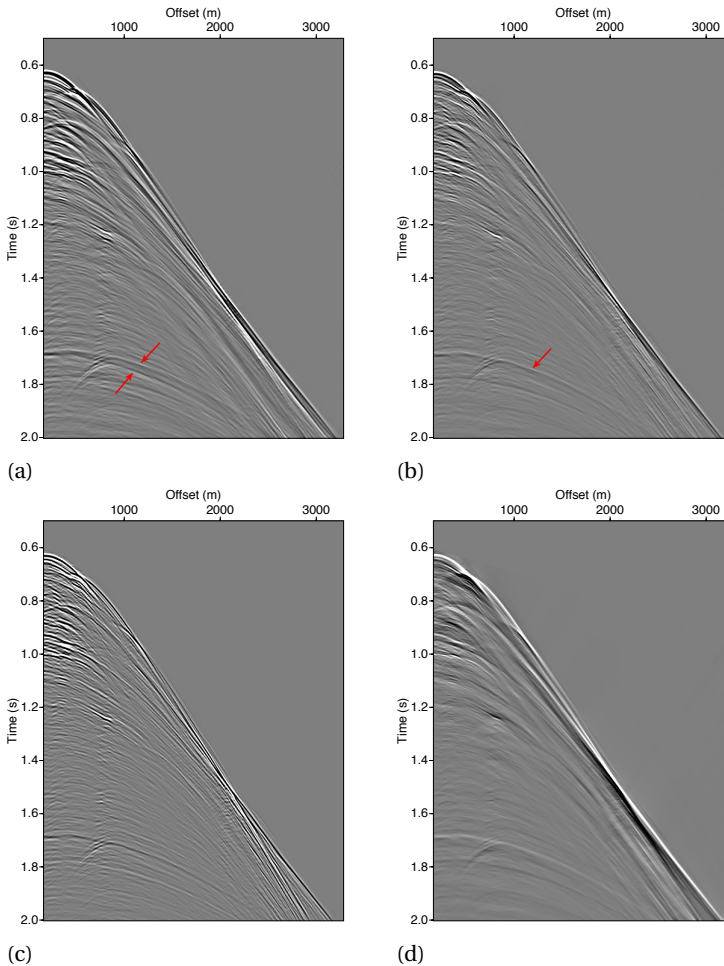

Figure 4.13: a) Shot record including the source ghost effect as well as the slanted-cable receiver ghost effect. b) Redatumed shot record including the source ghost effect. c) Redatumed shot record including source ghost effect as well as modeled receiver ghost effect. d) Shot record after CNN source deghosting and conventional receiver deghosting.

example, we took a subset of 110 shot records with a spatial source sampling of $\Delta x = 75$ m and a spatial receiver sampling of $\delta x = 6.25$ m, meaning that $n = 12$ in this example. The source depth was 5 m and the depth of the slanted cable ranged from 8 m to 60 m. A single shot record is shown in Figure 4.13a and its wavenumber-frequency spectrum in Figure 4.14a. Due to the slant of the cable, which leads to notch diversity, there is no clear receiver-ghost notch in the wavenumber-frequency spectrum. Figures 4.13b and 4.14b show the result after receiver deghosting. The arrows in Figures 4.13a and 4.13b indicate that the slanted ghost effect is removed accurately. In addition, the receivers have been redatumed to the source level of 5 m. We then numerically added the corresponding receiver-ghost wavefield, see Figure 4.13c. As expected, now a clear first-order receiver-ghost notch becomes visible in the spectrum around 150 Hz, see Figure 4.14c.
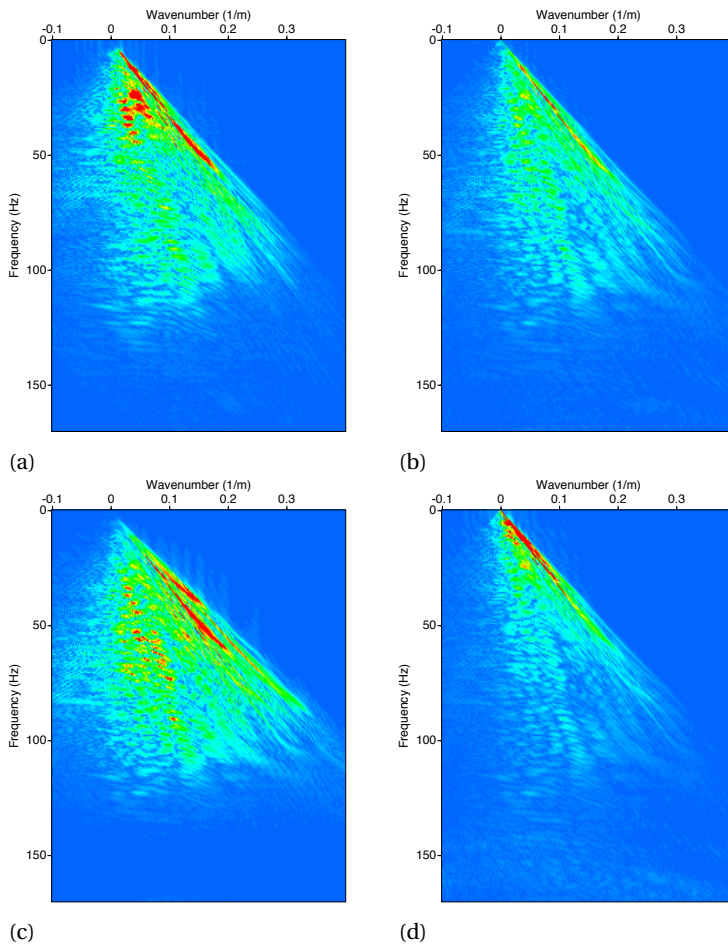

(a)   (b)

(c)   (d)

Figure 4.14: a) The wavenumber-frequency spectrum of Figure 4.13a. b) The wavenumber-frequency spectrum of Figure 4.13b. c) The wavenumber-frequency spectrum of Figure 4.13c. d) The wavenumber-frequency spectrum of Figure 4.13d.

To create the training data for the CNN, we subsampled the shot records with and without the redatumed receiver-ghost wavefield by the factor $n = 12$. The number of layers, the number of filters and the learning rate remain the same as in the numerical example discussed previously. Only the size of the kernels was adjusted to the size of the subsampled shot records from the field data. Once the network was trained (after 200 epochs) with the subsampled shot records, we applied the CNN to remove the source ghost from the coarsely sampled receiver gathers.

We then carried out receiver deghosting using sparse inversion in the densely sampled common-shot domain. A shot record from the now fully deghosted result is shown in Figure 4.13d. The reflections have the high-resolution appearance that characterizes ghost-free, wideband data, without any obvious deghosting artifacts. The corresponding wavenumber-frequency domain representation is shown in Figure 4.14d. As expected, we see that the amplitudes around the zeroth- and first-order source-ghost notches, at 0 Hz and 50 Hz respectively, have been boosted, whereas in between these notches the amplitudes have been reduced. Thus, both the shot-record and its wavenumber-frequency spectrum indicate that the source-ghost and the receiver ghost have been removed successfully.

A conventional technique to obtain the source deghosted result is to apply trace-by-trace sparse deghosting with a 1D ghost model. We compare results obtained with trace-by-trace sparse source deghosting with results obtained with CNN source deghosting for a shallow near-offset section in the common-shot domain with a minimum offset of 175 m (Figures 4.15a and 4.15b). The trace-by-trace sparse source deghosting result has some deghosting artefacts, which are most visible near the water-bottom reflection. These artefacts might be related to the relatively weak angle-dependancy of the ghost.
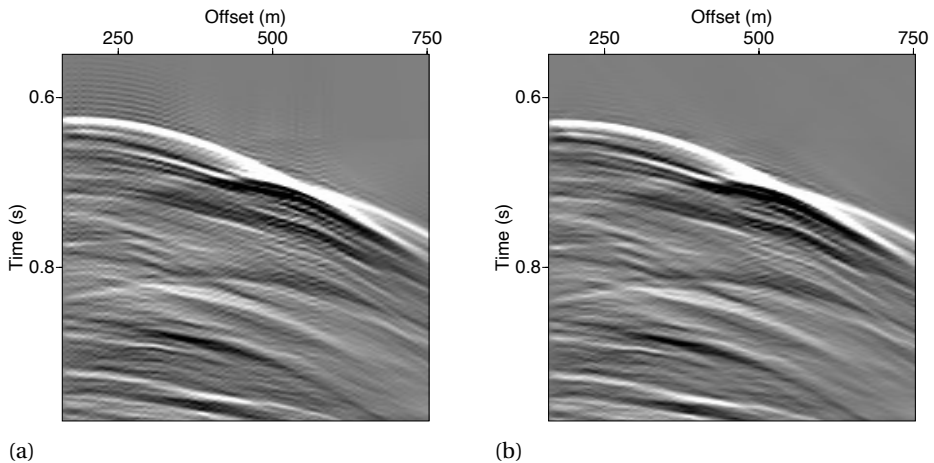

(a) (b)

Figure 4.15: a) A near-offset section after sparse receiver deghosting and trace-by-trace sparse source deghosting. b) A near-offset section sparse receiver deghosting and CNN source deghosting. d
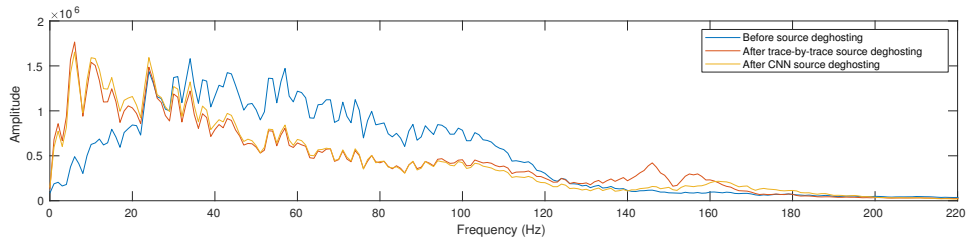
Figure 4.16: The stacked frequency spectra corresponding to Figures 4.15a and 4.15b and before receiver deghosting.

They are not present in the CNN source deghosting result. As an additional quality control we compare the corresponding stacked frequency spectra of Figures 4.15a and 4.15b in Figure 4.16. We also show the frequency spectrum before source deghosting. Figure 4.16 shows that the observed artefacts after trace-by-trace source deghosting are the result of over-amplified amplitudes in the notch area, which confirms that these artefacts are the result of neglecting the angle-dependancy of the ghost.

4.9. Discussion

This Chapter demonstrated the capabilities of a machine learning approach for removing the source-ghost wavefield from coarsely sampled data. It is a first step towards a fully 3D source wavefield deghosting method that is suitable for coarsely sampled data. Other seismic processing methods such as source redatuming, which are limited by coarsely sampled data, might benefit from a comparative strategy. One of the challenges in 3D would be the different azimuth distribution between the redatumed and subsampled shot gathers, and the aliased receiver gathers. In principle the method can handle irregular geometries by adjusting the subsampling or if necessary interpolating the training data to the required irregular sampling geometry. Another challenge is to account for variations between the source and receiver ghost wavefield due to rough sea surface effects. A rough sea surface causes asymmetry between the source ghost and the receiver ghost throughout a survey. The source ghost is almost instantaneous and therefore, accurately described by an effective static sea surface model. However, the receiver ghost could only be handled by a dynamic sea surface model. In such a case, the receiver ghost must first be removed using a method that can handle a dynamic rough sea surface (e.g. Grion and Telling, 2016; King and Poole, 2015; Vrolijk and Blacquière, 2020b). Subsequently, an effective static sea surface model could be included during the modelling of the receiver ghost wave field on the source depth. It is also known that e.g., ghost cavitation causes asymmetry between the source side and the receiver side. The field data results indicated that the CNN might be able to deal with the non-linear source effects since no obvious deghosting artefacts effects were present. Including the exact source effects, azimuthal differences and rough sea surface effects in the training data could be challenging and further research is required. In addition, comparing our proposed method with existing deep learning interpolation schemes (Garg et al., 2019;

Siahkoohi et al., 2019a; Wang et al., 2020) followed by, e.g., a sparse source deghosting method could also provide more insight in its capabilities.

It is expected that the method can be easily adapted to be suitable for application to coarsely sampled common-shot gathers acquired with ocean-bottom nodes. After source deghosting and redatuming of the sources to the ocean-bottom, the training of the CNN can be carried out on subsampled common-receiver gathers with and without modelled source ghost wavefield. Then the CNN could be applied to coarsely sampled common-shot gathers to remove the receiver ghost wavefield.

4.10. CONCLUSIONS

We successfully applied a CNN to remove the source-ghost wavefield from coarsely sampled receiver gathers. The key is that we used the symmetry that exists between source deghosting in the common-receiver domain and receiver deghosting in the common-shot domain. As receiver deghosting in the well-sampled common-shot domain is relatively easy, we proposed a strategy to train the CNN with subsampled shot records before and after receiver deghosting. Because of the symmetry, this case mimics the situation of coarsely sampled receiver gathers before and after source deghosting. Tests on numerical as well as field data show that our approach can accurately remove the source-ghost wavefield from coarsely sampled receiver gathers. These results are better than those obtained from adaptive source deghosting in the well-sampled common-shot domain.

5

CONCLUSIONS AND RECOMMENDATIONS

5.1. Conclusions

The main focus in this thesis was on improving the removal of the ghost wavefield in seismic data processing. Although, this so-called deghosting is a well-established methodology in seismic data processing, it is known that most deghosting techniques only perform well under ideal conditions, such as a flat sea surface, carpet shooting and carpet recording. In practise, however, these ideal conditions are almost never met, which raised the following question: can we develop (a) deghosting algorithm(s) that perform(s) well even under challenging conditions, such as a dynamic sea surface and coarse spatial source sampling?

Another topic that played an important role in this thesis was 'integrated methods'. Integrated methods can increase the efficiency of the seismic processing workflow by reducing the time required for quality control. We also investigated whether our integrated methods offer higher quality than a sequential workflow

In Chapter 2, we integrated receiver deghosting and closed-loop surface related multiple elimination (CL-SRME). We extended the CL-SRME scheme with a receiver ghost operator that takes into account wavefield propagation between the level of the receivers and the sea surface. We have presented the extended CL-SRME schemes for a horizontal streamer geometry as well as a slanted streamer geometry. The numerical data results showed that extended CL-SRME is more accurate than a standard least-squares receiver deghosting algorithm followed by CL-SRME. The field data results confirmed that extended CL-SRME was capable of successfully removing the surface related multiples as well as the receiver ghost reflections, without deghosting artifacts. In conclusion, we proved that it is possible to efficiently integrate CL-SRME and receiver deghosting to improve the data quality.

In Chapter 3, we discussed a deterministic as well as an adaptive receiver deghosting algorithm based on sparse inversion. The deterministic algorithm requires the exact ghost model, while the adaptive algorithm only requires a simplified ghost model, i.e., assuming a flat sea surface, and an estimate of the actual receiver depth. If the exact ghost model is known, the deterministic receiver deghosting algorithm will provide superior results. However, in practise, the exact ghost model is unknown due to a dynamic sea surface and streamer movement that affect the ghost model in a way that only an adaptive receiver deghosting algorithm can handle. An integrated approach was proposed to simultaneously estimate the ghost model parameters and perform receiver deghosting. The numerical data results showed that for a dynamic sea surface and small variations in the depth profile of the streamer, the adaptive receiver deghosting results were superior to the deterministic receiver deghosting results. The field data results confirmed that the adaptive receiver deghosting algorithm can provide ghost-free, broadband data, without any obvious deghosting artifacts. The field data results also showed that the adaptive receiver deghosting algorithm has the potential to significantly improve the poor low frequency SNR, which is common in the accelerometer measurements of a multi-component recording system. Overall, we conclude that our integrated adaptive deghosting algorithm improves image quality if the receiver ghost model for a

dynamic sea surface and an arbitrary streamer geometry is not known exactly.

In Chapter 4, we discussed the source ghost dilemma: the quality of source deghosting is often limited by a coarse spatial source sampling in the common-receiver domain, while in the common-shot domain it is limited by the complex subsurface. We proposed a machine learning approach for source deghosting the coarsely-sampled receiver gathers. The machine learning approach is based on an encoder-decoder convolutional neural network (CNN). The key of the method is to obtain input and output training data that ensure that the CNN generalizes well. Obtaining such a representative training data set is often a challenge in geophysical applications, especially for processing purposes. In our approach the training data sets consist of subsampled shot records with and without the receiver ghost wavefield, which are relatively easy to obtain from the data itself. Because of reciprocity, these training data are representative for source deghosting common-receiver gathers with coarse spatial source sampling. A numerical test showed that our trained neural network is able to accurately remove the source ghost wave field and we validated the method on a field data set as well. We showed that the quality of CNN source deghosting can be higher than a conventional source deghosting approach. More generally, we have proven that CNN source deghosting is a promising method in case coarse spatial source sampling is a limitation.

5.2. RECOMMENDATIONS FOR FURTHER RESEARCH

In this section we make some recommendations for further research. We also show some initial results related to some of these recommendations.

5.2.1. SOURCE DEGHOSTING INCLUDING DYNAMIC SEA SURFACE

In Chapter 3 we focused on removing the receiver ghost that has reflected from a dynamic sea surface. Blacquière and Sertlek (2019) developed a modeling strategy to construct a source ghost wavefield for the case of a dynamic sea surface, by using an effective static sea surface. This effective static sea surface is a realistic representation of the dynamic sea surface due to the almost instantaneous interaction time of the source wavefield with the sea surface. We used their modeling strategy to obtain two synthetic data sets with a source ghost for sea state 6 and an extreme sea state 8. These sea states are related to a significant wave height of 4-6 m and a significant wave height of 9-14 m, respectively (e.g., Ainslie, 2010). Zoomed-in sections of these modeled receiver gathers are given in Figures 5.1a and 5.1d. The time jitter due to the dynamic sea surface becomes clear in the extreme case (Figure 5.1d). In Figures 5.1b and 5.1e we show the initial results we obtained with our adaptive method from Chapter 3, now being applied as a source deghosting method. The adaptive source deghosting method provides a higher-quality than a deterministic source deghosting algorithm that would neglect the effect of the dynamic sea surface. The differences with the modeled source ghost-free data are given in Figures 5.1c and 5.1f and are respectively, 46.1 dB and 40.3 dB. These initial results are very promising and it would be worthwhile to apply the adaptive source deghosting method to a field data set, acquired during rough weather conditions.
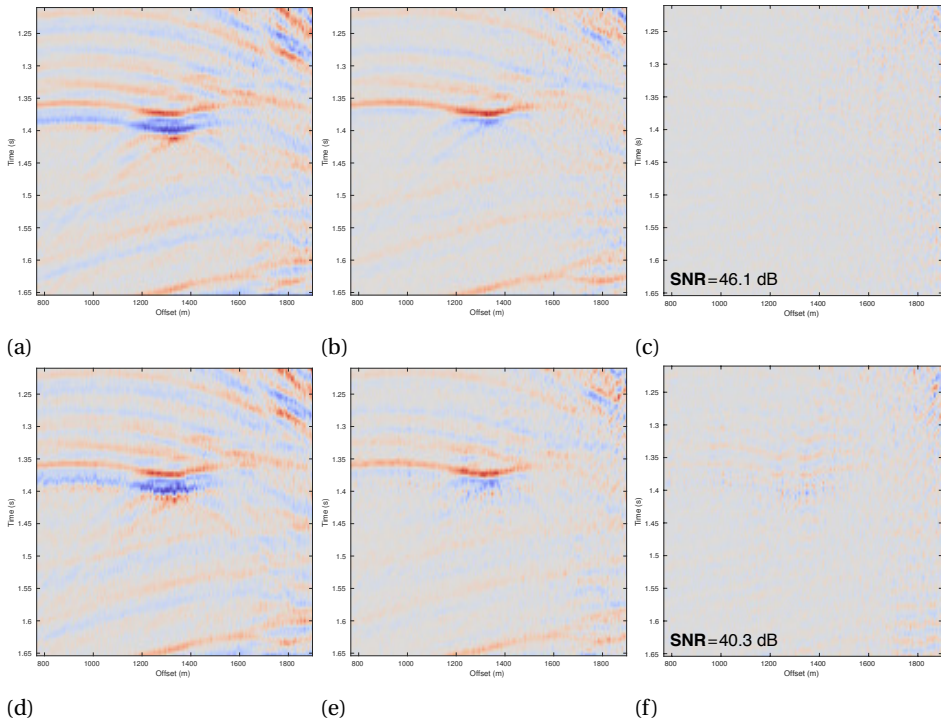
Figure 5.1: Zoomed-in sections of receiver gathers. In a) the receiver gather with ghost effect for sea state 6, sources are at $z_d = 20$ m, b) output for a) after adaptive source deghosting, c) residual for b) after adaptive source deghosting, d) the receiver gather with ghost effect for sea state 9, sources are at $z_d = 20$ m e) output for d) after adaptive source deghosting, f) residual for e) after adaptive source deghosting. Figure taken from Vrolijk and Blacquière (2018)

5.2.2. EXTENSION TO 3D

The theory described in Chapter 3 could be directly applied to 3D source or receiver deghosting for data acquired with carpet shooting or carpet recording. In practise, e.g. VSP and OBC data can meet the sampling requirements to enable 3D (adaptive) source deghosting. In Figure 5.2 we show the potential of 3D adaptive deghosting for a single reflection and its ghost reflection from a rough, static sea surface and sources located at a depth of 30 m. In Figures 5.2a and 5.2d we show an inline cross-section and time-snapshot, respectively. Figures 5.2b and 5.2e show the same inline cross-section and time-snapshot after deterministic deghosting assuming a flat sea surface. These results show quite some deghosting artifacts. The quality obtained with our 3D adaptive deghosting algorithm is much higher, i.e. there are clearly fewer deghosting artifacts present, see Figures 5.2c and 5.2f. The small amplitude loss indicates that the 3D adaptive method might require further improvement. In addition, the 3D method should be tested on more realistic synthetic data and field data as well.
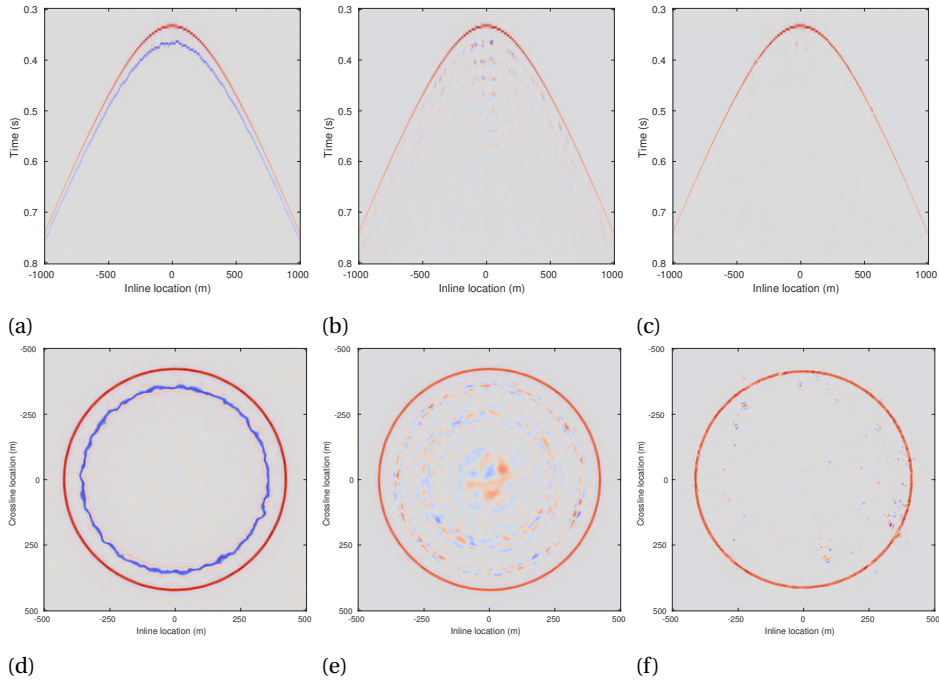
Figure 5.2: Inline cross-section a) for an event and its corresponding ghost wavefield with detectors at 30 m for a rough sea surface. Inline cross-section b) after deterministic closed-loop deghosting. Inline cross-section c) after adaptive closed-loop deghosting. Time-snapshot d) corresponding to Figure 5.2a. Time-snapshot e) corresponding to Figure 5.2b. Time-snapshot f) corresponding to Figure 5.2c. Figure taken from Vrolijk and Blacquière (2018)

However, a greater challenge is the case that we do not have sufficient source or receiver sampling in the inline and/or crossline direction. Tang and Campman (2017) integrated receiver interpolation with wavefield decomposition to solve the sampling issue for multi-component data. Sun and Verschuur (2017) proposed a method that implicitly handles coarsely-sampled common-shot data. In Chapter 4 we made an initial step towards source deghosting of coarsely-sampled common-receiver data using a CNN. One of the remaining challenges would be to optimize the machine learning to deal efficiently with 3D common-receiver gathers. Even though the size of coarsely sampled common-receiver gathers is relatively small compared to the size of fully sampled common-receiver gathers, our method is still computationally expensive. This is because in our current tests, the training was done from scratch on new data. To optimize this process we recommend to investigate the possibilities of transfer learning, i.e., from one data set to another. But transfer learning can also be used within a data set, e.g. by using the training results of a select part of the data as initialization for training the rest of the data. We also recommend extending the machine learning strategy to a source interpolation tool, which could be done relatively easy by adding the number of decoder blocks and/or changing the size of these blocks. After this, the result can be compared

or might be even combined with existing interpolation schemes that are also based on machine learning (Garg et al., 2019; Siahkoohi et al., 2018).

The extension of the CL-SRME algorithm towards 3D is ongoing research. Zhang and Verschuur (2019) proposed to integrate CL-SRME into full wavefield migration (FWM). In this way multiples can help to fill in the acquisition gaps. Again, the receiver ghost can be integrated in the same way as demonstrated in Chapter 2. We also recommend investigating the impact of separately integrating the receiver ghost and/or source ghost into FWM.

5.2.3. Integrated versus sequential

Another interesting research direction, may be to compare the results of extended CL-SRME with the results of deterministic receiver deghosting (Chapter 3) followed by standard CL-SRME. Both CL-SRME and deterministic receiver deghosting are based on sparse inversion. It is expected that extended CL-SRME can provide higher quality data, because its solution allows greater sparsity. Recently, Aharchaou and Neumann (2020) demonstrated that mainly for this reason, the quality of their integrated broadband preprocessing method for towed streamer data is higher than the quality of their sequential workflow. Predicting the outcome of integrating adaptive receiver deghosting and CL-SRME is a bit more uncertain. To integrate adaptive receiver deghosting into CL-SRME, the update of the ghost model parameters must be included in the algorithm, and therefore the total number of parameters in the inversion increases. This makes the algorithm more sensitive to converging to a wrong solution. We recommend to investigate the possibility of successfully integrating adaptive receiver deghosting into CL-SRME.

A

DERIVATION OF GRADIENTS

In this appendix we derive the gradients of equations 3.7, 3.8, 3.13 and 3.14. The derivation of the gradients is based on the rules of complex-valued derivatives of vector and matrix functionals (see e.g. Haykin, 2002; Hjørungnes, 2011; Petersen and Pedersen, 2012). At first, we derive the gradient of $J_1 = \sum_\omega ||\hat{V}||_F$ with respect to $\hat{X}(\omega')$ (equations 3.7 and 3.13). Lopez and Verschuur (2015) describe a similar derivation with respect to the gradient used in closed-loop surface multiple estimation. For clarification we drop the subscripts j and m. According to Haykin (2002) the gradient of the real-valued function J_1 with respect to the complex vector $\hat{X}(\omega')$ is given by

$$\nabla_{\hat{X}(\omega')} J_1 = 2 \frac{dJ_1}{d\hat{X}(\omega')^*}, \tag{A.1}$$

where the function J_1 being the Frobenius norm with respect to the data residual vector $\hat{V}$ summed over all frequencies could be written by

$$J_1 = \sum_\omega ||\hat{V}||_F = \sum_\omega \hat{V}^H \hat{V} = \sum_\omega Tr(\hat{V}\hat{V}). \tag{A.2}$$

We rewrite the differential equation to be:

$$\frac{dJ_1}{d\hat{X}(\omega')^*} = \frac{d\hat{V}^H}{d\hat{X}^*(\omega')}\hat{V} + \hat{V}^H \frac{d\hat{V}}{d\hat{X}^*(\omega')}, \tag{A.3}$$

where we eliminate the summation $\sum_\omega$, because only for $\omega = \omega'$ there is a non-zero contribution to the derivative with respect to $\hat{X}(\omega')$ (Lopez and Verschuur, 2015). According to Haykin (2002) the second term of equation A.3 has no contribution to the gradient because $\frac{d\hat{V}}{d\hat{X}^*(\omega')} = 0$. We substitute $\hat{V}^H = (\hat{P} - \mathbf{G}\hat{X})^H$ into equation A.3 to obtain

$$\frac{dJ_1}{d\hat{X}(\omega')^*} = \frac{d(P - \mathbf{G}\hat{X})^H}{d\hat{X}^*}\hat{V} = \frac{d(P^H - \hat{X}^H \mathbf{G}^H)}{d\hat{X}^*}\hat{V}, \tag{A.4}$$

where $\frac{d(\hat{P}^H)}{d\hat{X}^*} = 0$, then the derivative according to Haykin (2002) is given by

$$\frac{dJ_1}{d\hat{X}(\omega')^*} = -\frac{d(\hat{X}^H \mathbf{G}^H)}{d\hat{X}^*}\hat{V} = -\mathbf{G}^H \hat{V}, \tag{A.5}$$

which we substitute into equation A.1 to obtain

$$\nabla_{\hat{X}(\omega')} J_1 = -2\mathbf{G}^H \hat{V}. \tag{A.6}$$

We continue with the derivation of the gradient of J_1 with respect to $\hat{\mathcal{D}}$ (equation 3.18). The matrix $\hat{\mathcal{D}}$ only has real values along the diagonal that represent the receiver depth with respect to the sea surface $\hat{\delta}$. According to Petersen and Pedersen (2012) the gradient of the real-valued function $J1$ with respect to $\Re\hat{\mathcal{D}}$ is given by

$$\nabla_{\hat{\mathcal{D}}} J_1 = \nabla_{\Re\hat{\mathcal{D}}} J_1 = \frac{dJ_1}{d\Re\hat{\mathcal{D}}}, \tag{A.7}$$

where we use the chain rule to expand the derivate term of equation A.7

$$\frac{dJ_1}{d\hat{\mathcal{D}}} = \frac{d\mathbf{G}^*}{d\Re\hat{\mathcal{D}}}\frac{dJ_1}{d\mathbf{G}^*} + \frac{d\mathbf{G}}{d\Re\hat{\mathcal{D}}}\frac{dJ_1}{d\mathbf{G}}. \tag{A.8}$$

In a steepest-descent method for a scalar real-valued function we only use the first term because the function decreases the fastest in the direction $\frac{dJ_1}{d\mathbf{G}^*}$ (see Hjørungnes, 2011). According to Staal (2015) we compute the derivative operator $\frac{d\mathbf{G}^*}{d\Re\hat{\mathcal{D}}}$. We substitute equation A.2 into the derivative term $\frac{dJ_1}{d\mathbf{G}^*}$ to obtain

$$\frac{dJ_1}{d\mathbf{G}^*} = \sum_\omega \frac{d}{d\mathbf{G}^*} Tr(\hat{V}\hat{V}^H). \tag{A.9}$$

We substitute $\hat{V}^H = (\hat{P} - \mathbf{G}\hat{X})^H$ into equation A.9 to obtain

$$\frac{dJ_1}{d\mathbf{G}^*} = \sum_\omega \frac{\hat{V}dTr(\hat{P} - \mathbf{G}\hat{X})^H}{d\mathbf{G}^*} = \sum_\omega \hat{V}\frac{dTr(P - \hat{X}^H \mathbf{G}^H)}{d\mathbf{G}^*}, \tag{A.10}$$

where $\frac{d\hat{P}}{d\mathbf{G}^*} = 0$, then the derivative according to Hjørungnes (2011) is given by

$$\frac{dJ_1}{d\mathbf{G}^*} = -\sum_\omega \frac{\hat{V}dTr(\hat{X}^H \mathbf{G}^H)}{d\mathbf{G}^*} = -\sum_\omega \hat{V}\hat{X}^H, \tag{A.11}$$

which we substitute into equation A.7 to obtain

$$\nabla_{\hat{\mathcal{D}}} J_1 = -\sum_\omega \frac{d\mathbf{G}^*}{d\Re\hat{\mathcal{D}}}\hat{V}\hat{X}^H. \tag{A.12}$$

REFERENCES

Aaron, P., R. O'Toole, S. Barnes, R. F. Hegge, and R. G. van Borselen, 2008, True-azimuth versus zero-azimuth 3-D multiple prediction in WATS processing: 78th Annual International Meeting, SEG, Expanded Abstracts, 2431–2435.

Abma, R. L., M. M. N. Kabir, K. H. Matson, S. Mitchell, S. A. Shaw, and W. McLain, 2005, Comparisons of adaptive subtraction methods for multiple attenuation: The Leading Edge, **24**, 277–280.

Aharchaou, M., and E. Neumann, 2020, An integrated broadband preprocessing method for towed-streamer seismic data: Geophysics, **85**, no. 2, V201–V221.

Ainslie, M. A., 2010, Principles of sonar performance modelling: Axel Springer.

Amundsen, L., 1993, Wavenumber-based filtering of marine point-source data: Geophysics, **58**, 1335–1348.

———, 2017, Broadband seismic over/under sources and their designature-deghosting: Geophysics, **82**, no. 5, P61–P73.

Amundsen, L., and H. Zhou, 2013, Low-frequency seismic deghosting: Geophysics, **78**, no. 2, WA15–WA20.

Amundsen, L., H. Zhou, A. Reitan, and A. B. Weglein, 2013, On seismic deghosting by spatial deconvolution: Geophysics, **78**, no. 6, V267–V271.

Araya-Polo, M., J. Jennings, A. Adler, and T. Dahlke, 2018, Deep-learning tomography: The Leading Edge, **37**, 58–66.

Baardman, R. H., D. J. Verschuur, R. G. van Borselen, M. O. Frijlink, and R. F. Hegge, 2010, Estimation of primaries by sparse inversion using dual sensor data: 80th Annual International Meeting, SEG, Expanded Abstracts, 3468–3472.

Beasley, C. J., R. C. Y. Ji, and J. Perdomo, 2013, Wave equation receiver deghosting: a provocative example: 83rd Annual International Meeting, SEG, Expanded Abstracts, 133–135.

Berkhout, A. J., 1982, Seismic migration, imaging of acoustic energy by wave field extrapolation, A: theoretical aspects: Elsevier (second edition).

———, 1985, Seismic migration, imaging of acoustic energy by wave field extrapolation, A: theoretical aspects: Elsevier (third edition).

———, 2012, Blended acquisition with dispersed source arrays: Geophysics, **77**, no. 4, A19–A23.

Berkhout, A. J., and G. Blacquière, 2016, Deghosting by echo-deblending: Geophysical Prospecting, **64**, 406–420.

Berkhout, A. J., and D. J. Verschuur, 1997, Estimation of multiple scattering by iterative inversion, part I: theoretical considerations: Geophysics, **62**, 1586–1595.

Blacquière, G., and H. Ö. Sertlek, 2018, Modeling and assessing the effects of the sea surface, from being flat to being rough and dynamic: Geophysics, **84**, no. 2, 1MA–Z11.

———, 2019, Modeling and assessing the effects of the sea surface, from being flat to being rough and dynamic: Geophysics, **84**, no. 2, 1MA–Z11.

A

Caporal, M., G. Blacquière, and M. Davydenko, 2018, Broadband imaging via direct inversion of blended dispersed source array data: Geophysical Prospecting, **66**, 942 – 953.

Caprioli, P., K. Özdemir, D.-J. van Manen, S. Mahat, A. Özbek, E. Kragh, and P. Christie, 2012, Combination of multi-component streamer pressure and vertical particle velocity: theory and application to data: 82nd Annual International Meeting, SEG, Expanded Abstracts, https://dx.doi.org/10.1190/segam2012–1144.1.

Caprioli, P., J. Roth, J. Rickett, and M. Vassallo, 2019, Joint adaptive deghosting and designature: 81th Annual International Meeting, EAGE, Extended Abstracts, 1–5.

Cecconello, E., E. Asgedom, O. Orji, and W. Söllner, 2017, Modelling of time-varying rough sea surface ghosts and source deghosting by integral inversion: 86th Annual International Meeting, EAGE, Extended Abstracts, Th A4 05.

Cecconello, E., E. Asgedom, and W. Söllner, 2019, Source deghosting and demultiple for calm and rough weather conditions: 88th Annual International Meeting, EAGE, Extended Abstracts, Th R04 02.

Cecconello, E., and W. Söllner, 2020, Realistic weather conditions and removal of time-varying sea-surface effects: Application on ocean-bottom-cable data: Geophysics, **85**, no. 3, V297–V315.

Das, V., A. Pollack, U. Wollner, and T. Mukerji, 2019, Convolutional neural network for seismic impedance inversion: Geophysics, **84**, R869–R880.

Day, A., T. Klüver, W. Söllner, H. Tabti, and D. Carlson, 2013, Wavefield-separation methods for dual-sensor towed-streamer data: Geophysics, **78**, no. 2, WA55–WA70.

Dellinger, J., A. Ross, D. Meaux, A. Brenders, G. Gesoff, J. Etgen, J. Naranjo, G. Openshaw, and M. Harper, 2016, Wolfspar®, an "FWI-friendly" ultralow-frequency marine seismic source: 86th Annual International Meeting, SEG, Expanded Abstracts, 4891–4895.

Dragoset, W. H., I. Moore, M. Yu, and W. Zhao, 2008, 3D general surface multiple prediction: An algorithm for all surveys: 78th Annual International Meeting, SEG, Expanded Abstracts, 2426–2430.

Egorov, A., S. Glubokovskikh, A. Bóna, R. Pevzner, B. Gurevich, and M. Tokarev, 2018, How rough sea affects marine seismic data and deghosting procedures: Geophysical Prospecting, **66**, 3–12.

Ferber, R., and C. J. Beasley, 2014, Simulating ultra-deep-tow marine seismic data for receiver deghosting: 76th Annual International Meeting, EAGE, Extended Abstracts, Th ELI1 14.

Ferber, R., P. Caprioli, and L. West, 2013, L1 pseudo-vz estimation and deghosting of single-component marine towed-streamer data: Geophysics, **78**, no. 2, WA21–WA26.

Garg, A., A. Vos, N. Bortych, D. Gupta, and D. Verschuur, 2019, Spatial aliasing removal using deep learning super-resolution: First Break, **37**, 87–92.

Geldart, L. P., and R. E. Sheriff, 2004, Problems in exploration seismology and their solutions: Society of Exploration Geophysicists.

Gisolf, A., and D. J. Verschuur, 2010, The principles of quantitative acoustical imaging: EAGE publications bv.

Glinsky, M. E., G. A. Clark, P. K. Z. Cheng, K. R. S. Devi, J. H. Robinson, and G. E. Ford, 2001, Automatic event picking in prestack migrated gathers using a probabilistic neural network: Geophysics, **66**, 1488–1496.

Grion, S., and R. Telling, 2016, Rough sea estimation for phase-shift de-ghosting: 86th Annual International Meeting, SEG, Expanded Abstracts, 5129–5133.

——, 2017, Estimation of a time-varying sea-surface profile for receiver-side deghosting: 87th Annual International Meeting, SEG, Expanded Abstracts, 4854–4858.

Grion, S., R. Telling, and J. Barnes, 2015, De-ghosting by kurtosis maximisation in practice: SEG, Expanded Abstracts, 4605–4609.

Guitton, A., and D. J. Verschuur, 2004, Adaptive subtraction of multiples using the l1-norm: Geophysical Prospecting, **52**, 27–38.

Hampson, G., 2017, Notional ghosts: 87th Annual International Meeting, SEG, Expanded Abstracts, 111–115.

Haumonte, L., L. Velay, and M. Manin, 2016, In situ test results obtained in the mediterranean sea with a novel marine seismic acquisition system (freecable): 86th Annual International Meeting, SEG, Expanded Abstracts, 51–55.

Haykin, S., 2002, Adaptive filter theory: Prentice Hall.

Hjørungnes, A., 2011, Complex-valued matrix derivatives with applications in signal processing in communications: Cambridge University Press.

Hopperstad, J.-F., R. Laws, and E. Kragh, 2008, Where is the center of a multi-depth marine source array?: 78th Annual International Meeting, SEG, Expanded Abstracts, 40–44.

Huang, L., X. Dong, and T. E. Clee, 2017, A scalable deep learning platform for identifying geologic features from seismic attributes: The Leading Edge, **36**, 249–256.

Khodabandeloo, B., and M. Landrø, 2018, Acoustically induced cavity cloud generated by air-gun arrays comparing video recording and acoustic data to modeling: Journal of Acoustical Society of America, **143**, 3383.

King, S., and G. Poole, 2015, Hydrophone-only receiver deghosting using a variable sea surface datum: 85th Annual International Meeting, SEG, Expanded Abstracts, 4610–4614.

Konuk, T., and J. Shragge, 2018, Mimetic finite-difference modeling of time-varying sea-surface effects on seismic data.: 88th Annual International Meeting, SEG, Expanded Abstracts, 3948–3952.

Kragh, E., J. Robertsson, R. Laws, L. Amundsen, T. Røsten, T. Davies, K. Zerouk, and A. Strudley, 2004, Rough-sea deghosting using wave heights derived from low-frequency pressure recordings — a case study: 74th Annual International Meeting, SEG, Expanded Abstracts, 1309–1312.

Kryvohuz, M., and X. Campman, 2017, Source-side up-down wavefield separation using dual NFHs: 79th Annual International Meeting, EAGE, Extended Abstracts, 111–115.

Landrø M., L. Amundsen, and D. Barker, 2011, High-frequency signals from air-gun arrays: Geophysics, **76**, no. 4, Q19–Q27.

Laws, R., and E. Kragh, 2002, Rough seas and time-lapse seismic: Geophysical Prospecting, **50**, 195–208.

Leroy, C. C., S. P. Robinson, and M. J. Goldsmith, 2008, A new equation for the accurate calculation of sound speed in all oceans: Journal of Acoustical Society of America, **124**, 2774–2782.

Letki, L. P., and C. Spjuth, 2014, Quantification of wavefield reconstruction quality from multisensor streamer data using a witness streamer experiment: 76th Annual Interna-

tional Meeting, EAGE, Extended Abstracts, 1–4.

Lewis, W., and D. Vigh, 2017, Deep learning prior models from seismic images for full-waveform inversion: 87th Annual International Meeting, SEG, Expanded Abstracts, 1512–1517.

Lin, T. Y., and F. J. Herrmann, 2013, Robust estimation of primaries by sparse inversion via one-norm minimization: Geophysics, **78**, R133–R150.

Lopez, A. G., and D. J. Verschuur, 2015, Closed-loop surface-related multiple elimination and its application to simultaneous data reconstruction: Geophysics, **80**, no. 6, V189–V199.

Masoomzadeh, H., N. Woodburn, and A. Hardwick, 2013, Broadband processing of linear streamer data: 83rd Annual International Meeting, SEG, Expanded Abstracts, 4635–4639.

Mayhan, J. D., and A. B. Weglein, 2013, First application of Green's theorem-derived source and receiver deghosting on deep-water gulf of mexico synthetic SEAM and field data: Geophysics, **78**, no. 2, WA77–WA89.

Mikhailiuk, A., and A. Faul, 2018, Deep learning applied to seismic data interpolation: 80th Annual International Meeting, EAGE, Extended Abstracts, 1–5.

Monk, D. J., 1990, Wavefield separation of twin streamer data: First Break, **8**, 96–104.

Nath, S. K., S. Chakraborty, S. K. Singh, and N. Ganguly, 1999, Velocity inversion in cross-hole seismic tomography by counter-propagation neural network, genetic algorithm and evolutionary programming techniques: Geophysical Journal International, **138**, 108–124.

Nekut, A. G., and D. J. Verschuur, 1998, Minimum energy adaptive subtraction in surface-related multiple elimination: 68th Annual International Meeting, SEG, SEG, Expanded Abstracts, 1507–1510.

Orji, O. C., W. Sollner, and L. J. Gelius, 2013, Sea surface reflection coefficient estimation: 83rd Annual International Meeting, SEG, Expanded Abstracts, 51–55.

Parkes, G., and S. Hegna, 2011, A marine seismic acquisition system that provides a full 'ghost-free' solution: 81st Annual International Meeting, SEG, Expanded Abstracts, 37–41.

Parkes, G. E., and L. Hatton, 1986, The marine seismic source: Seismology and exploration geophysics: Reidel.

Petersen, K. B., and M. S. Pedersen, 2012, The matrix cookbook: Technical University of Denmark.

Pham, N., S. Fomel, and D. Dunlap, 2019, Automatic channel detection using deep learning: Interpretation, **7**, SE43–SE50.

Pierson, W. J., and L. Moskowitz, 1964, A proposed spectral form for fully developed wind seas based on the similarity theory of S. A. Kitaigorodskii: Journal of Geophysical Research, **69**, 5181–5190.

Poole, G., and J. Cooper, 2018, Multi-sensor receiver deghosting using data domain sparseness weights: 80th Annual International Meeting, EAGE, Extended Abstracts, We A10 08.

Posthumus, B. J., 1993, Deghosting using a twin streamer configuration: Geophysical Prospecting, **41**, 267–286.

Quan, T. M., D. G. C. Hildebrand, and W.-K. Jeong, 2016, Fusionnet: A deep fully resid-

ual convolutional neural network for image segmentation in connectomics: arXiv e-prints, arXiv:1612.05360.

Rickett, J., D.-J. V. Manen, P. Loganathan, and N. Seymour, 2014, Slanted-streamer data-adaptive de-ghosting with local plane waves: 76th Annual International Meeting, EAGE, Extended Abstracts, 4221–4225.

Robertsson, J. O. A., L. Amundsen, and O. Pedersen, 2014, Deghosting of arbitrarily depth-varying marine hydrophone streamer data by time-space domain modelling: 84th Annual International Meeting, SEG, Expanded Abstracts, 4248–4252.

Ronneberger, O., P. Fischer, and T. Brox, 2015, U-net: Convolutional networks for biomedical image segmentation: MICCAI 2015, Medical Image Computing and Computer-Assisted Intervention, 234–241.

Ross, C. P., and D. M. Cole, 2017, A comparison of popular neural network facies-classification schemes: The Leading Edge, **36**, 340–349.

Röth, G., and A. Tarantola, 1994, Neural networks and inversion of seismic data: Journal of Geophysical Research: Solid Earth, **99**, 6753–6768.

Sanchis, C., and T. Elboth, 2014, Multicomponent streamer noise characteristics and de-noising: 84th Annual International Meeting, SEG, Expanded Abstracts, 4183–4187.

Savels, T., K. de Vos, and J. W. de Maag, 2011, Surface multiple attenuation through sparse inversion; results for complex synthetics and real data: First Break, **29**, 55–64.

Sertlek, H. O., and M. Ainslie, 2015, Agora: Airgun source signature model: its application for the dutch seismic survey: Presented at the Conference Proceedings of UAC 2015.

Shi, Y., X. Wu, and S. Fomel, 2018, Automatic salt-body classification using deep-convolutional neural network: 88th Annual International Meeting, SEG, Expanded Abstracts, 1971–1975.

Siahkoohi, A., R. Kumar, and F. Herrmann, 2018, Seismic data reconstruction with generative adversarial networks: 80th Annual International Meeting, EAGE, Extended Abstracts, 1–5.

Siahkoohi, A., R. Kumar, and F. J. Herrmann, 2019a, Deep-learning based ocean bottom seismic wavefield recovery: 89th Annual International Meeting, SEG, Expanded abstracts, 2232–2237.

Siahkoohi, A., D. J. Verschuur, and F. J. Herrmann, 2019b, Surface-related multiple elimination with deep learning: 89th Annual International Meeting, SEG, Expanded Abstracts, 1052–3812.

Soubaras, R., 2010, Deghosting by joint deconvolution of a migration and a mirror migration: 80th Annual International Meeting, SEG, Expanded Abstracts, 3406–3410.

Soubaras, R., and R. Dowle, 2010, Variable-depth streamer — a broadband marine solution: First Break, **28**, no. 12, 89–96.

Staal, X. R., 2015, Combined imaging and velocity estimation by joint migration inversion: Doctoral dissertation, Delft University of Technology.

Sun, H., and L. Demanet, 2018, Low-frequency extrapolation with deep learning: 88th Annual International Meeting, SEG, Expanded Abstracts, 2011–2015.

Sun, Y., and D. Verschuur, 2017, 3D receiver deghosting for seismic streamer data using L1 inversion in an extended Radon space: 87th Annual International Meeting, SEG, Expanded Abstracts, 4940–4944.

Sun, Y., D. J. Verschuur, and R. G. van Borselen, 2018, Acoustic propagation operators for

A

pressure waves on an arbitrarily curved surface in a homogeneous medium: Journal of Applied Geophysics, **150**, 314–324.

Tang, Z., and X. Campman, 2017, Joint up/down decomposition and reconstruction using three-component streamers with or without ghost model: the sampling theory: Geophysical Prospecting, **65**, 956–980.

Telling, R., and S. Grion, 2019, A perturbed ghost model for estimating air-gun array signatures: The Leading Edge, **38**, 658–740.

Telling, R., S. Grion, S. Denny, and R. G. Williams, 2018, Marine source signature estimation with dual near-field hydrophones: 88th Annual International Meeting, SEG, Expanded Abstracts, 4070–4074.

ten Kroode, F., S. Bergler, C. Corsten, J. W. de Maag, F. Strijbos, and H. Tijhof, 2013, Broadband seismic data - the importance of low frequencies: Geophysics, **78**, no. 2, WA3–WA14.

Tenghamn, R., S. Vaage, and C. Borresen, 2007a, A dual-sensor towed marine streamer: Its viable implementation and initial results: 77th Annual International Meeting, SEG, Expanded Abstracts, 989–993.

——, 2007b, A dual-sensor towed marine streamer: Its viable implementation and initial results: 77th Annual International Meeting, SEG, Expanded Abstracts, 989–993.

Trad, D. O., 2009, Five-dimensional interpolation: Recovering from acquisition constraints: Geophysics, **74**, V123–V132.

van den Berg, P. M., and J. T. Fokkema, 1980, The rayleigh hypothesis in the theory of diffraction by a perturbation in a plane surface: Radio Science, **15**, 723–732.

van Groenestijn, G. J. A., and D. J. Verschuur, 2009a, Estimating primaries by sparse inversion and application to near-offset data reconstruction: Geophysics, **74**, A23–A28.

——, 2009b, Estimation of primaries and near offsets by sparse inversion: Marine data applications: Geophysics, **74**, R119–R128.

Verschuur, D. J., 2014, Generalization of the EPSI primary estimation algorithm for deep-towed and slanted cables: 76th Annual International Meeting, EAGE, Extended Abstracts, 1911–1915.

Verschuur, D. J., and A. J. Berkhout, 1997, Estimation of multiple scattering by iterative inversion, part II: practical aspects and examples: Geophysics, **62**, 1596–1611.

Verschuur, D. J., A. J. Berkhout, and C. P. A. Wapenaar, 1992, Adaptive surface-related multiple elimination: Geophysics, **57**, 1166–1177.

Verschuur, D. J., J. W. Vrolijk, and C. Tsingas, 2012, 4D reconstruction of wide azimuth (WAZ) data using sparse inversion of hybrid radon transforms: 82nd Annual International Meeting, SEG, Expanded Abstracts, https://dx.doi.org/10.1190/segam2012-098.1.

Vrolijk, J. W., and G. Blacquière, 2017, Deghosting and its effect on noise: 79th Annual International Meeting, EAGE, Extended Abstracts, 1–5.

——, 2018, Adaptive deghosting for a rough and dynamic sea surface: 88th Annual International Meeting, SEG, Expanded Abstracts, 4583–4587.

——, 2020a, Adaptive estimation of the upgoing wavefield from a variable-depth recording in the case of a dynamic sea surface: Geophysics, **85**, no. 1, 1JF–Z3.

——, 2020b, Adaptive estimation of the upgoing wavefield from a variable-depth recording in the case of a dynamic sea surface: Geophysics, **85**, no. 1, C1–Y1.

Vrolijk, J. W., D. J. Verschuur, and G. A. L. Angarita, 2017, Integrated receiver deghosting and closed-loop surface-multiple elimination: Geophysics, **82**, no. 4, T133–T141.

Walker, C., D. Monk, and D. Hays, 2014, Blended source - the future of ocean bottom seismic acquisition: Presented at the 76th Annual International Meeting, Extended Abstracts, EAGE.

Wang, B., N. Zhang, W. Lu, J. Geng, and X. Huang, 2020, Intelligent missing shots' reconstruction using the spatial reciprocity of green's function based on deep learning: IEEE Transactions on Geoscience and Remote Sensing, **58**, 1587–1597.

Wang, P., and C. Peng, 2012, Premigration deghosting for marine towed streamer data using a bootstrap approach: 82nd Annual International Meeting, SEG, Expanded Abstracts, https://dx.doi.org/10.1190/segam2012–1146.1.

Wang, P., S. Ray, and K. Nimsaila, 2014, 3D joint deghosting and crossline interpolation for marine single-component streamer data: 84th Annual International Meeting, SEG, Expanded Abstracts, 3594–3598.

Wapenaar, C. P. A., and A. J. Berkhout, 1989, Elastic wave field extrapolation: redatuming of single- and multi-component seismic data: Elsevier.

Weglein, A. B., F. V. Araujo, P. M. Carbvalho, R. H. Stolt, K. H. Matson, R. T. Coates, D. Corrigan, D. J. Foster, S. A. Shaw, and H. Zhang, 2003, Topical review: Inverse scattering series and seismic exploration: Inverse Problems, **19**, R27–R83.

Weglein, A. B., F. A. Gasparotto, P. M. Carvalho, and R. H. Stolt, 1997, An inverse scattering series method for attenuating multiples in seismic reflection data: Geophysics, **62**, 1975–1989.

Yilmaz, Ö., 2001, Seismic data analysis: Society of Exploration Geophysicists.

Zhang, D., and E. Verschuur, 2019, Integration of closed-loop surface-related multiple estimation and full wavefield migration for shallow water: 81th Annual International Meeting, EAGE, Extended Abstracts, 1–5.

Ziolkowski, A. M., G. E. Parkes, L. Hatton, and T. Haugland, 1982, The signature of an air gun array: Computation from near-field measurements including interaction: Geophysics, **47**, 1413–1421.

Zwartjes, P. M., and M. D. Sacchi, 2007, Fourier reconstruction of nonuniformly sampled, aliased seismic data: Geophysics, **72**, no. 1, V21–V32.

ACKNOWLEDGEMENTS

To my parents, Hans and Jolande, sister Janneke and the rest of my family, thank you for your continued support and love.

Willemijn, you have positively turned my life upside down. I am sorry for the times when it was hard for you to get through to me because I had my focus on doing research. Thank you, for your unconditional support and love as a girlfriend, wife and mother of our beautiful girl, Noor.

Jan-Willem Vrolijk
October 2020

CURRICULUM VITÆ

Jan-Willem VROLIJK

16-10-1986   Born in Rijnsburg, Netherlands.

EDUCATION

2016–2020   PhD. candidate in Geophysics
Delft University of Technology, Delft, The Netherlands

2009–2011   MSc. in Applied Physics
Delft University of Technology, Delft, The Netherland

2005-2009   BSc. in Applied Physics
Delft University of Technology, Delft, The Netherland

WORK EXPERIENCE

2016–2020   PhD. candidate in Geophysics
Delft University of Technology, Delft, The Netherlands

2012–2016   Research Geophysicist
Delphi Studio for Imaging, Delft, The Netherlands

LIST OF PUBLICATIONS

JOURNAL PAPERS

5. **J.W. Vrolijk**, G. Blacquière, *Source deghosting of coarsely-sampled data using a machine-learning approach*, Geophysics (accepted).

4. **J.W. Vrolijk**, G. Blacquière, *Adaptive estimation of the upgoing wavefield from a variable-depth recording in the case of a dynamic sea surface*, Geophysics **85** , no. 1, JF-Z3 (2020).

3. **J.W. Vrolijk**, D.J. Verschuur, G.A. Lopez, *Integrated receiver deghosting and closed-loop surface-multiple elimination*, Geophysics **82**,no. 4,1JA-Z33 (2017).

2. Y. Sun, D.J. Verschuur, **J.W. Vrolijk**, *Solving the complex near-surface problem using 3D data-driven near-surface layer replacement*, Geophysical Prospecting **62**, no. 3, 491-506, (2014).

1. **J.W. Vrolijk**, P. Haffinger, D.J. Verschuur, *Multi-datum based estimation of near-surface full-waveform redatuming operators*, Journal of Applied Geophysics **82**, 30-45, (2012).

CONFERENCE PAPERS

10. **J.W. Vrolijk**, G. Blacquière, *Source deghosting of coarsely-sampled data using a machine-learning approach*, EAGE, Extended Abstracts (2020).

9. **J.W. Vrolijk**, G. Blacquière, *Adaptive source deghosting in the common-shot domain*, SEG, Expanded abstacts (2019).

8. **J.W. Vrolijk**, G. Blacquière, *Adaptive deghosting for a rough and dynamic sea surface*, SEG, Expanded abstacts (2018).

7. **J.W. Vrolijk**, G. Blacquière, *Adaptive Deghosting Including the Rough and Time Variant Sea Surface*, EAGE, Extended Abstracts(2018).

6. **J.W. Vrolijk**, G. Blacquière, *Shot-based deghosting for variable sea surface and receiver depth*, SEG, Expanded abstacts(2017).

5. **J.W. Vrolijk**, G. Blacquière, *Deghosting and its Effect on Noise*, EAGE, Extended Abstracts (2017).

4. **J.W. Vrolijk**, D.J. Verschuur, *Integrated receiver deghosting and closed-loop surface multiple elimination*, SEG, Expanded abstacts (2016).

3. **J.W. Vrolijk**, D.J. Verschuur, *Integrated deghosting and multiple removal: field data experience*, SEG, Expanded abstacts (2015).

2. D.J. Verschuur, **J.W. Vrolijk**, C. Tsingas *4D reconstruction of wide azimuth (WAZ) data using sparse inversion of hybrid Radon transformst*, SEG, Expanded abstacts (2012).

1. **J.W. Vrolijk**, P. Haffinger, D.J. Verschuur *Multi-datum based estimation of near-surface full-waveform redatuming operators*, SEG, Expanded abstacts (2011)